PhD Thesis

Multi-manifold Diffeomorphic Metric Mapping for Cortical Registration with its Applications in Brain Structural and Functional Studies

Jidan Zhong
NUS Graduate School for Integrative Sciences and Engineering
National University of Singapore

A DISSERTATION SUBMITTED IN PARTIAL FULFILLMENT OF THE REQUIREMENTS OF

PhilosophiæDoctor (PhD)

2011

1. Reviewer:

2. Reviewer:

3. Reviewer:

Acknowledgements

I would like to express my deep and sincere gratitude to my advisor Dr Anqi Qiu, Assistant Professor in Department of Bioengineering, National University of Singapore. It has been an honor to be her first Ph.D. student. Her unending encouragement and full research support have provided a necessary basis for the present thesis. I appreciate all her contributions of time and ideas to my Ph.D. experience.

I am deeply grateful to my advisor Dr Annett Schirmer, Associate Professor in Department of Psychology, National University of Singapore. I thank her for the technical discussions and constructive comments throughout this work.

The CFA lab has been a source of friendship as well as good advice and collaboration. I am especially grateful for the original lab mates who have been giving me advice and sticking by me through troubles on my project: Ta Anh Tuan, Du Jia, Hock Wei Soon and Jordan Bai Bingren. I would like to acknowledge other past and present lab mates that I have had the pleasure to work with or alongside of are Sergey Kushnarev, Muhammad Farid Bin Abdul Rahman, Wang Yanbo, Yang Xianfeng, and Gan Swu Chyi.

I gratefully acknowledge the funding sources that made my Ph.D. work possible. I was funded by NUS Graduate School for Integrative Sciences and Engineering scholarship for four years study. My work was also supported by National University of Singapore start-up grant R-397-000-058-133, A.STAR SERC 082-101-0025, and A.STAR SICS-09/1/1/001.

I wish to thank my friends who made my time in Singapore enjoyable and helped me get through the difficult times: Pengfei He, Tao Peng, Kelei Chen, Jiajin Li, Dan Kai, Liuya Min, Danyang Kong, Yuan Ping, Dong Shao and Kan Lin. I appreciate all the emotional support, entertainment, and caring they provided.

Lastly, I would like to thank my parents for their love, understanding and endless encouragement. Thank you.

Contents

Summary

The human cortex is a convoluted sheet that forms sulco-gyral patterns to allow a large surface area inside the skull. Thus, in terms of distance measured along the cortex, functionally distinct regions are geometrically distant but close to each other in volume space. Because of this complexity, one of the main challenges in brain structural and functional MRI studies is to optimize the alignment of the cortical structures across individuals. In this thesis, we first develop a new diffeomorphic mapping algorithm, multi-manifold large deformation diffeomorphic metric mapping (MM-LDDMM), for morphing the cortical hemispheric surfaces using the geometry of sulcal curves (1-dimensional manifold) and cortical surface (2-dimensional manifold) in their own coordinates. This registration algorithm could better align both local regions and global shape patterns compared to previous registrations in the LDDMM framework and the spherical registrations implemented in CARET and FreeSurfer softwares.

Once the registration method is developed, we subsequently apply it in a structural study for generating a cortical surface template. As average template generation is based on registration, only good registration would give representative template over a population. We generate an average template for a sample of subjects including young healthy adults to healthy elders as well as dementia patients with the MM-LDDMM registration. It maintains the detailed sulco-gyral pattern but not limited to major deep sulci. This template is representative for the population in terms of its metric distance to each subject in the population and would be useful in the shape study in a variety of neurodegenerative diseases and healthy aging.

Other than in structural studies, good brain registration is also required in functional studies to locate which brain region is related to a particular function. While the functional connectivity of the brain in the early childhood is not clear but very important for our understanding of the normal brain development, we conduct resting state functional MRI analyses based on MM-LDDMM registration. We analyze the resting state functional connectivity of 6-year-old children's brain with a large sample and identify the primary, higher order networks and default mode network (DMN). This study suggests that intrinsic functional networks of the brain are formed with well-developed visual and somatomotor networks but developing auditory, attention, executive networks, and DMN at six years of age. Moreover, we investigate the resting state functional connectivities development between 6 and 10 years old children and examine their relations with cognitive performance to better understand the functional development during early childhood. Using the seed correlation method and graph theoretical analyses, we report that, during early development, both regional activation and functional interactions between regions, especially for those in frontal networks, are changing prominently, which can be partly due to structural changes and has important relationship with cognitive performance for executive functions. This study provides new information about normal neurodevelopmental trajectories during early childhood, which could enable us to better understand any abnormal developments for those neurodevelopmental disorders.

List of Tables

List of Figures

List of Symbols

$\cdot$	Group action, page 23
$*$	Matrix transpose, page 24
$\mathbf{D}$	Jacobian matrix, page 29
I_{temp}	Template object, page 22
I_{targ}	Target object, page 22
γ	Curve, page 31
S	Surface, page 31
$k_V(\cdot,\cdot)$	Kernel of Hilbert space V, page 23
$k_W(\cdot,\cdot)$	Kernel of Hilbert space W, page 24
m_t	Momentum at time t, page 29
v_t	Velocity vector field at time t, page 22
$x_i(t)$	Coordinate of point i at time t, page 23
$\mathbf{x}_t$	Coordinate array of a point set at time t, page 31
$\mu_{\mathbf{x}}$	Vector-valued measure of point set, $\mathbf{x}$, page 24
ϕ_t	Flow of diffeomorphism, page 22
$\alpha_i(t)$	Momentum vector of point i at time t, page 30
$\alpha_{\mathbf{t}}$	Momentum vector array of a point set at time t, page 31
δ	Dirac measure, page 24
∇_1	Gradient with respect to the first variable, page 30

1

Introduction

1.1 Motivation

The human brain is the center of the nervous system, so complex that even the slightest damage can result in dire consequences. Damage to different brain regions can result in varying types of brain disorders with different grades of severity. For instance, inflammation in the brain can result in impairments such as weakness and paralysis, while strokes, stemming from a reduction of brain blood supply, can make everyday tasks like walking and talking difficult. Brain tumors can press on normal brain tissues, nerves and blood vessels, thus affecting brain function. Other neurodegenerative diseases resulting from the loss of structures or functions of neurons, such as Huntington's and Alzheimer's disease, can affect emotion, memory, language functions and so on. As the brain is very important yet vulnerable, brain disorders warrant utmost care and treatment. Magnetic resonance imaging (MRI), often divided into structural MRI and functional MRI (fMRI), is an important non-invasive technique for diagnosing and treating medical conditions. Structural MRI can provide good contrast of gray/white matter and help detect the abnormalities of shape and structures, while fMRI looks at the blood flow in a normal, diseased or injured brain to detect areas of activity which are involved in a task, a process or an emotion. MRI can therefore help physicians evaluate both the structure of the brain and how it works.

To identify the brain anatomical changes and regions responsible for particular functions with MRI images, group analysis based on a population of subjects is required. Moreover, to precisely identify the location of the regions within a population, correct spatial correspondences across images need to be established to guarantee the reliability of the analysis. This can be achieved through the process of transforming different images into one coordinate system, known as image registration, which is necessary for comparing or integrating data obtained from different measurements. However, the conventional image registration based on volume fails to offer good anatomical accuracy due to the complex convolution of the cortex. A small inaccuracy in volume registration may cause large inaccuracies in structural localization, especially for the sulcal and gyral patterns, for example, for points on two sides of a sulcus (1).

As the sulco-gyral folding pattern varies across individuals in the human cerebral cortex, and the sulci and gyri are related to functional areas (2) and architectonic boundaries (3), registration based on the cortical surface models which preserve the sulco-gyral pattern information is more accurate than the volume based registration (2). The widely used spherical surface registration approaches require a spherical representation of the brain before registration (4, 5), however, introducing inconsistent distortion of the brain structure across subjects, which potentially affects the quality of surface registration. Registration based on the cortical surfaces in their own coordinates is not without flaws though, as the method fails to align both the cortical surface and sulci/gyri together (6, 7, 8). While it has been shown that registration with higher accuracy could increase the statistical power for the functional studies (9), better registration methods are needed to give us more reliable structural and functional statistical results in our applications. This thesis is aimed at the development of new cortical surface registration algorithms to control both local and global alignment as an improved alternative to other existing methods. Subsequently, we present its application in structural and functional MRI studies.

1.2 Thesis Contributions

Figure 1.1 shows the general work flow for the thesis. We develop a new cortical surface registration method, named multi-manifold large deformation diffeomorphic metric mapping (MM-LDDMM), that deforms the cortical hemispheric surfaces using the geometry of both sulcal curves (1-dimensional manifold) and cortical surface (2-dimensional manifold) in their own coordinates. It is the extension of the previous works on region of interest (ROI)-based LDDMM surface registration and LDDMM sulcal curve registration. It takes advantages of the landmark (or ROI)-based registration approaches for improving the quality of regional alignment when prior labeling information (sulcal curves or ROI) is given. In addition, it also takes the dense representation of the cortex, the cortical hemispheric surface, to control the quality of global as well as regional alignment. The performance of this method is evaluated by

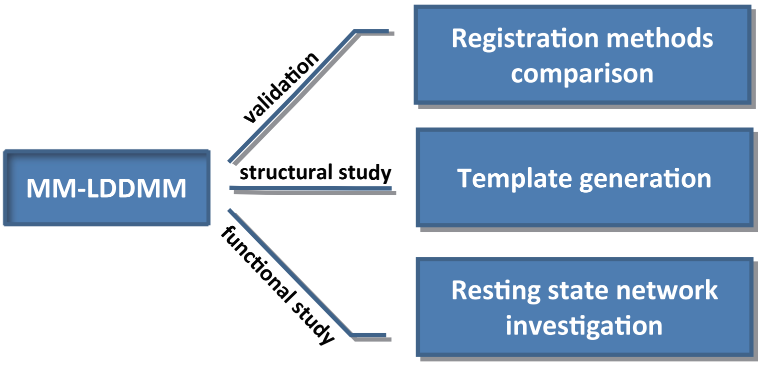

Figure 1.1: General work flow for the whole thesis.

comparison to the other surface registration methods, and its advantages are presented. Having the registration method developed and evaluated, our registration method is then applied to a structural MRI study, where an average surface template is generated. As the structural and functional group studies are template-dependent, a template which can represent morphology and individual variability can cause less bias for those studies. While average template generation is based on registration, only good registration would give representative template over a population. We generate an average template for a sample of subjects including young healthy adults to the healthy elders as well as the dementia patients with the MM-LDDMM registration. It maintains the detailed sulco-gyral pattern but this is not limited to major deep sulci. This template is representative for the population in terms of its metric distance to each subject in the population and would be useful in the shape study in a variety of neurodegenerative diseases and healthy aging.

Other than in structural studies, good brain registration is also required in functional studies to identify regions responsible for particular functions. While the functional connectivity of the brain in the early childhood is not clear but very important for our understanding of the normal brain development and functional changes in patients with neurodegenerative diseases, we conduct resting state functional MRI analyses based on MM-LDDMM registration. We analyze the resting state functional connectivity of 6-year-old children's brain with a large sample and identify the primary, higher order networks and default mode network (DMN),which fills the knowledge gap for our understanding of the functional connectivity from children to adults. Moreover, as many neurodegenerative disorders have their origins in infancy and early childhood, to help the understanding of the abnormal functional development during early childhood, we investigate the resting state functional connectivities development between 6 and 10 years old normal children and examine their relations with cognitive performance. Using the seed correlation method, we show a protracted developmental trajectory for functional circuits, with decreased connectivity related to improved attention, response inhibition and memory performances. Also, using graph analyses, we report that significant changes of the importance (in terms of betweenness centrality) of specific regions of interest (ROIs) and inter-ROI connections in the frontal networks are associated with improved response inhibition and memory functions during early childhood. These findings show the importance of frontal regions in the functional development and provide new information about normal neurodevelopmental trajectories during early childhood.

To summarize, this thesis contributes towards the registration of cortical surfaces and its application in structural and functional analyses by:

1. Developing a new surface-based registration method, MM-LDDMM algorithm with both curves and surface information to control the local and global alignment and thus improve registration accuracy.
2. Investigating the different performance of MM-LDDMM method with other existing surface-based registration methods.
3. Generating a cortical surface template using MM-LDDMM based on the initial momentum to reduce the influence from single subject template during analysis.
4. Applying the new registration method to resting state fMRI to analyze the functional connectivity and the functional development during early childhood as well as the relationship between the normal functional development and the cognitive performance.

1.3 Thesis Overview

The subsequent chapters are organized as follows. Chapter 2 describes brain anatomy and introduces some background information related to brain imaging and imaging analysis that shall be used in the rest of the thesis. We also present a review of related work in brain registration and specifically provide background on the theoretical frameworks used in our work, e.g., LDDMM framework. In Chapter 3 we describe our approach to multi-manifold LDDMM registration of cortical surfaces. It is followed by the evaluation of the MM-LDDMM registration in comparison with the previous registration methods in the LDDMM framework and the popular spherical registrations in Chapter 4, where the registration improvements of the MM-LDDMM method are also presented. Then we apply the MM-LDDMM registration into the average template generation in Chapter 5 and in the resting state functional MRI analysis in Chapter 6 and 7. Finally, in Chapter 8, we list our conclusions and recommendations for future directions.

2

Background

2.1 Anatomy of Cerebrum

The human brain is the center of the human nervous system and the cerebrum, as the largest and most prominent part of the human brain, is the control center of it. It is 85% of the weight of a human brain. Structurally, it is divided into two hemispheres, the left and the right, each of which is divided into four lobes: Frontal, Parietal, Occipital and Temporal lobes (see Figure 2.1 (A)). The cerebrum consists of two layers, an outer layer called the cerebral cortex, consisting of gray matter (unmyelinated neurons), and one inner layer, called the cerebral medulla, consisting of white matter (myelinated axons) (see Figure 2.1 (B)). The Cerebrum is responsible for many functions, such as language, conscious thought, memory, personal development, vision and other sensations.

The cerebral cortex, which makes up the superficial aspect of the cerebrum, is the most complex and important structure of the human brain. The surface of the human cerebral cortex is folded in a sulco-gyral pattern (see Figure 2.1 (B)), allowing a large surface area to fit in the skull, with more than two-thirds of the cortical surface buried in the sulci. The cerebral cortex has the thickness of about 2- 4 *mm* and is formed by billions of neurons, each linked with up to 10,000 synaptic connections. The neurons communicate with one another through axons, which carry action potentials to distant parts of the brain and body, targeting specific recipient cells and thus being responsible for the master control of all mental functions. Different parts of the cerebral cortex are involved in different cognitive and behavioral functions. For example, frontal lobe is involved in memory (10) while occipital lobe plays an integral role of visual sensory processing (11). The primary auditory cortex is located in the temporal lobe while

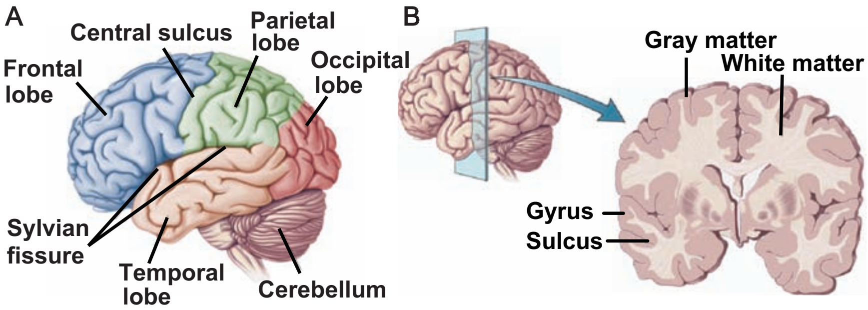

Figure 2.1: Cerebrum Anatomy. (A) different lobes of the cerebrum, (B) different layers of the cerebrum and the sulco-gyral pattern. The images were taken from `www.bioon.com/book/biology/whole/image/1/1-8.tif.jpg` and `www.bioon.com/book/biology/whole/image/1/1-6.tif.jpg`

somatosensory cortex is located in the parietal lobe, just behind the central sulcus.

When brain is healthy, it works well and quickly. However, when brain damage occurs, problems quickly surface and mount. For example, inflammation in the brain can lead to problems such as weakness and paralysis (12). Strokes, resulting in a loss of brain cells, can affect the ability to think clearly (13). Multiple sclerosis can affect the transmission of electrical signals to nerve cells (14), while Parkinson's Disease, a movement disorder, leads to tremors and difficulty with walking, movement, and coordination (15). As an important non-invasive technique for diagnosing and treating medical conditions of the brain, Magnetic resonance imaging (MRI) can help physicians evaluate both the structure and function of the brain.

2.2 Basics of Magnetic Resonance Imaging

2.2.1 Basic Physics

Magnetic Resonance Imaging (MRI) is a non-invasive method to visualize internal structures. It provides good contrast between the different soft tissues of the body, allowing a differentiation between gray matter, white matter and brainstem in the brain. MRI is based on the principles of nuclear magnetic resonance (NMR), a physical phenomenon that atomic nuclei interact with the electromagnetic wave in the magnetic field. The primary constituents of the human body are fat and water, which have many hydrogen atoms to make up approximately 63% the human body.

An MRI machine applies a powerful magnetic field to magnetize and align the hydrogen nuclei in the body. A radio frequency (RF) is subsequently introduced to alter this alignment systematically. This causes the nuclei to produce NMR signals detectable by the MRI scanner, which are recorded to construct an image of the scanned area (16). As strong magnetic field gradients cause nuclei at different locations to rotate at different speeds, 3-D images can be obtained by providing gradients in each direction.

2.2.2 Basic Principles of MRI

2.2.2.1 Spin and Magnetic Moment

Spin is a fundamental property of nature which comes in multiples of 1/2 and can be positive or negative. The spinning of the nuclear particles produces angular momentum **J** which is a vector with both magnitude and direction. The largest measurable component of it, expressed as I, represents the overall spin value as spin quantum number. Protons, electrons and neutrons possess spin. Nuclei are composed of positively charged protons and uncharged neutrons. Nuclei with odd number of protons or neutrons have nuclear spins of multiples of 1/2, while those with even number of protons and neutrons have no spin. Two or more particles with spins having opposite signs can pair up to get the overall spin as 0. Hydrogen nuclei, which makes up 63% the human body, possess spins of 1/2. The spin of a proton as a magnetic moment vector behaves like a tiny magnet with a north (N) and south pole (S) (Figure 2.2).

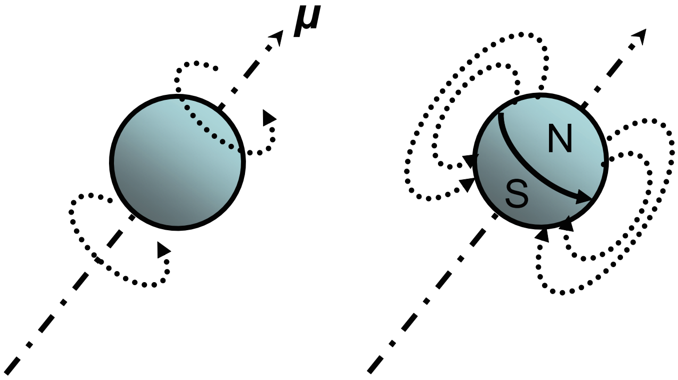

Figure 2.2: Spin of a nucleus as a magnetic moment vector μ behaves like a tiny magnet with a north (N) and south (S) pole.

The angular momentum **J** generated by spinning is quantized. The corresponding quantum number is known as the magnetic quantum number, m, and can take values of $I, I-1, \ldots, -I$

and thus a total of $2I + 1$ angular momentum states. A non-zero spin is associated with a non-zero magnetic moment ($\vec{\mu}$) via the relation $\vec{\mu} = \gamma \mathbf{J}$, where γ is the gyromagnetic ratio. The z-component of the angular momentum vector ($\mathbf{J}$) is $J_z = m\hbar$, where $\hbar$ is the reduced Planck constant ($= 1.0545726 \times 10^{-34} m^2 kg/s$). Thus the z-component of the magnetic moment is simply: $\mu_z = \gamma J_z = \gamma m\hbar$.

2.2.2.2 Effect of Magnetic Field

In the absence of an externally applied magnetic field, the magnetic moments have random orientations. When the proton is placed in an external magnetic field B_0, the spin vector lines up (at a slight angle) with the external field, either parallel or anti-parallel with respect to B_0. In addition, the nuclei precess about the magnetic field direction like gyroscopes at some frequency called Larmor frequency: $\omega_0 = \gamma B_0$ (Figure 2.3).

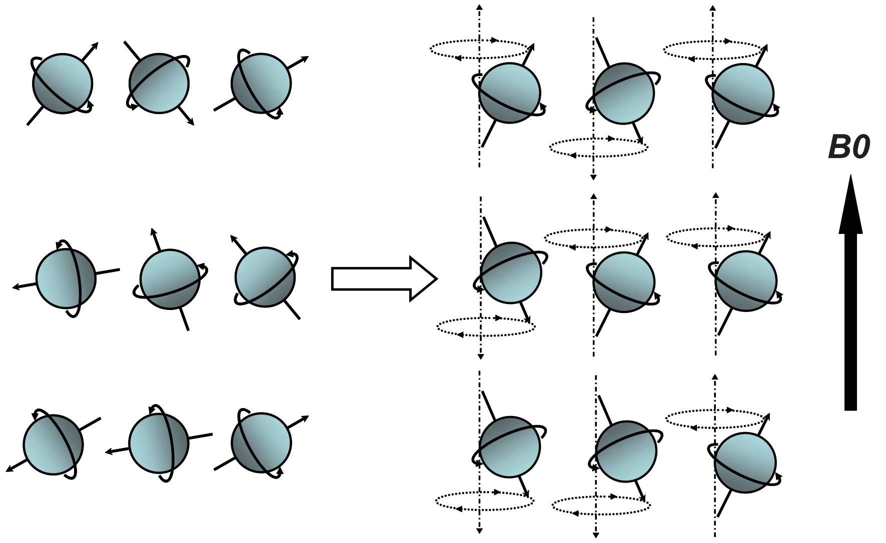

Figure 2.3: Left panel– magnetic moments with random orientations in the absence of external magnetic field; Right panel– magnetic moments parallel or anti-parallel aligned with the external field

Protons aligned in the parallel orientation are in a low energy level state while protons in the anti-parallel orientation are in a high-energy state. The energy E of a magnetic moment $\vec{\mu}$ when in a magnetic field B_0 is given by: $E = -\vec{\mu} \cdot \mathbf{B}_0 = -\mu_z B_0 = -\gamma m\hbar B_0$. The lower energy state of protons corresponding to m = +1/2 in a static magnetic field B_0 is $E(\frac{1}{2}) = -\frac{1}{2}\gamma\hbar B_0$. The higher energy state of protons corresponding to m = -1/2 is given by $E(-\frac{1}{2}) = \frac{1}{2}\gamma\hbar B_0$. Consequently, the energy differences between two quantum states can be calculated as $\triangle E = \gamma\hbar B_0$ (Figure 2.4).

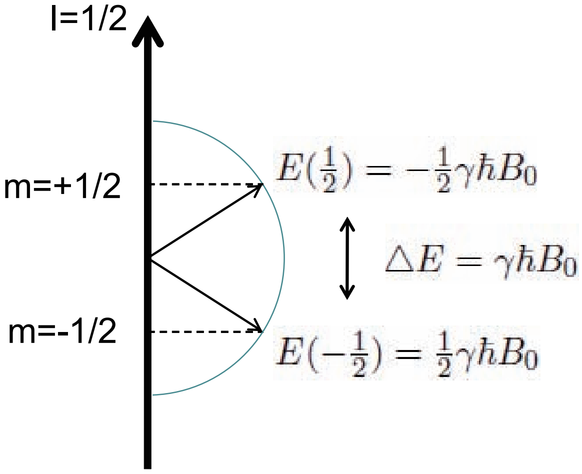

Figure 2.4: For protons with spin quantum number of 1/2, two energy levels and the energy difference are shown.

As protons aligned in the parallel orientation are in a low energy level with a more stable state, the number of spins under this state is more than that under the high energy state. This number of difference is called spin excess and the magnetic moments of the excess spins add to form the net magnetization. When the spin system is at equilibrium, net magnetization lies along the z axis, the same as the external magnetic field.

2.2.2.3 Magnetic Resonance by Nuclei

The proton would undergo a transition from the lower energy state to the higher energy state by the absorption of a photon. The energy of this photon must exactly match the energy difference between the two states. While the energy of an absorbed photon is $E = h\nu_0$, the energy difference between the nuclear spin levels is $\triangle E = \gamma\hbar B_0$. Hence, a magnetic resonance absorption will only occur when $\nu_0 = \gamma B_0/(2\pi)$, which is the same as Larmor frequency.

2.2.2.4 Relaxation

When exposing the nuclear spin system to energy of a radio frequency (RF) that equals to the energy difference between the spin states, the equilibrium of the spin system is disturbed. Individual spins begin to precess in phase, as will the net magnetization. Protons would absorb photons and transit to high energy level. Thus, the net magnetization would move toward the transverse plane. With the termination of the RF field, the nuclei in the excited state would return to the steady state or the equilibrium condition, which process is called relaxation. The energy transmitted in this process is observed as the MRI signal. Two relaxation processes, spin-lattice and spin-spin relaxations, allow nuclear spins to return to equilibrium.

Spin-Lattice (Longitudinal) Relaxation: This process is called ”spin-lattice”, ”longitudinal magnetic” or T_1 relaxation, where T_1 refers to the mean time for an individual nucleus to dissipate its excess energy as heat to the surrounding environment (or lattice) and return to its thermal equilibrium state of the spins.

At equilibrium, the net magnetization vector lies along the direction of the main magnetic field B_0 and is called the equilibrium magnetization $\mathbf{M}_0$. Here, the longitudinal magnetization M_Z equals M_0. To describe how M_Z returns from 0 to its equilibrium during relaxation after the RF pulse has stopped, the equation as a function of the time t is written as: $M_Z = M_0(1-e^{-t/T1})$ where T_1 is the time taken for approximately 63% of the longitudinal magnetization to be restored following the RF pulse (Figure 2.5(A)).

Spin-Spin (Transverse) Relaxation: The magnetic moments of the nuclei can interact with each other causing a decrease in transverse magnetization M_{XY}, which is called transverse relaxation. The time constant which describes the return to equilibrium of the transverse magnetization, is called the spin-spin relaxation time, T_2, $M_{XY} = M_{XYmax}e^{-t/T2}$, where T_2 is the time it takes for the transverse magnetization to decay to 37% of its original magnitude. T_2 is always less than or equal to T1. The net magnetization in the XY plane goes to zero and then the longitudinal magnetization grows in until we have M_0 along Z (Figure 2.5(B))

T_2^*: In practice, the decay of transverse magnetization depends on both the static magnetic field inhomogeneity and molecular interactions. The corresponding transverse relaxation time is called as T_2^* and is as follows: $\frac{1}{T_2^*} = \frac{1}{T_2} + \frac{1}{T_2 inhomo}$ (Figure 2.5(C)).

MR signal contrast: The concentration of mobile hydrogen protons in a tissue is referred to as its spin density (proton density). The strength of the MRI signal depends primarily on three parameters: proton density in a tissue, T_1 and T_2. The contrast between brain tissues is dependent upon how these 3 parameters differ between tissues. Different tissues have different viscosity or rigidity, thus with different T_1 and T_2. It is possible to manipulate the MR image contrast by changing the pulse sequence parameters. A pulse sequence is a combination of one or more RF pulses and gradients with intervening periods of recovery. The two most important parameters are the repetition time (T_R) and the echo time (T_E). The T_R is the time

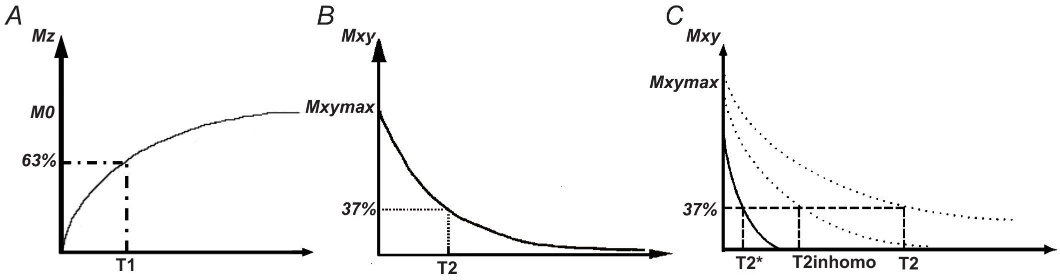

Figure 2.5: Diagram depicting the relaxation processes of T_1 (panel A), T_2 (panel B) and T_2^* (panel C). T_2^* is shorter than T_2.

between consecutive 90 degree RF pulse (which means the RF pulse is 90 degrees to the B_0 field). The T_E is the time between the initial 90 degree RF pulse and the echo. The most common pulse sequences are the T_1-weighted and T_2-weighted spin-echo sequences. In the case of T_1-weighted MRI, images are created typically with short T_E and short T_R times. They can differentiate fat from water - with fat brighter and water darker (`www.mr-tip.com`) by using a gradient echo (GRE) sequence. In the brain T1-weighted scans provide good gray matter/white matter contrast. In addition, the image contrast can be increased with the use of an inversion pulse as in an MP-RAGE sequence. Due to short T_R, this scan can be run very quickly, allowing the collection of high resolution 3D structural image (Figure 2.6, Left). These structural images can provide detailed information of the brain's shape and size, and provide the base for cortical surface reconstruction and segmentation. The T_2-weighted sequence uses a long T_R and long T_E. The T_2-weighted sequence can be employed as a dual echo sequence. Like the T_1-weighted scan, fat is differentiated from water, but with fat dark and water bright (Figure 2.6, Middle). The first or shorter echo ($T_E < 30 msec$) is proton density (PD) weighted or a mixture of T_1 and T_2. This image can provide good contrast of tissue and CSF, thus very helpful for evaluating periventricular pathology (Figure 2.6, Right). T_2^*-weighted scans use a gradient echo (GRE) sequence, with long T_E and long T_R. It is prone to susceptibility losses at air/tissue boundaries, but can increase contrast for certain types of tissue, such as venous blood.It is used for functional MRI detection allowing people to visualize and map the parts of the brain used to perform tasks.

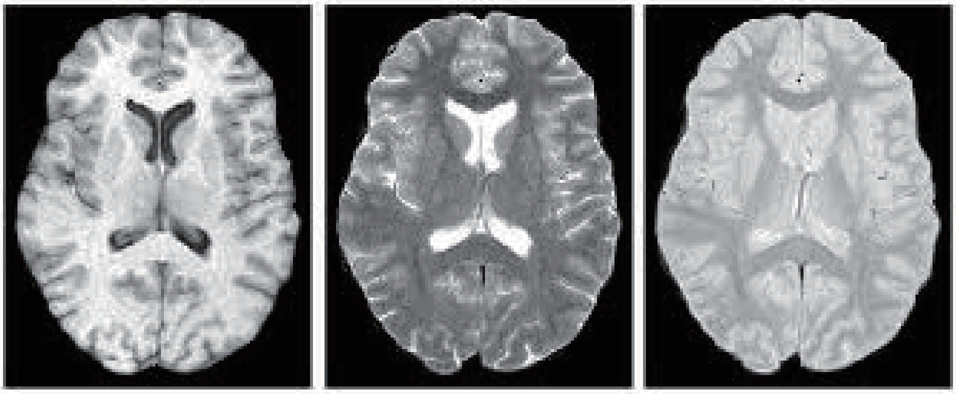

Figure 2.6: Brain scan using T_1 (left), T_2 (middle) and proton density (right) measurements. The figures are from `www.fmrib.ox.ac.uk/analysis/research/fast/slideshow/t1_t2_pd.gif`.

2.2.3 Functional Magnetic Resonance Imaging

Functional magnetic resonance imaging (fMRI) is one special type of MRI scan to measure signal changes in the brain related to neural activity. The human brain, like other organs in the body, needs oxygen to metabolize glucose to provide energy. While oxygen is delivered by hemoglobin in the blood, increased neural activity causes an increased demand for oxygen. Hemoglobin is diamagnetic when oxygenated (oxyhemoglobin) but paramagnetic when deoxygenated (deoxyhemoglobin) (17). Increase of neural activity will increase the amount of oxyhemoglobin and change the local ratio of oxyhemoglobin to deoxyhemoglobin, which lead to a detection method called blood oxygen level dependent (BOLD) contrast. Changes in blood oxygenation cause changes in the MR signal via T_2^* changes (18), so T_2^* images are used. Such images can be acquired with moderately good spatial resolution of 2-4 *mm* on each side for one voxel and temporal resolution with 1-4 seconds per image.

FMRI is used to produce activation maps showing which parts of the brain participate in a particular mental process (Figure 2.7). Functional activity of the brain determined from fMRI has confirmed the different function of the distinct anatomically structures such as the primary visual cortex (19, 20), the motor cortex (21, 22) and Broca's area of language related activities (23, 24, 25).

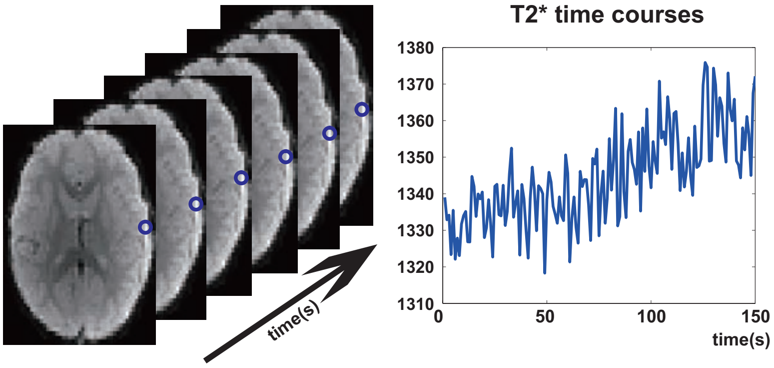

Figure 2.7: FMRI scans using T_2^* measurements are shown in the left column. The activation in the same voxel during an interval is shown in the right column.

2.3 Resting State Functional MRI Analysis

As mentioned in the previous section, functional MRI (fMRI) is used to noninvasively produce activation maps identifying brain regions involved in a particular mental process. Traditionally, researchers have focused on task-based fMRI. During the fMRI scan, the subjects were required to perform a particular task which would cause increased metabolic activity in the area of the brain responsible for that task. With these images, the relationship between brain activation and the tasks can be detected and thus the location of the brain with the task-related function can be identified. As is well known, task-based fMRI provides a remarkable tool for studying functional relationships between regions during the performance of a specific task, however, it faces some issues which need to be handled carefully (26). For instance, when the subjects are clinical populations with cognitive impairment, they may have difficulty to perform complex tasks. In addition, for developmental studies, there may be task performance difference between groups, e.g. simple tasks for adults could be hard for children, and simple tasks for children could produce ceiling effects in adults (26).

Resting state functional MRI (rsfMRI) has recently emerged as a novel and powerful tool for functional studies that can complement task-based fMRI. In resting state fMRI studies, subjects are typically required to rest quietly with their eyes closed or fixating gaze on a cross-hair for a short period of 5-10 minutes. Thus, the task performance issue for task based fMRI can be avoided and rsfMRI is particularly useful in studying functional development (27, 28). In this section, we will introduce the rsfMRI and the techniques for its analysis.

2.3.1 Resting State fMRI

During the resting state, the spontaneous low-frequency (<0.08 Hz) fluctuations (LFF) of the blood oxygenation level-dependent (BOLD) signal are presented and show high temporal correlations between spatially distinct but functionally related regions (22, 29), where the temporal correlation of signal between different brain areas is defined as functional connectivity (30). Although the true neuronal basis of the LFF under resting state is not yet fully understood, numerous studies suggested that the resting state functional network is formed by brain regions overlap in both function and neuroanatomy (31), e.g. regions of motor and visual networks (22, 32). Resting state functional MRI has been widely used to identify brain networks that are engaged during cognitive tasks as well as alterations associated with neurodegenerative diseases ((29, 33, 34) for reviews). Moreover, the default mode network, a set of regions deactivated during goal-oriented tasks (mainly composed of the bilateral posterior cingulate/precuneus, inferior parietal cortex, and ventromedial prefrontal cortex)(35), is also repeatedly found from resting state fMRI in both children and adults, linked to internal mental brain activities (36, 37, 38, 39). Resting state fMRI has now becoming an important tool for understanding the brain functional development in infants and young children (39, 40, 41, 42, 43) due to its simplicity and short scanning time. Before the introduction of data processing and analysis for resting state fMRI, one must note that as a complement for task-related fMRI in studying brain functions, resting state fMRI has the limitations of being unable to investigate task specific functions. This means that resting state fMRI can not fully replace task-related fMRI although it is simpler and easier to implement, it can only be a cooperative and complementary method for task-related fMRI to help us better understand brain functional circuits.

2.3.2 Data Preprocessing

Before analysis on the rsfMRI data, preprocessing needs to be performed as raw rsfMRI data is contaminated by motion artifacts, scanner noise and physiological noise (22, 43, 44). Except for the usual fMRI preprocessing steps such as slice timing, motion correction, skull stripping and spatial smoothing (to improve signal to noise ratio), the data need to be processed by, but not limited to, temporal filtering to get the LFF between 0.01 and 0.08 Hz, which will also help remove signal contributed by cardiac and respiratory patterns (28), and regressing out the nuisance variance (ventricular and white matter signals) (45). Some studies also perform whole-brain signal regression to account for noise sources such as motion, cardiac, and respiratory signals that globally influence the signal (46). Although preprocessing with global signal regression has been shown to increase connection specificity (43), the resultant signal has shown to introduce negative correlations (34), interpretation for the directionality of the relations should proceed with caution (47).

2.3.3 Data Analysis

There are several methods used to study the rsfMRI connectivities, such as data-driven approach, seed-based approach and graph theoretical approach.

2.3.3.1 Data-driven Approach

Data-driven methods, like independent or principal component analysis (ICA/PCA) and cluster analysis (48, 49, 50, 51), directly examine functional time series data by searching for spatiotemporal associations within the data. Of these methods, ICA is relatively popular for identifying resting state networks in the brain (52, 53). ICA is a statistical method used to discover hidden factors (sources or features) from a set of observed data such that the sources are maximally independent (54). For fMRI data, ICA decomposes the 4-dimensional BOLD signal into a group of spatially distinct maps and their associated time courses which describe the spatial and temporal characteristics of the underlying components (55). Then these findings can be validated referred to experimental design or similar external indicators for explanation (56).

ICA is widely used to detect the functional connection based on the whole brain (57, 58, 59, 60, 61, 62). For example, Fransson et al. (57) studied resting state connectivity in the brains of sedated infants under 1 year old and defined several networks similar to adults. Similarly, Thomason et al. (59) reported the default mode network (DMN) in 7- to 12-year-old children. ICA method offers advantages in detecting meaningful inter-regional correlation pattern, but the results require considerable efforts to interpret properly (56).

2.3.3.2 Seed-based Approach

Seed-based approach is another popular method in rsfMRI data analysis. It is hypothesis-driven such that one or more regions of interest (ROIs) need to be chosen and the relationship of them to the rest of brain is then defined by correlation or regression. It is applied in the first rsfMRI study where the time series of a seed ROI in the left motor cortex was correlated with the time series of all other brain voxels (22). The functional connectivity between the left and right motor cortex was demonstrated in that study without any task. Since its initial demonstration, this seed-based correlation approach has been widely applied and multiple brain networks involved in different functions have been detected in the absence of tasks (39, 41, 63). For instance, Fair et al. (39) used ROI-based analyses to examine differential connectivity related to the ventromedial prefrontal cortex (vMPFC) in children compared to adults and found that nodes within the DMN were sparsely connected in children, and strongly functionally connected in adults.

Based on the method, the resultant functional connectivity map provides the information that with which brain regions the seed ROI is functionally connected. This approach is relatively simple and the results are straightforward (64). However, the disadvantage of the method is that the information of the functional connectivity map is limited to the functional connections of the selected seed region, making it difficult to examine functional connections patterns on a whole-brain scale (31).

2.3.3.3 Graph Theoretical Approach

Emergence of rsfMRI data, which allow simultaneous examination of all brain regions and their interactions, leads to increasing interest in the application of graph metrics to characterize large-scale brain networks (43). A graph is a data structure with nodes and edges between the nodes (65). Taking the brain network as a graph G, a node N corresponds to a brain region while an edge K corresponds to the connection between 2 regions, such as the correlation between regional time series. The graph can be binary or weighted graph. To generate a binary matrix, the graph is thresholded and an edge either exists between 2 regions or does not. For the weighted matrix, the weight of an edge is usually the correlation between the 2 regions (non-negative). When analyzing binary matrix, a sequence of threshold needs to be applied to get the result while this can be avoid for weighted matrix (53). Many graph theoretical metrics provide quantitative measures to characterize the structure of these networks as a graph ((53), for a review). We outline several fundamental global and local properties of the networks in common use: characteristic path length (L_p), global efficiency (E_{glob}), clustering coefficient (C_p), betweenness centrality of node (N_{bc}) and edge (E_{bc}).

Global network metrics: To calculate the characteristic path length L_p, the distance matrix describing geodesic distances between all possible node pairs is calculated by Dijkstra's algorithm (66). L_p is calculated as the global mean of geodesic distances:

$$L_p = \frac{1}{N(N-1)} \sum_{\substack{i,j \in G \\ i \neq j}} d_{ij} ,$$

where d_{ij} is the shortest path length between nodes i and j. The path length of nodes completely disconnected with the network is set as Inf, and these nodes are excluded while computing L_p. A shorter distance means higher routing efficiency because information is exchanged via fewer steps.

Global efficiency measures the ability of a network to transmit information at the global level (67). The global efficiency is defined as

$$E_{glob} = \frac{1}{N(N-1)} \sum_{\substack{i,j \in G \\ i \neq j}} \frac{1}{d_{ij}} .$$

The larger the metric, the more efficient the network is.

Local node metrics: Nodal clustering coefficient measures the extent of inter-connectivity among the neighbors of the node. It is defined as the ratio of the number of existing connections among the node i's neighbors and all their possible connections:

$$C_i = \frac{1}{k_i(k_i-1)} \sum_{\substack{j,m \in G \\ j,m \neq i}} (a_{ij} a_{jm} a_{mi}) ,$$

where k_i is the number of nodes connecting to node i (named the degree of the node i) and the a_{ij} is the connection status between i and j: a_{ij} >0 when link between i and j exists, a_{ij} =0 otherwise (a_{ii}=0 for all i). The clustering coefficient C_p, an average of the clustering coefficients over all nodes in the network, quantifies the extent of local inter-connectivity of a network.

The Node betweenness centrality N_{bc} captures the influence that one node has over the flow of information between all other nodes in the network and can be defined as the fraction of all shortest paths in the network that pass through a given node i:

$$N_{bc}(i) = \sum_{\substack{j,k \in G \\ j \neq k \neq i}} \frac{\sigma_{kj}(i)}{\sigma_{kj}} ,$$

where σ_{kj} is the total number of shortest paths from node k to j and $\sigma_{kj}(i)$ is the number of shortest paths from node k to j that pass through node i. Nodes with high N_{bc} are important in managing the flow of information across the network because they are more likely to reside on the shortest path between other regions. Thus, a node with high centrality connecting disparate parts of the network is considered a hub in the network (68, 69).

Similarly, Edge betweenness centrality (E_{bc}) identifies critical paths in the network. Network paths with high E_{bc} are more likely to reside on the shortest path between any 2 nodes. The betweenness of an edge $E_{bc}(k,k')$ is defined as the number of shortest paths between pairs of other nodes that pass through the edge:

$$E_{bc}(k,k') = \sum_{\substack{j,k\in G \\ j,k\neq k,k'}} \frac{\sigma_{kj}(k,k')}{\sigma_{kj}},$$

where σ_{kj} is the number of shortest geodesic paths from k to j, and $\sigma_{kj}(k,k')$ is the number of shortest geodesic paths from k to j that pass through the edge (k,k').

All the properties mentioned above could be calculated using a matlab toolbox ((70), `http://www.brain-connectivity-toolbox.net`). Watts and Strogatz (71) have shown that graphs with high clustering coefficient and low characteristic path can be characterized as small-world networks, allowing for both globally and locally efficient information transfer.

Several studies have used graph theoretical approaches to characterize large-scale brain networks using rsfMRI (68, 72, 73). The whole brain functional networks were found with the small-world property in healthy adults (74, 75). It is also used in developmental studies to examine the graph metrics change with age and cognitive skill (72).

2.4 Brain Registration

Before the aforementioned image analysis can be performed, the spatial correspondence across images need to be established first. Registration is the process of transforming different images into one common coordinate system to establish this spatial correspondence. It is necessary when analyzing data obtained from different measurements, such as structural MRI (2, 76, 77, 78) and fMRI (2, 79, 80, 81). Registration of data involves both intra-subject and inter-subject models. For example, the registration of functional images to the structural images of the same subject belongs to intra-subject inter-modality registration, and the registration of structural images of different subjects to the atlas belongs to inter-subject intra-modality registration, which is frequently used in population group analysis.

This thesis focuses on inter-subject structural MRI registration, which is challenging due to high individual variation in topography of the gyri and sulci of the cerebral cortex. As the cortical folding pattern is correlated with the brain function (2), the correct registration of sulci and gyri across subjects is necessary.

Although the majority of brain registration methods are volume-based, including piecewise linear transformation (82, 83) and high dimensional transformations (84), they do not guarantee the alignment of the cortices. For instance, a small inaccuracy in volume registration may cause large inaccuracies in structural localization, especially for the sulcal and gyral patterns, e.g. for points on two sides of a sulcus (1).

On the contrary, since the sulcal and gyral landmarks are a property of the 2D cortical sheet, an alternative approach to register between subjects is to align the cortical surfaces as a 2D manifold. The surface based registration methods may differ in the features used as constraints on registration, the algorithms used to minimize unwanted distortions, and the surface geometry they operated on. The methods can be categorized according to the geometry of the surface representation being used, namely a flat 2D plane (85, 86), a sphere (2, 87) and the surface geometry itself (6, 88), which are generated after a sequence of geometrical image preprocessing algorithms like surface reconstruction, surface segmentation and structural modeling. The subsequent section will provide a brief overview of the existing brain registration methods.

2.4.1 Flattened Surface Registration

Using a flat 2D plane as the surface representation can result in a change of the original topological structure of the surface. Drury et al. (85) and Van Essen et al. (86) transformed the cortical surfaces into flattened representation and modeled it as a viscoelastic fluid sheet (89) and the registration is driven by selected landmarks that are identifiable on both source and target sheets. Although this method takes the alignment of sulcal and gyral patterns into consideration, extra artificial cuts have to be introduced to the sheet to control the distortion in order to get the flat map. This fails to preserve the topological structure of the original surface, and two close points on the opposite side of the cut may be far away on the flattened surface after the cut.

2.4.2 Spherical Surface Registration

On the other hand, the registration of the cortical surface to a sphere better maintains the original topology and can be fully automated. However, this method also introduces distortions to the original brain structures and such distortions are inconsistent over subjects. Several surface registration approaches were proposed based on the spherical surface by optimizing the alignment of shape metrics or features. For instance, Fischl et al. (2) provided an automated method for registration based on spherical representation of the cortex. The spherical representation provides a mathematically simple surface suitable for deformation. The surfaces of individual brains were transformed to spherical forms while minimizing metric distortions. These individual spherical maps were combined to construct an average map of the large-scale folding patterns on a unit sphere. An automated method then non-rigidly aligns the surface of any individual brain, converted to the spherical representation, to that average sphere using continuously varying shape metrics such as cortical convexity. Similarly, Goebel et al. (90) developed an automated method to align spheres using curvature information of the cortex. The automated methods do not require manual work, thus eliminating any inter-rater variability and are suitable for registration of large group population. Van Essen (5) proposed an alternative approach to constrain the registration using features, such as sulcal landmarks. Registration was carried out using an algorithm that deforms one spherical map to another, bringing the source landmarks into register with the atlas landmarks while minimizing shear and areal distortion in the intervening regions. This landmark-based method is flexible because people can customize the registration features based on their particular study needs. Recently, Yeo et al. (91, 92) developed a spherical demons algorithm with the computational intensity extensively decreased and no landmarks involved. The deformation space is restricted to be a composition of diffeomorphisms, each parameterized by a stationary velocity field. In each iteration, the method greedily seeks the locally optimal diffeomorphism to be composed with the current transformation, which makes the resulting registration method fast. It has been shown that spherical surface-based registration is superior to volume-based registration in fMRI group analysis (9, 93).

The spherical brain registration approaches mentioned above all require a spherical representation of the brain before registration. This step would introduce large distortion of the brain structure, which does not appear consistently across subjects. As a consequence, matching would begin with such a distortion error. Direct alignment of the cortical surfaces in their own coordinates has been proposed to avoid such distortions.

2.4.3 Original Surface Registration

Cortical surface registration directly based on its original representation can avoid conventional intermediate parameterizations (e.g. flat map or spherical map) and help to simplify the cortical registration process. As the sulci and gyri preserve the sulco-gyral pattern of the cortical surface, several methods are proposed based on sulcal and gyral landmarks. Shi et al. (6) proposed a surface registration method that extrapolated sulcal line deformations to a full cortical surface based on implicit harmonic mappings that minimize a surface-to-surface deformation energy. While this method needs one-to-one correspondences between curves on different cortices, Qiu et al. (88) and Glaunѐs et al. (8) developed a cortical registration method using Large Deformation Diffeomorphic Metric Mapping (LDDMM) curve registration algorithm where exact correspondence between paired curves is not required.

The advantage of such techniques is that the registration results are independent of the intermediate space (e.g. flat, sphere, or equivalently, the specific parameterization of the cortex) resulting in a more consistently accurate registration throughout the cortex. Of these methods, the LDDMM framework is attractive because the diffeomorphic transformations have the following desirable properties, (a) it is one-to-one: disjoint sets remain disjoint; (b) it is continuous: connected sets remain connected, and (c) it is smooth: smoothness of features is preserved and coordinates are transformed consistently. The LDDMM approach is effectively unconstrained by degrees of freedom, it seeks diffeomorphisms parameterized by time-varying velocity fields, on which a smoothness constraint is imposed for regularization.

Nevertheless, previous LDDMM algorithms for surface registration (8, 88, 94, 95) make the examination of shape variability very difficult as they optimize time-dependent momenta along a diffeomorphic trajectory, where the shape space of surface is in fact a nonlinear metric space. Moreover, although the sulci and gyri are related to the sulco-gyral pattern of the cortex, they are only a coarse representation of the cortex. Based on the variability across subjects, only some curves are continuously present, thus one can not draw as many curves as possible to represent the cortex. The curves can only control the local alignment in the region around the curves. As the whole cortical surface registration better controls about the global information, it is expected that combining surface and cortical information together would get better alignment of the whole cortical surface.

2.5 LDDMM Framework

In the setting of LDDMM, the set of anatomical shapes are placed into a metric shape space. This is modeled by assuming that the shape is generated one from the other via a flow of diffeomorphisms, solutions of ordinary differential equations $\dot{\phi}_t = v_t(\phi_t), t \in [0,1]$, starting from the identity map $\phi_0 = \text{id}$, and associated velocity vector fields $v_t, t \in [0,1]$. We define a metric distance between target shape I_{targ} and template shape I_{temp} as the length of the geodesic curves $\phi_t \cdot I_{temp}, t \in [0,1]$, through the shape space such that $\phi_1 \cdot I_{temp} = I_{targ}$ at time $t = 1$. These geodesics $\phi_t \cdot I_{temp}, t \in [0,1]$, are generalizations of simple finite dimensional curves. The metric between two shapes I_{temp}, I_{targ} takes the form

$$\rho(I_{temp}, I_{targ})^2 = \inf_{v_t : \dot{\phi}_t = v_t(\phi_t), \phi_0 = \text{id}} \int_0^1 \|v_t\|_V^2 dt \quad \text{such that } \phi_1 \cdot I_{temp} = I_{targ} \tag{2.1}$$

where $v_t \in V$, a Hilbert space with kernel k_V and norm $\|\cdot\|_V$. To ensure solutions are diffeomorphisms, V must be a space of smooth vector fields (96, 97).

2.5.1 Variational Formulation

In practice, the metric ρ and the diffeomorphic correspondence $\phi = \phi_1$ between the template shape I_{temp} and target shape I_{targ} are calculated via a variational formulation of the "inexact matching problem". Associate for each pair (I_{temp}, I_{targ}), a norm-squared cost is $E(\phi_1 \cdot I_{temp}, I_{targ})$; then the variational problem requires minimization of the functional

$$J(v_t) = \inf_{v_t : \dot{\phi}_t = v_t(\phi_t), \phi_0 = \text{id}} \int_0^1 \|v_t\|_V^2 dt + \beta E(\phi_1 \cdot I_{temp}, I_{targ}). \tag{2.2}$$

The first term in Eq. 2.2 is a regularization term to guarantee the smoothness of deformation fields and the second term is a matching functional to quantify the mismatching between the objects $\phi_1 \cdot I_{temp}$ and I_{targ}. β is a trade-off parameter. Then the general solution to this variational problem can be written in the form of

$$v_t(x) = \sum_{i=1}^{n} k_V(x_i(t), x)\alpha_i(t) \tag{2.3}$$

where $\alpha_i(t)$ are referred to as *momentum vectors*, which are analogous to the momentum in fluid mechanics. These momentum vectors can be computed from trajectories $x_i(t)$ by solving the system of linear equations

$$\frac{dx_i(t)}{dt} = \sum_{j=1}^{m} k_V(x_i(t), x_j(t))\alpha_j(t), i = 1, 2, \ldots, n \tag{2.4}$$

2.5.2 Vector-valued Measure

Since both curve and surface are geometric objects, previous studies (8, 98, 99, 100, 101, 102) have associated the geometry of curves and surfaces with vector-valued measures, $\mu_{\mathbf{x}} = \sum_i w_i \otimes \delta_{x_i}$, such that for all vector fields, u, in a reproducing kernel Hilbert space, W, with reproducing kernel k_W, $\langle \mu_{\mathbf{x}}, u \rangle_2 = \sum_i \langle w_i, u(x_i) \rangle_2$. δ indicates the Dirac measure and for 3D curves and surfaces, w_i are 3D vectors.

A curve cannot be uniquely reconstructed based on the locations of a set of points. We assume a curve embedded in $\mathcal{R}^3$ is a one-dimensional manifold in the sense that the local region of every point on the curve is equivalent to a line which can be uniquely defined by this point and the unit tangent vector at this location. Thus, for the curve case, w_i is the tangent vector at x_i with length. Similarly, we assume the cortical surfaces embedded in $\mathcal{R}^3$ to be a two-dimensional manifold in the sense that the neighborhood of every point on the surface is equivalent to a two-dimensional plane in Euclidean space. Such a plane can be uniquely defined by a point and a vector originated at this point and normal to the plane. Therefore, for the surface case, w_i is the normal vector at x_i. The action of ϕ_1 on the discrete measure $\mu_{\mathbf{x}}$ is given by

$$\phi_1 \cdot \mu_{\mathbf{x}} = \sum_i (\phi_1 \cdot w_i) \otimes \delta_{\phi_1(x_i)} \ .$$

We use a kernel norm to compare $\phi_1 \cdot \mu_{\mathbf{x}}$ and $\mu_{\mathbf{y}}$. Let k_W be a kernel and $\mu_{\mathbf{x}}$ be a measure. In practice, we often use a Gaussian kernel such that $k_W(x, y) = e^{-\frac{\|x-y\|^2}{2\sigma_W^2}}$.We define

$$\|\mu_x\|_{k_W}^2 = \sum_i \sum_j w_i^* [k_W(x_i, x_j) w_j].$$

The W in the notation comes from the fact that k_W can be interpreted as the reproducing kernel of a vector space (W) of smooth vector-valued functions and $\|.\|_{k_W}$ is then the dual norm (7, 103, 104, 105). We will let

$$E(\phi_1 \cdot \mathbf{x}, \mathbf{y}) = \|\phi_1 \cdot \mu_{\mathbf{x}} - \mu_{\mathbf{y}}\|_{k_W}^2 \ . \tag{2.5}$$

With $\mu_{\mathbf{x}} = \sum_{i=1}^{n} w_i \otimes \delta_{x_i}$ and $\mu_{\mathbf{y}} = \sum_{j=1}^{m} \tilde{w}_j \otimes \delta_{y_j}$, this is equal to

$$\begin{aligned} E(\phi_1 \cdot \mathbf{x}, \mathbf{y}) \quad = \quad & \sum_{i=1}^{n} \sum_{j=1}^{n} (\phi_1 \cdot w_i)^* [k_W(\phi_1(x_i), \phi_1(x_j))(\phi_1 \cdot w_j)] \\ & -2 \sum_{i=1}^{n} \sum_{j=1}^{m} (\phi_1 \cdot w_i)^* [k_W(\phi_1(x_i), y_j)\tilde{w}_j] \\ & + \sum_{i=1}^{m} \sum_{j=1}^{m} \tilde{w}_i^* [k_W(y_i, y_j)\tilde{w}_j] \, . \end{aligned} \tag{2.6}$$

The first and last terms enforce structural integrity of the two shapes, while the middle term penalizes geometric and spatial mismatch.

We now briefly describe how this representation is implemented with curves and surfaces in the discrete setting (details about the continuous case in (104, 105)). For the sake of simplicity, here we only discuss one pair of curves, γ_{temp} and γ_{targ}, and one pair of surfaces, S_{temp} and S_{targ}.

Curves: When each curve is represented by a sequence of points, still denoted as $\gamma_{temp} = \mathbf{x} = (x_i)_{i=1}^{n}$ and $\gamma_{targ} = \mathbf{y} = (y_j)_{j=1}^{m}$, we use the representation (7, 105)

$$\mu_{\mathbf{x}} = \sum_{j=1}^{n-1} w_j \otimes \delta_{c_j}$$

with $c_j = (x_{j+1} + x_j)/2$ and $w_j = x_{j+1} - x_j$, and similarly for $\mathbf{y}$. The action of ϕ_1 on the discrete measure μ_x is given by

$$\phi_1 \cdot \mu_{\mathbf{x}} = \sum_{j=1}^{n-1} (\phi_1 \cdot w_j) \otimes \delta_{\phi_1(c_j)},$$

where $\phi_1 \cdot w_j$ is approximated as $\phi_1(x_{j+1}) - \phi_1(x_j)$ at the center $\phi_1(c_j) = (\phi_1(x_{j+1}) + \phi_1(x_j))/2$. The representation in terms of vector-valued measure is sensitive to both the location and the first order local geometry of the curve.

Surfaces: Now, let S_{temp} and S_{targ} be triangulated meshes with vertices $\mathbf{x} = (x_i)_{i=1}^{n}$ and $\mathbf{y} = (y_j)_{j=1}^{m}$, respectively. Then we let (104, 106)

$$\mu_{\mathbf{x}} = \sum_{f \in \mathcal{F}_{\mathbf{x}}} w_{c_f} \otimes \delta_{c_f} \, ,$$

where $\mathcal{F}_{\mathbf{x}}$ is the set of faces in the triangulation, and, for a positively ordered face $f = (x_{f_1}, x_{f_2}, x_{f_3})$,

$w_{c_f} = \frac{1}{2}(x_{f_1} - x_{f_2}) \times (x_{f_3} - x_{f_1})$ and $c_f = \frac{1}{3}(x_{f_1} + x_{f_2} + x_{f_3})$, where × denotes cross product; $\mu_{\mathbf{y}}$ is defined similarly. The action of ϕ_1 on the discrete measure $\mu_{\mathbf{x}}$ is given by

$$\phi_1 \cdot \mu_{\mathbf{x}} = \sum_{f \in \mathcal{F}_{\mathbf{x}}} (\phi_1 \cdot w_{c_f}) \otimes \delta_{\phi_1(c_f)},$$

where $\phi_1 \cdot w_{c_f}$ is approximated as $1/2(\phi_1(x_{f_1}) - \phi_1(x_{f_2})) \times (\phi_1(x_{f_3}) - \phi_1(x_{f_1}))$ and $\phi_1(c_f) = 1/3(\phi_1(x_{f_1}) + \phi_1(x_{f_2}) + \phi_1(x_{f_3}))$. Here again, the representation makes a direct use of the geometry of the point set as a triangulated surface. Note that the definitions of $\mu_{\mathbf{x}}$ in the curve and surface cases come from discretizations of mathematical objects called currents, as described by (8, 104).

3

MM-LDDMM Registration

While previous LDDMM methods for surface registration (7, 99, 105, 106) were only based on either curves or surface which failed to control both the local and global information together, a method which can make up this disadvantage is needed. Based on the previous LDDMM framework, in this chapter, we would develop a surface registration method by combining curves and surface together for controlling the quality of local and global deformation.

3.1 Introduction

The human cortex is a convoluted sheet that forms sulco-gyral folding patterns to allow a large surface area inside the skull. Because of this, functionally distinct regions are close to each other in volume space but geometrically distant in terms of distance measured along the cortex. Such geometric property of the cortex has been well preserved in the cortical surface model (86, 107, 108, 109, 110). Thus, surface-based analysis, in particular, surface-based registration for optimizing the alignment of anatomical and functional data across individuals, has received great attention in both anatomical and functional studies in magnetic resonance imaging (MRI) (2, 5, 7, 86, 111, 112).

Most of the advanced cortical surface registration approaches have been implemented in the spherical coordinates based on either the folding pattern (2, 111) or landmarks (sulcal or gyral curves) (5, 7, 101, 112).They have been applied in brain morphometric studies for not only exploring abnormalities in the cortical folding and thickness associated with disease but also providing the locations (e.g. (113, 114, 115)). Previous fMRI works using the surface registration approaches have shown superior power in detecting functional activations when compared with volume-based registration approaches (2, 108, 116). In particular, the landmark-based spherical mappings provide flexibility to choose sulcal or gyral curves in functional activation areas for the improvement of the alignment in regions of interest (ROIs) (7, 101, 116, 117, 118) even though the gyral or sulcal curves are the coarse representation of the cortex. Nevertheless, the landmark or folding pattern based spherical mappings require the spherical reparametrization of the cortical surface in which adjacent gyri with distinct functions are well separated. This surface reparametrization process introduces large distance and area distortion that potentially affects the quality of the surface alignment. To avoid such distortion, one would expect to directly align the cortical surfaces in their own coordinates.

In 2005, Vaillant and Glaunès (104) first introduced a vector-valued measure acting on vector fields as geometric representation of surfaces and then imposed a Hilbert space structure on it, whose norm was used to quantify the geometric similarity between two surfaces in their own coordinates. Since then, the vector-valued measure has been incorporated as matching functional into large deformation diffeomorphic metric mapping (LDDMM) variational problems for aligning curves or surfaces (7, 105, 106) where time-dependent momenta were found to describe trajectories connecting one object to another. Moreover, Durrleman et. al. have recently derived a sparse approximation of the vector-valued measure, which offered a way to visualize and interpret statistics on shapes of curves and surfaces (100, 102).

Following these previous works, we introduced a multi-manifold large deformation diffeomorphic metric mapping (MM-LDDMM) algorithm for morphing the cortical hemispheric surfaces by integrating the vector-valued measures of sulcal curves (1-dimensional manifold) and cortical surfaces (2-dimensional manifold) in this thesis. Unlike the previous LDDMM algorithms (7, 95, 105) optimizing time-dependent momenta along a diffeomorphic trajectory, we present an algorithm based on recent derivation of a conservation of momentum law for the geodesics of diffeomorphic flow (119, 120). Once a template is fixed, the space of initial momentum becomes an appropriate space for studying shape via geodesic flow since the flow at any point on curves and surfaces along the geodesic is completely determined by the momentum at the origin. We solve for trajectories (geodesics) of the kinetic energy by computing its variation with respect to the initial momentum and by applying a gradient descent scheme. The initial momentum represents shapes of a population in a linear space as has been done for landmarks in (121), which provides a natural way to compute mean shape through its average.

In this chapter, we will first review the conservation of momentum law and geodesic flow equation associated with objects represented by points (e.g., curves, surfaces). We will then define the kinetic energy of the MM-LDDMM algorithm with respect to the initial momentum and its Euler-Lagrange equation. To apply the MM-LDDMM algorithm for the cortical hemispheric registration, we will present a procedure that defines sulcal curves for improving the quality of regional alignment and the cortical surface for controlling the quality of global as well as regional alignment. Finally, we will compare mapping results of the MM-LDDMM algorithm with those of the LDDMM-curve and LDDMM-surface algorithms using 40 MRI datasets.

3.2 Method

3.2.1 Geodesic Shooting with Initial Momentum in Diffeomorphisms

Based on the previous review on the LDDMM framework in section 2.5, we know that the metric between two shapes I_{temp}, I_{targ} is determined by the integrated norm $||v_t||_V$ of the vector field generating the transformation, where $v_t \in V$, a smooth Hilbert space with kernel k_V and norm $||\cdot||_V$. To ensure solutions are diffeomorphisms, V must be a space of smooth vector fields (96, 97). Equivalently, the metric distance can be computed through m_t, termed the momentum, a linear transformation of v_t defined by the kernel, $k_V : v_t \rightarrow m_t = k_V^{-1} v_t$ according to

$$\begin{aligned} \rho(I_{temp}, I_{targ})^2 &= \inf_{v_t : \dot{\phi}_t = v_t(\phi_t), \phi_0 = \mathrm{id}} \int_0^1 ||v_t||_V^2 dt \quad \text{such that } \phi_1 \cdot I_{temp} = I_{targ} \qquad (3.1) \\ &= \inf_{m_t : \dot{\phi}_t = k_V m_t(\phi_t), \phi_0 = \mathrm{id}} \int_0^1 \langle m_t, k_V m_t \rangle_2 dt \quad \text{such that } \phi_1 \cdot I_{temp} = I_{targ} \ . \end{aligned}$$

In practice, we often use a Gaussian kernel such that $k_V(x, y) = e^{-\frac{||x-y||^2}{2\sigma_V^2}}$, and $\langle \ \rangle_2$ represents the L2 inner product.

A geodesic equation in this diffeomorphic group (starting from the identity in the direction v_0) can be characterized by a conservation equation that relates to the conservation of momentum (122). It can be proved that the momentum, m_t, along the geodesic, ϕ_t, satisfies the property (119, 120): for all $u \in V$,

$$\langle m_t, u \rangle_2 = \langle m_0, (D\phi_t)^{-1} u(\phi_t) \rangle_2,$$

where D is the Jacobian matrix. This equation uniquely specifies m_t as a linear form on V, given the initial momentum and the evolving diffeomorphism, ϕ_t. In other words, a change of variables provides the expression that the initial momentum m_0 encodes the geodesic connecting I_{temp} and I_{targ} according to

$$m_t = |D\phi_t^{-1}|(D\phi_t^{-1})^* m_0 \circ \phi_t^{-1} , \tag{3.2}$$

where $*$ denotes transpose and $\circ$ represents composition. This implies $\langle m_t, k_V m_t \rangle_2 = \langle m_0, k_V m_0 \rangle_2$ for all time t. We can thus define a variational problem equivalent to Eq. (3.1) as

$$\begin{aligned} \rho(I_{temp}, I_{targ})^2 &= \inf_{m_0 : \dot{\phi}_t = k_V m_t(\phi_t), \phi_0 = \mathrm{id}} \langle m_0, k_V m_0 \rangle_2 \\ &\quad \text{such that } \phi_1 \cdot I_{temp} = I_{targ} , \end{aligned} \tag{3.3}$$

where m_t is constructed based on Eq. (3.2).

If $I_{temp} = \mathbf{x} = (x_i)_{i=1}^n$ and $I_{targ} = \mathbf{y} = (y_i)_{i=1}^m$ are the point sets on the objects of I_{temp} and I_{targ}, where I_{temp} and I_{targ} can be labeled or unlabeled landmarks, curves, or surfaces, then the momentum, m_t, becomes singular and is defined as a sum of Dirac measures

$$m_t = \sum_{i=1}^{n} \alpha_i(t) \otimes \delta_{x_i(t)} , \tag{3.4}$$

such that for any $u \in V$, $\langle m_t, u \rangle_2 = \sum_{i=1}^n \langle \alpha_i(t), u(x_i(t)) \rangle_2$, where $x_i(t) = \phi_t(x_i)$ and $\alpha_i(t)$ is the momentum vector of the i^{th} point at time t. The law of momentum conservation in Eq. (3.2), implies that the momentum in the point-based LDDMM mappings satisfies the dynamic systems given by

$$\frac{d\alpha_i(t)}{dt} = -\sum_{j=1}^{n} \alpha_i(t)^* \alpha_j(t) \nabla_1 k_V(x_i(t), x_j(t)), i = 1, 2, \cdots, n . \tag{3.5}$$

where ∇_1 denotes the gradient of k_V with respect to its first variable. This has been referred as geodesic shooting with the flow equation

$$\frac{dx_i(t)}{dt} = \sum_{j=1}^{n} k_V(x_i(t), x_j(t)) \alpha_j(t) . \tag{3.6}$$

This indicates that the geodesic connecting $\mathbf{x}$ and $\mathbf{y}$ can be generated given the initial momentum $\alpha_i(0)$ and $x_i(0)$. Thus, Eq. (3.3) is simplified as

$$\rho(\mathbf{x}, \mathbf{y})^2 = \inf_{\alpha_0, \phi_0 = \mathrm{id}} \sum_{i=1}^{n} \sum_{j=1}^{n} \alpha_j(0)^* [k_V(x_i(0), x_j(0)) \alpha_i(0)] \quad \text{such that } \phi_1 \cdot \mathbf{x} = \mathbf{y} , \tag{3.7}$$

where $\alpha_i(t)$ and $x_i(t)$ are constructed through the geodesic shooting given in Eq. (3.5) and (3.6).

3.2.2 Multi-Manifold Large Deformation Diffeomorphic Metric Mapping (MM-LDDMM)

To control both the global and local alignment of the surface, we now propose a variational problem, multi-manifold large deformation diffeomorphic metric mapping (MM-LDDMM), that seeks optimal initial momentum for generating unified diffeomorphic vectors (v_t) over the ambient space based on multiple anatomical manifolds such as curves and surfaces. The MM-LDDMM requires minimization of the functional

$$\begin{aligned} J(\boldsymbol{\alpha_0}) &= \inf_{\boldsymbol{\alpha_0},\phi_0=\mathrm{id}} \sum_{i=1}^{n}\sum_{j=1}^{n} \alpha_j(0)^*[k_V(x_i(0),x_j(0))\alpha_i(0)] \\ &\quad + \sum_{i=1}^{n_c}\beta_{\gamma_i}E_{\gamma_i}(\phi_1\cdot\gamma^i_{temp},\gamma^i_{targ}) + \sum_{i=1}^{n_s}\beta_{S_i}E_{S_i}(\phi_1\cdot S^i_{temp},S^i_{targ})\ , \end{aligned} \tag{3.8}$$

where $\alpha_i(t)$ and $x_i(t)$ satisfy the geodesic shooting equations (3.5) and (3.6). n_c and n_s are numbers of curves and surfaces incorporated in the mapping. $E_{\gamma_i}(\phi_1\cdot\gamma^i_{temp},\gamma^i_{targ})$ and $E_{S_i}(\phi_1\cdot S^i_{temp},S^i_{targ})$ are matching functionals that respectively quantify the closeness between curve γ^i_{targ} and deformed curve $\phi_1\cdot\gamma^i_{temp}$ and between surface S^i_{targ} and deformed surface $\phi_1\cdot S^i_{temp}$, which are defined in section 2.5.2 via vector-valued measures (8, 98, 99, 100, 101, 102). β_{γ_i} and β_{S_i} are the trade-off parameters respectively for curve closeness and surface closeness.

3.2.2.1 Euler-Lagrange Equation of the MM-LDDMM

Lemma 1 (MM-LDDMM Solution)**.** *The point-based multi-manifold LDDMM algorithm minimizes the energy Eq. (3.8) with respect to the initial momentum,* $\boldsymbol{\alpha_0}=(\alpha_i(0))_{i=1}^n$ *, when the variables* $\mathbf{x}_t=(x_i(t))_{i=1}^n$ *and* $\boldsymbol{\alpha_t}=(\alpha_i(t))_{i=1}^n$ *satisfy the shooting equations in Eqs. (3.5) and (3.6). Its Euler-Lagrange optimality conditions imply*

$$\nabla J = 2k_V(\mathbf{x}_0,\mathbf{x}_0)\alpha_0+\boldsymbol{\eta_0}^{\alpha}=0 \tag{3.9}$$

where $\boldsymbol{\eta_0}^{\alpha}$ *at* $t=0$ *is obtained by solving the ODE system in Eq. (3.12) backwards with conditions* $\boldsymbol{\eta_1}^{\alpha}=0$ *and* $\boldsymbol{\eta_1}^{\mathbf{x}}=\sum_{i=1}^{n_c}\beta_{\gamma_i}d_{\mathbf{x}_1}E_{\gamma_i}+\sum_{i=1}^{n_s}\beta_{S_i}d_{\mathbf{x}_1}E_{S_i}$*.* $d_{\mathbf{x}_1}E_i$ *at* $t=1$*.* $d_{\mathbf{x}_1}E_i$ *is the derivative of* E_i *with respect to* $\mathbf{x}_1$*.*

Proof. For simplicity, assume $\boldsymbol{\alpha_t}=(\alpha_i(t))_{i=1}^n$ to be a vector with all elements of $\alpha_i(t)$ and $\mathbf{x}_t=(x_i(t))_{i=1}^n$ to be a vector with all elements of $x_i(t)$. We thus rewrite the MM-LDDMM variational problem in Eq. (3.8) into a matrix form:

$$J = \boldsymbol{\alpha}_{\mathbf{0}}^{*}[k_V(\mathbf{x}_0, \mathbf{x}_0)\boldsymbol{\alpha}_{\mathbf{0}}] + \sum_{i=1}^{n_c} \beta_{\gamma_i} E_{\gamma_i} + \sum_{i=1}^{n_s} \beta_{S_i} E_{S_i} \; .$$

We consider a variation $\boldsymbol{\alpha}_{\mathbf{0}}^{\epsilon} = \boldsymbol{\alpha}_{\mathbf{0}} + \epsilon\tilde{\boldsymbol{\alpha}}_{\mathbf{0}}$ and denote the corresponding variation in $\mathbf{x}_1$ as $\tilde{\mathbf{x}}_1$. Our goal is to express the derivative of J with respect to ϵ as a function of $\tilde{\boldsymbol{\alpha}}_{\mathbf{0}}$. We get

$$\partial_\epsilon J \;\; = \;\; 2\tilde{\boldsymbol{\alpha}}_{\mathbf{0}}^{*}[k_V(\mathbf{x}_0, \mathbf{x}_0)\boldsymbol{\alpha}_{\mathbf{0}}] + \sum_{i=1}^{n_c} \beta_{\gamma_i} \tilde{\mathbf{x}}_1^{*} d_{\mathbf{x}_1} E_{\gamma_i} + \sum_{i=1}^{n_s} \beta_{S_i} \tilde{\mathbf{x}}_1^{*} d_{\mathbf{x}_1} E_{S_i} \; .$$

We now study the variation of $\mathbf{x}_t$ through the geodesic shooting equations in Eqs. (3.5) and (3.6). Rewrite them in a matrix form:

$$\begin{aligned} \frac{d\mathbf{x}_t}{dt} &= k_V(\mathbf{x}_t, \mathbf{x}_t)\boldsymbol{\alpha}_t \\ \frac{d\boldsymbol{\alpha}_t}{dt} &= -\boldsymbol{\alpha}_t^{*}[\boldsymbol{\alpha}_t \nabla_1 k_V(\mathbf{x}_t, \mathbf{x}_t)] \end{aligned}$$

Taking the derivative of both sides with respect to the variation in $\boldsymbol{\alpha}_{\mathbf{0}}$ implies a first order variation in $\mathbf{x}_t$ and $\boldsymbol{\alpha}_t$, that we denote $\tilde{\mathbf{x}}_t$ and $\tilde{\boldsymbol{\alpha}}_t$, with

$$\begin{aligned} \frac{d\tilde{\mathbf{x}}_t}{dt} &= \partial_{\mathbf{x}_t}[k_V(\mathbf{x}_t, \mathbf{x}_t)\alpha_t]\tilde{\mathbf{x}}_t + k_V(\mathbf{x}_t, \mathbf{x}_t)\tilde{\alpha}_t \\ \frac{d\tilde{\boldsymbol{\alpha}}_t}{dt} &= -(\tilde{\boldsymbol{\alpha}}_t^{*}\boldsymbol{\alpha}_t + \boldsymbol{\alpha}_t^{*}\tilde{\boldsymbol{\alpha}}_t)\nabla_1 k_V(\mathbf{x}_t, \mathbf{x}_t) - \boldsymbol{\alpha}_t^{*}\partial_{\mathbf{x}_t}[\boldsymbol{\alpha}_t \nabla_1 k_V(\mathbf{x}_t, \mathbf{x}_t)]\tilde{\mathbf{x}}_t \; , \end{aligned}$$

where $\partial_{\mathbf{x}_t}$ represents taking partial derivative with respect to $\mathbf{x}_t$. Rearrange this first-order differential equations into the form of

$$\frac{d}{dt}\begin{pmatrix} \tilde{\mathbf{x}}_t \\ \tilde{\boldsymbol{\alpha}}_t \end{pmatrix} = H(t)\begin{pmatrix} \tilde{\mathbf{x}}_t \\ \tilde{\boldsymbol{\alpha}}_t \end{pmatrix} , \tag{3.10}$$

where H is a coefficient matrix that depends on $\mathbf{x}(t)$ and $\boldsymbol{\alpha}(t)$. Given initial conditions $\tilde{\boldsymbol{x}}_0 = 0, \tilde{\boldsymbol{\alpha}}_{\mathbf{0}}$, its general solution is written as

$$\begin{pmatrix} \tilde{\mathbf{x}}_t \\ \tilde{\alpha}_t \end{pmatrix} = M_{0t}\begin{pmatrix} 0 \\ \tilde{\alpha}_0 \end{pmatrix} = \begin{pmatrix} M_{0t}^{(1)} & M_{0t}^{(2)} \\ M_{0t}^{(3)} & M_{0t}^{(4)} \end{pmatrix}\begin{pmatrix} 0 \\ \tilde{\alpha}_0 \end{pmatrix} , \tag{3.11}$$

where $M_{0t}^{(1)}, M_{0t}^{(2)}, M_{0t}^{(3)}, M_{0t}^{(4)}$ are block matrices of M_{0t} associated with $\tilde{\mathbf{x}}_0$ and $\tilde{\alpha}_t$. We get

$$\tilde{\mathbf{x}}_t = M_{01}^{(2)}\tilde{\alpha}_0 \; .$$

Thus, we have

$$\begin{aligned}\partial_\epsilon J &= 2\tilde{\alpha}_0^*[k_V(\mathbf{x}_0,\mathbf{x}_0)\boldsymbol{\alpha}_\mathbf{0}] + (M_{01}^{(2)}\tilde{\alpha}_0)^*\Big(\sum_{i=1}^{n_c}\beta_{\gamma_i}d_{\mathbf{x}_1}E_{\gamma_i} + \sum_{i=1}^{n_s}\beta_{S_i}d_{\mathbf{x}_1}E_{S_i}\Big) \\ &= 2\tilde{\alpha}_0^*[k_V(\mathbf{x}_0,\mathbf{x}_0)\boldsymbol{\alpha}_\mathbf{0}] + \tilde{\alpha}_\mathbf{0}^*\Big[(M_{01}^{(2)})^*\Big(\sum_{i=1}^{n_c}\beta_{\gamma_i}d_{\mathbf{x}_1}E_{\gamma_i} + \sum_{i=1}^{n_s}\beta_{S_i}d_{\mathbf{x}_1}E_{S_i}\Big)\Big],\end{aligned}$$

Using $M_{st}M_{ts} = Id$, we have

$$\frac{\partial}{\partial S}M_{st} = -M_{st}H(s)$$

so that, for any vector $\boldsymbol{\eta}$,

$$\frac{\partial}{\partial S}M_{st}^*\boldsymbol{\eta} = -H(s)^*M_{st}^*\boldsymbol{\eta}$$

This implies that the vector

$$M_{01}^*\begin{pmatrix} \sum_{i=1}^{n_c}\beta_{\gamma_i}d_{x_1}E_{\gamma_i} + \sum_{i=1}^{n_s}\beta_{S_i}d_{x_1}E_{S_i} \\ 0 \end{pmatrix}$$

can be computed as the solution of

$$\frac{d}{dt}\begin{pmatrix} \boldsymbol{\eta_t}^\mathbf{x} \\ \boldsymbol{\eta_t}^\alpha \end{pmatrix} = -H(t)^*\begin{pmatrix} \boldsymbol{\eta_t}^\mathbf{x} \\ \boldsymbol{\eta_t}^\alpha \end{pmatrix}, \tag{3.12}$$

with conditions of $\boldsymbol{\eta_1}^\mathbf{x} = \sum_{i=1}^{n_c}\beta_{\gamma_i}d_{\mathbf{x}_1}E_{\gamma_i} + \sum_{i=1}^{n_s}\beta_{S_i}d_{\mathbf{x}_1}E_{S_i}$ and $\boldsymbol{\eta_1}^\alpha = 0$ at $t = 1$(this equation must therefore be solved backwards in time).

Therefore, the gradient of J can be written as

$$\nabla J = 2k_V(\mathbf{x}_0,\mathbf{x}_0)\boldsymbol{\alpha}_\mathbf{0} + \boldsymbol{\eta_0}^\alpha\ .$$

□

3.2.2.2 Implementation

We use a conjugate gradient routine to perform the minimization of functional J in (3.8) with respect to variables $\alpha_i(0)$. Of course any other optimization scheme could be considered at this point. During each iteration, the functional and its gradient are updated in the following steps:

1. compute trajectory $\mathbf{x}_t$ based on the geodesic shooting equations in (3.5), (3.6) with initial conditions $\mathbf{x}_0 = \mathbf{x}_{temp}$ and $\boldsymbol{\alpha}_\mathbf{0}$;

2. compute $d_{\mathbf{x}_1} E_{\gamma_i}$ and $d_{\mathbf{x}_1} E_{S_i}$;
3. compute vectors $\boldsymbol{\eta_t}^{\alpha}$ by solving the system of ODE in Eq. (3.12);
4. compute gradient $\nabla J = 2k_V(\mathbf{x}_0, \mathbf{x}_0)\alpha_0 + \boldsymbol{\eta_0}^{\alpha}$.

All time-dependent variables were evaluated on a uniform grid $t_1 = 0, \ldots, t_T = 1$ and a predictor/corrector centered Euler scheme was used to solve the systems of ODE in Eqs. (3.5), (3.6), and (3.12). The complexity of each iteration is of order N^2. To speed up computations when N is large, all convolutions by kernels k_V and k_W are accelerated with fast Gaussian Transform (123) when k_V and k_W are chosen as Gaussian kernels, which reduces the complexity to $N \log(N)$.

3.2.3 Cortical Registration Process via the MM-LDDMM

In the cortical hemispherical registration, one expects that gyri or sulci appearing in every subject, such as the central sulcus, the Sylvian fissure, etc, can be well matched along with the cortical hemispherical surface. Thus, fourteen sulcal curves and the cortical hemispheric surface are considered as geometric objects in the MM-LDDMM algorithm for improving the quality of global and regional alignment. These fourteen curves (definitions given in Appendix A.1), including superior frontal sulcus (SFS), inferior frontal sulcus (IFS), precentral sulcus (PreCeS), central sulcus (CeS), postcentral sulcus (PostCeS), Sylvian fissure (SF), anterior segment of the superior temporal sulcus (aSTS), inferior temporal sulcus (ITS), intraparietal sulcus (IPS), calcarine sulcus (CaS), parieto-occipital fissure (POF), collateral sulcus (CLS), superior callosal sulcus (CC), and olfactory sulcus (OS), are chosen as curve objects because they are consistently present and are readily identifiable on the cortical surface (115, 124).

Given an T1-weighted MR image, we first apply FreeSurfer to extract the triangulated mesh at the boundary between the gray matter and white matter (4, 108). Then, these sulcal curves are tracked on the cortical surface using dynamic programming after the starting and ending points of each curve are manually labeled (125). Figure 3.1 shows these curves in the lateral, medial, and basal views on the left and right cortical surfaces. These sulcal curves are served as constraints in the cortical registration process.

We design a four-step process for the cortical surface registration:

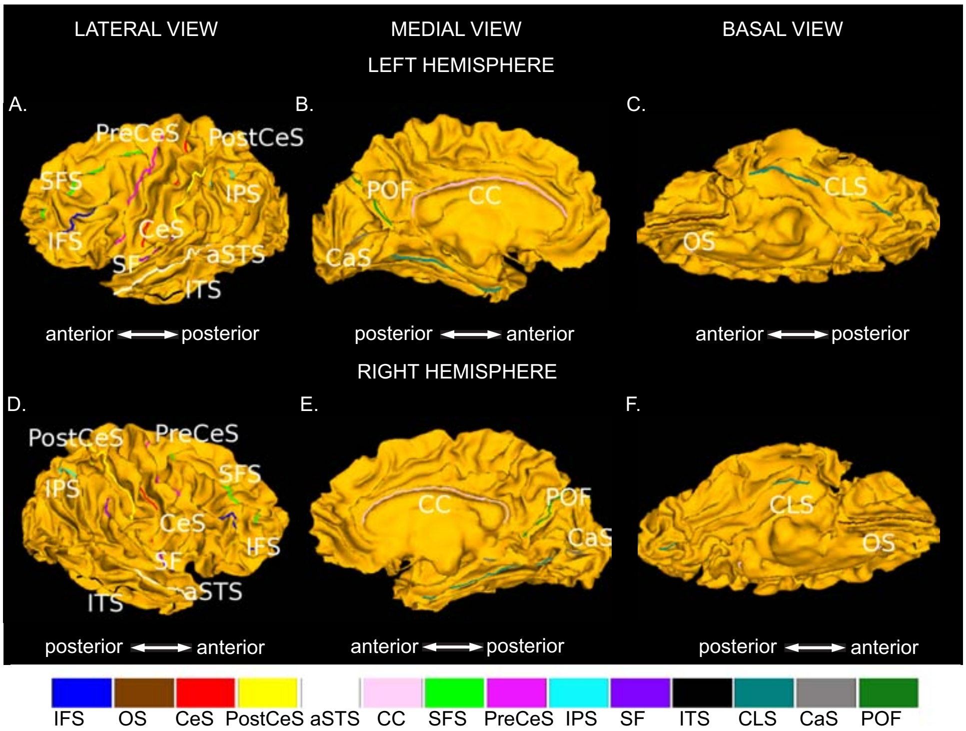

Figure 3.1: Fourteen sulcal curves are illustrated in the lateral (panels A,D), medial (panels B,E), and basal (panels C,F)) views of the left (top row) and right (bottom row) cortical surfaces. Note: on the lateral view: SFS—superior frontal sulcus, IFS—inferior frontal sulcus, CeS—central sulcus, PreCeS—precentral sulcus, PostCeS— postcentral sulcus, IPS—intraparietal sulcus, SF—sylvian fissure, aSTS—anterior segment of the superior temporal sulcus, ITS—inferior temporal sulcus; on the medial view: CC—superior callosal sulcus, POF—parieto-occipital sulcus, CaS—calcarine sulcus; on the basal view: OS— olfactory sulcus, CLS—collateral sulcus.

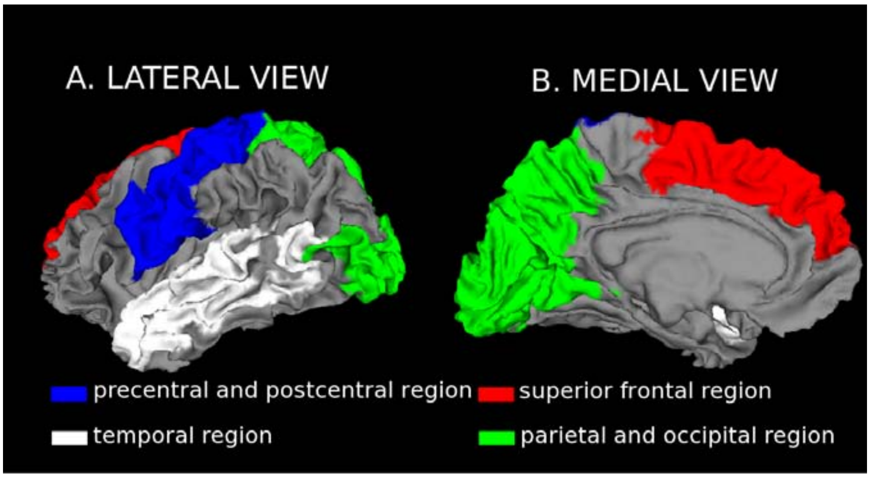

Figure 3.2: Panels (A,B) show the surface with four regions of interest in the lateral and medial views, respectively. The superior frontal region, precentral and postcentral region, temporal region, and parietal and occipital region are respectively colored in red, blue, white, and green.

1. Initial alignment: Apply the MM-LDDMM algorithm for aligning the 14 sulcal curves ($n_c = 14$) and the cortical hemispherical surface ($n_s = 1$) using the MM-LDDMM algorithm.

2. Labeling Process: The parcellation information (Figure 3.2) on the template surface, S_{temp}, is translated to the target cortical surface, S_{targ}, based on the closest distance between the deformed template (from the initial alignment) and the target.

3. ROI alignment: The LDDMM-surface mapping ($n_c = 0$ in Eq. (3.8)) is applied to each ROI. The initial momentum obtained from it is used as the initial assignment in the next step for achieving better alignment in ROIs.

4. Final alignment: Repeat the first step but with the initial assignment of the initial momentum obtained from the third step.

Note that here we proposed one procedure with the above four steps to map two cortical hemispheric surfaces using the MM-LDDMM algorithm. Nevertheless, any other procedures can be applied based on the objective of registration. For instance, in a functional hearing study, the sulcal curves (e.g. the superior and inferior temporal sulci) and the ROI of the auditory cortex may be chosen in the MM-LDDMM algorithm to improve local mapping around the auditory cortex.

3.3 Results

3.3.1 MM-LDDMM Registration Result

Figure 3.3 illustrates two examples of the MM-LDDMM mapping results using this procedure. On each panel, the template surface (in green) estimated from the previous section is superimposed with the target surface (in yellow). Visually, the deformed template surface is well aligned with the target surface both globally and locally, especially, in the superior region and the central sulcal region (see regions pointed by arrows in Figure 3.3.

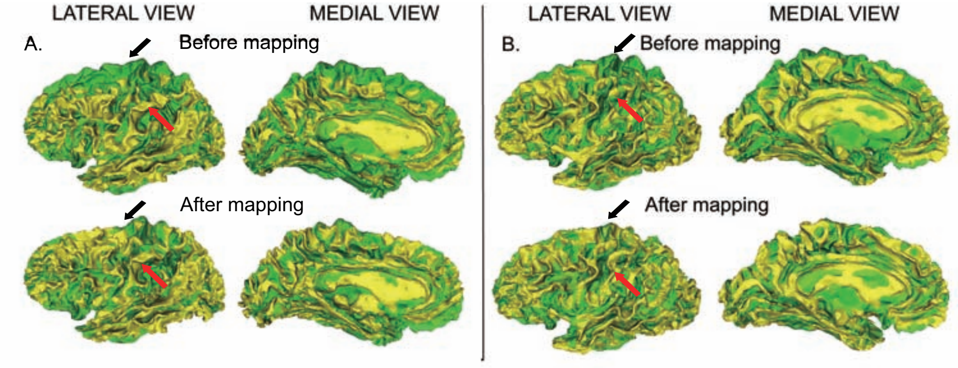

Figure 3.3: Panels (A,B) show two examples of the MM-LDDMM mapping. The template and target surfaces are respectively in green and yellow. The top row of each panel illustrates the target surface superimposed with the template surface before the MM-LDDMM mapping, while the bottom row shows the target surface superimposed with the template surface after the MM-LDDMM mapping. The lateral and medial views of the surface are shown in the left and right columns.

3.3.2 MM-LDDMM Comparisons with the LDDMM-curve Mapping and LDDMM-surface Mapping

To quantitatively measure mapping accuracy, a surface distance graph is defined as the percentage of vertices on surface S_1 having the distance to surface S_2 less than d *mm*. We compared the MM-LDDMM mapping accuracy with those of the LDDMM-curve (7, 105) and LDDMM-surface mappings (104, 106) through the surface distance graph in five ROIs as illustrated in the top row of Figure 3.4. These five ROIs were chosen because they are the major areas in the frontal, temporal, parietal and occipital lobes and are distributed in the lateral and medial views of the cortical surface. Moreover, these five regions are often used to evaluate the accuracy of the cortical registration in literature partly because they can be reliably identified (9, 87).

Twenty subjects (10 young adults with age of 23.9±2.88 and 10 elders with age 73.5±3.27) were randomly selected from the public available dataset of Open Access Series of Imaging Studies (OASIS) (126). Following the data process described in Section 3.2.3, we deformed a template to each of the 20 subjects using the MM-LDDMM mapping with the fourteen sulcal curves and the cortical surface. The template was also deformed to each individual subject via the LDDMM-surface when the initialization of the initial momenta in the ROIs was assigned by the same values as those used in the MM-LDDMM mapping. Finally, the LDDMM-curve mapping with the fourteen sulcal curves was applied to deforming the template to each of the 20 subjects. To make a fair comparison, the key parameters, σ_V and σ_W, were tuned in the LDDMM-curve and LDDMM-surface algorithms and then were directly used in the MM-LDDMM algorithm. To evaluate the mapping accuracy, we manually delineated the five ROIs (see the top row in Figure 3.4) on the cortical hemispherical surface of every subject and then computed the surface distance graphs between each of the twenty subjects and the template deformed by the MM-LDDMM, or the LDDMM-curve mapping, or the LDDMM-surface mapping. The average surface distance graphs among the twenty subjects were shown in the bottom row of Figure 3.4, which suggests that the anatomical variations across subjects were best removed using the MM-LDDMM algorithm in these five regions. The LDDMM-surface mapping gives better results than those of the LDDMM-curve mapping. Moreover, the average surface distance graphs do not show the improvement of the closeness between the template and the twenty subjects in the precentral and superior frontal gyri after the LDDMM-curve mapping partly because the sulcal curves, the coarse representation of the cortical surface, were not defined inside these regions.

3.4 Discussion

The MM-LDDMM algorithm introduced here incorporates the geometry of the cortical surface and its sulcal curves into the large deformation diffeomorphic metric mapping framework for optimizing the alignment of the cortical surface both locally and globally. The MM-LDDMM algorithm takes the anatomical labeling information, including the sulcal curve constraints and initial assignment of the initial momenta in the ROIs, as prior knowledge of the anatomy to ensure that local registration is optimized. In addition, the dense representation of the cortex,

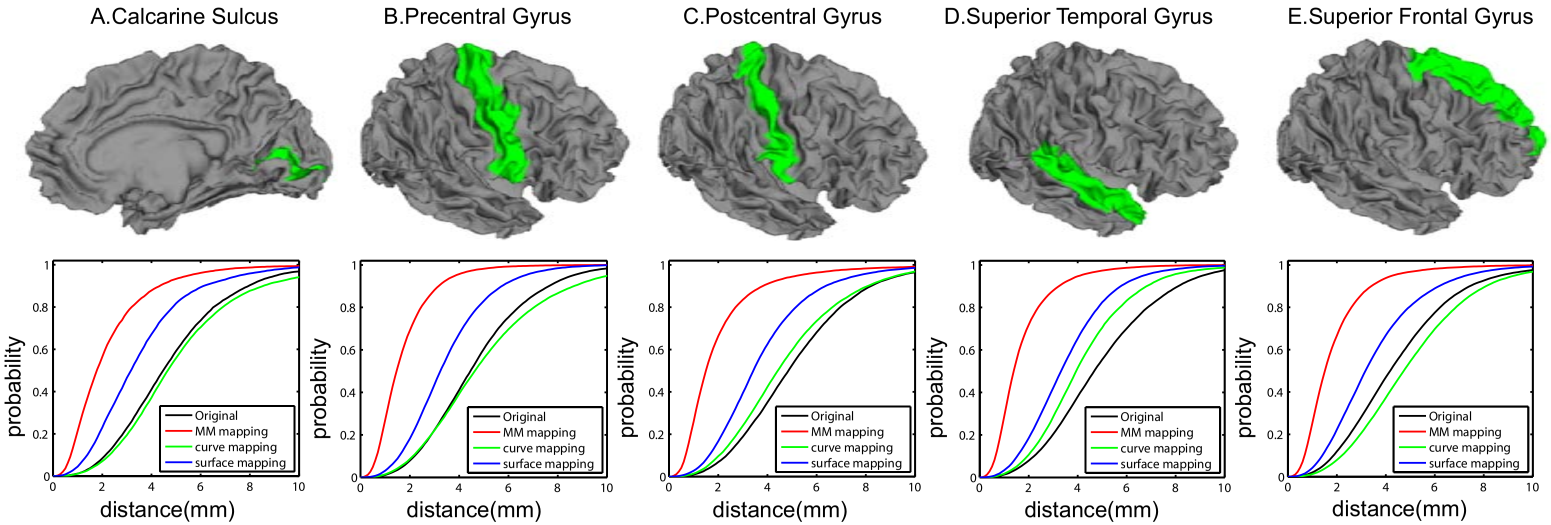

Figure 3.4: The top row shows the lateral or medial view of the template surface with a region of interest (ROI) colored in green. The bottom row shows the average surface distance graphs among 20 subjects for each ROI. Red, blue, green, and black curves respectively correspond to the average surface distance graph after the MM-LDDMM, LDDMM-surface, LDDMM-curve mapping and before any mapping.

the cortical surface, in the MM-LDDMM balances the global and local alignments. This integration of ROI and whole cortical hemispheric surface based registration offers tremendous flexibility in optimizing the alignment of anatomical and functional data across individuals. As shown in previous studies (106, 127, 128, 129), the ROI-based registration in general achieves better alignment. The difficulty with it is to define the anatomical boundary of the ROIs (e.g., the prefrontal cortex, the anterior cingulate) because of large anatomical variabilities across individuals. Using the MM-LDDMM algorithm can avoid the extraction of a specific ROI. Instead, the MM-LDDMM takes reliable sulcal curves inside and around the ROIs to achieve the local mapping accuracy and determines the alignment of anatomical branches with large variabilities across subjects through the geometry of the cortical hemispheric surface. We believe that it is particularly valuable to the group fMRI analysis for improving spatial alignment accuracy and thus increasing statistical power by giving anatomical constraints (e.g. sulcal curves) in the region where functional activations are expected as prior knowledge.

Compared with existing LDDMM algorithms for curves or surfaces (7, 104, 105), the MM-LDDMM algorithm directly takes the constraint of the conservation law of momentum into the optimization and thus guarantees that the optimal trajectory connecting the template and target is geodesic. In contrast, the LDDMM-curve and -surface mapping algorithms (104, 105) seek the optimal time-dependent momenta (or velocity) along the trajectory that theoretically satisfies the conservation law of momentum. However, their numerical solution may not be true. Moreover, the MM-LDDMM algorithm also improves the cortical surface registration when compared with the LDDMM-curve and surface mappings algorithms (104, 105). Nevertheless, the comparison across registration algorithms presented in this chapter is limited to the diffeomorphic mapping algorithms. The comparison of the MM-LDDMM algorithm with the widely used spherical registrations of the cortical surface (2, 5, 107, 111) would be handled in the next chapter with quantitative measures for evaluating mapping accuracy, which will be valuable to neuroimaging community.

4

MM-LDDMM Validation

In the previous chapter, we developed a cortical surface registration method, MM-LDDMM, and showed that it could improve the surface registration with comparison to the LDDMM-curve and surface mappings algorithms (104, 105). While the comparison was limited to the diffeomorphic mapping algorithms, the performance of this method over other widely used spherical registrations of the cortical surface (2, 5, 107, 111) needs to be addressed. In this chapter, we would compare the MM-LDDMM with both previous LDDMM registrations and other spherical registrations with quantitative measures for evaluating mapping accuracy for local and global features, which will be valuable guidance to neuroimaging community for choosing mapping algorithms.

4.1 Introduction

Cortical surface model is widely used in anatomical and functional studies in magnetic resonance imaging (MRI) as it can well preserve the complex sulco-gyral folding pattern of the human cortex (86, 107, 108, 109, 110). Researchers have recently focused on developing techniques for cortical parcellation, cortical morphological and functional studies using the cortical surface model (9, 78, 130). In particular, registration for the cortical surface has received great attention in both anatomical and functional studies in magnetic resonance imaging (MRI) (86, 108, 109, 110, 131). It has been widely applied in brain morphometric studies not only for exploring abnormalities in the cortical morphology and functions associated with disease but also for providing the locations (e.g. (113, 132, 133)). Moreover, functional studies have shown that cortical surface mappings have superior power in detecting functional activations as compared to automated Talairach registration (2) and affine volume-based registration approaches (9).

Since the cortex is highly folded, its surface representation has been suggested to facilitate the visualization and analysis of functional data by preserving its important geometrical and topological relationships. One well-known representation is the sphere. Various methods have been proposed to inflate the cortical surface and then project it onto a unit sphere, such as CARET (87), FreeSurfer (108), conformal mappings (134, 135). Thus, a majority of early cortical surface mapping approaches were developed in the spherical coordinates where landmarks (e.g. points or gyral/sulcal curves) or cortical folding patterns were driving forces to align one cortical sphere to the other (87, 92, 107, 108, 111, 112). Among them, curve-based CARET and folding-pattern-based FreeSurfer cortical mapping algorithms have been widely used partly because they are publicly available and provide reasonable cortical alignments. Nevertheless, the curve or folding-pattern-based spherical mappings require the spherical parameterization of the cortical surface in which adjacent gyri with distinct functions are well separated. This surface parameterization process introduces distance, area, and angular distortions that potentially affect the quality of the surface alignment. To avoid such an issue, one would expect to directly align the cortical surfaces in their own coordinates. In 2005, Vaillant and Glaunès (98) first introduced a vector-valued measure acting on vector fields as geometric representation of surfaces in their own space and then imposed a Hilbert space structure on it, whose norm was used to quantify the geometric similarity between two surfaces in their own coordinates. Since then, the vector-valued measure has been incorporated as a matching functional in the variational problems of large deformation diffeomorphic metric surface mapping (LDDMM) (98, 99). Following this work, several LDDMM algorithms have been developed to map gyral/sulcal curves (LDDMM-curve) (8, 88) and simultaneously align cortical surfaces and gyral/sulcal curves (multi-manifold LDDMM, MM-LDDMM) (136). Several studies have shown the robustness of the LDDMM algorithms in registering cortical surfaces using curves (88) or both curves and surfaces (136).

While many cortical mapping approaches are available, anatomical and functional studies have suggested that different mapping algorithms can influence statistical outcomes in group analysis (93, 137). Thus, it is important to know the performance of each mapping algorithm, especially in regions of interests (ROIs), to properly interpret image findings. To our knowledge, no study has directly compared the LDDMM approaches with spherical registration methods, such as those in CARET and FreeSurfer, to address their mapping accuracies. In this chapter, we aim to quantitatively compare these cortical surface mapping algorithms, including LDDMM-curve, LDDMM-surface, MM-LDDMM, CARET, and FreeSurfer, in terms of registration accuracy for local (gyral/sulcal curves and sulcal regions) and global (folding pattern) cortical features. In addition, we conducted a simulation experiment to evaluate mapping error distribution over the cortical surface and localize regions with large mapping errors for each mapping algorithm, which potentially provides guidance for the choice of mapping algorithm in ROI-specific imaging studies.

4.2 Methods

4.2.1 Subjects and Image Acquisition

Forty subjects comprising of ten young adults (5 males and 5 females, age: 23.4±2.55 years), ten middle-aged adults (5 males and 5 females, age: 49.3±1.89 years), ten elderly (5 males and 5 females, age: 73.9±2.02 years), and ten patients with Alzheimer's disease (5 males and 5 females, age: 76.4±2.55 years) were randomly selected from the OASIS database (138). An average atlas was not used in this study because mapping accuracy may be biased to the mapping algorithm that was applied to generate the average atlas. Thus, a single-subject template was constructed using an MRI scan collected from a healthy subject (female, age: 54 years). This subject was chosen because her age and total brain volume were at the average values of the 40 subjects in this study.

Magnetic resonance (MR) scans for the whole brain were acquired using the Siemens Magnetom Vision 1.5T imaging system using Magnetization Prepared Rapid Gradient Recalled Echo (MPRAGE) sequence (TR = 9.7 ms, TE = 4 ms, flip angle = 10°, inversion time (TI) = 20 ms, delay time (TD) = 200 ms, 256 × 256 (1 × 1 mm) in-plane resolution, one hundred twenty-eight 1.25-mm slices without gaps). Three or four T1- weighted MPRAGE scans were collected for each subject. Head movement was minimized by cushioning and a thermoplastic face mask. All MR images used in this study are accessible online (`www.oasis-brains.org`) (138).

4.2.2 Cortical Surface Generation

The three or four MP-RAGE data per subject were averaged offline (with correction for head movement) to increase the contrast to noise ratio and were interpolated into isotropic voxels with resolution of 1mm × 1mm × 1mm. FreeSurfer was used to label each voxel as cerebrospinal fluid (CSF), gray matter (GM), and white mater (WM) using a Markov-Random field model (139). An inner surface at the boundary of GM and WM was constructed and then propagated to the boundary of GM and CSF to form an outer surface via a flow with the force based on the image labeling and gradient such that the topologies of the outer and inner surfaces were preserved (4). The fiducial surface, the center of the inner and outer surfaces, was then smoothed by changing the location of each vertex toward the barycenter of its first neighbors to reduce noise features and small geometric changes of shapes (140). For the rest of the chapter, this smoothed fiducial surface was considered as geometric representation of the cortex and used as input surface for LDDMM, CARET, and FreeSurfer cortical surface mappings. Examples of the cortical surface are illustrated in the first column of Figure 4.1.

4.2.3 Cortical Surface Mapping Algorithms

4.2.3.1 LDDMM

Two cortical surfaces may be mapped onto each other by treating the 2-dimensional manifolds of the cortical surfaces as 1-dimensional features (curves), or 2-dimensional structure of the manifold as a whole, or combination of 1- and 2-dimensional features (curves and surface). Compared to 2-dimensional surface matching, an advantage of 1-dimensional curve mapping is that the amount of computation is reduced. Also, the selection of curves can be guided by previous knowledge derived from postmortem studies. In the setting of LDDMM, we developed mapping algorithms that utilize three different anatomical manifolds; i.e. curves (8, 88), surfaces (98, 99), and integration of curves and surfaces (136). All of these mapping algorithms provide diffeomorphic maps (i.e., one-to-one, reversible smooth transformations that preserve topology) that allow deforming one cortical surface to a template in its own folded coordinates. The use of LDDMM for mapping the cortical surfaces requires studying them in a metric space, provides a diffeomorphic transformation, and defines a metric distance that can be used to quantify the similarity between two shapes. We assume that shape objects can be generated one from the other via a flow of diffeomorphisms, solutions of ordinary differential equation $\dot{\phi}_t = v_t(\phi_t), t \in [0, 1]$ with $\phi_0 = \mathrm{id}$, identity map, and associated velocity fields v_t. For a pair of objects I_{temp} and I_{targ}, a diffeomorphic map ϕ transforms one to the other $\phi_1 \cdot I_{temp} = I_{targ}$ at time $t = 1$. We defined a variational problem to find optimal transformation, $\phi_t, t \in [0, 1]$, in

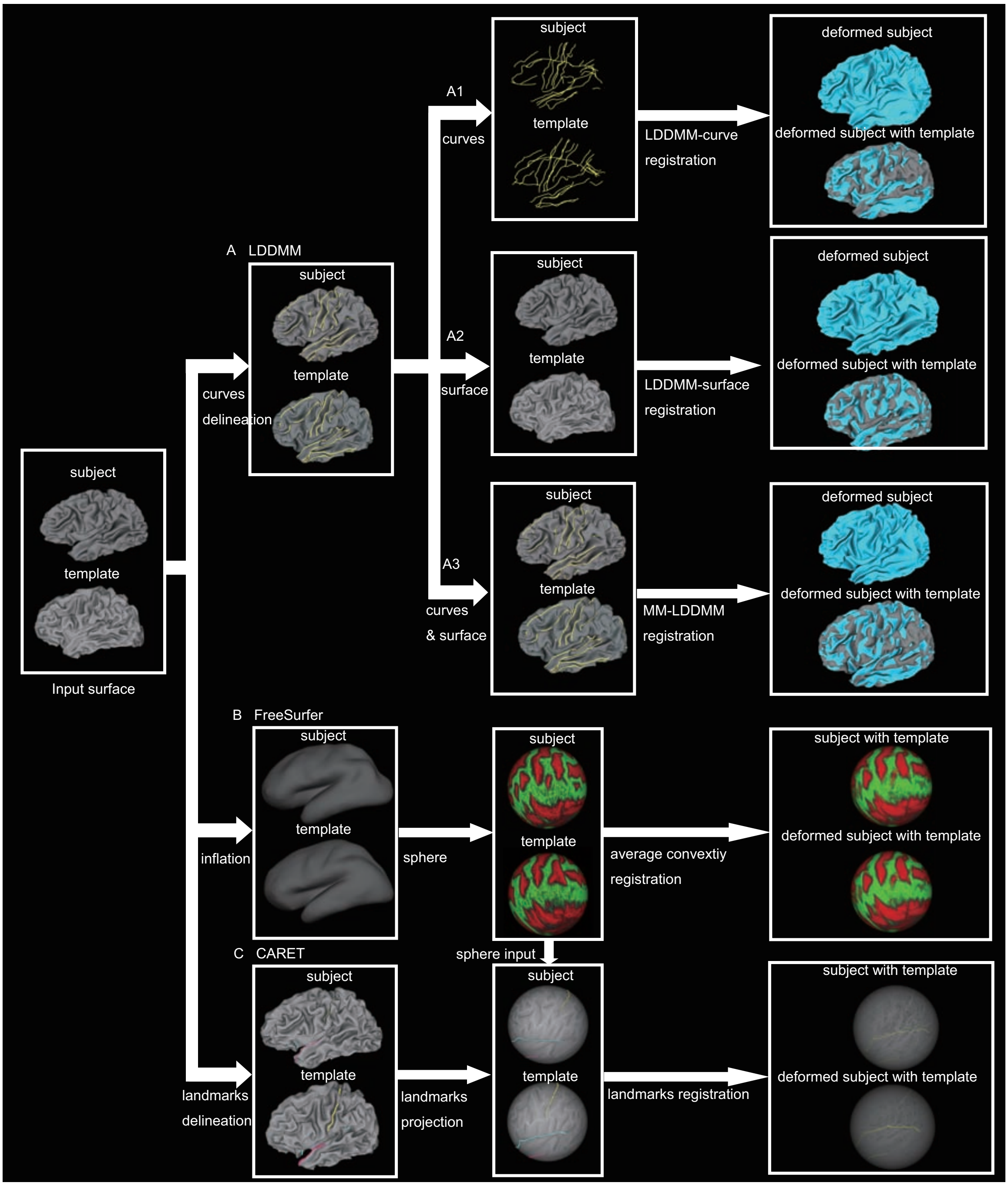

Figure 4.1: Schematic of LDDMM, FreeSurfer, CARET cortical mapping processing pipelines.

the form of

$$J(v_t) = \inf_{v_t:\dot{\phi}_t = v_t(\phi_t), \phi_0 = \text{id}} \int_0^1 \|v_t\|_V^2 dt + \beta E(\phi_1 \cdot I_{temp}, I_{targ}), \tag{4.1}$$

where the first term quantifies the metric distance between the shapes, the length of the geodesic curves $\phi_t \cdot I_{temp}, t \in [0, 1]$ through the shape space generated from connecting I_{temp} to I_{targ} in a Hilbert space, V , of smooth vector fields with norm $\| \cdot \|_V$. V ensures that the solutions are diffeomorphisms. β is the trade-off parameter. $E(\phi_1 \cdot I_{temp}, I_{targ})$ quantifies the closeness between the deformed object $\phi_1 \cdot I_{temp}$ and object I_{targ}. We adapted this variational problem to different objects, such as curves (8, 88), surfaces (98, 99), and integration of curves and surfaces (136). For the purpose of registering two cortical surfaces, we briefly reviewed how to define $E(\phi_1 \cdot I_{temp}, I_{targ})$ for objects of curves, surfaces, and integration of curves and surfaces.

LDDMM-curve: Since a curve is a geometric object, it cannot be uniquely reconstructed based on the locations of a set of points. We consider a curve embedded in R^3 as a one-dimensional manifold in the sense that the local region of every point on the curve is equivalent to a line which can be uniquely defined by this point and the tangent vector at this location. Thus, we, represent our mapping object, I, as $I = \gamma^i, i = 1, 2, ...n_c$, where $\{\gamma^i\}_1^{n_c}$ is a set of gyral and sulcal curves on the surface associated with a series of points and their tangent vectors. n_c is the total number of paired curves. We defined $E(\phi_1 \cdot I_{temp}, I_{targ})$ in Eq. (4.1) as

$$E(\phi_1 \cdot I_{temp}, I_{targ}) = \sum_{i=1}^{n_c} E_{\gamma_i}(\phi_1 \cdot \gamma^i_{temp}, \gamma^i_{targ}) \ ,$$

where $\phi_1 \cdot \gamma^i_{temp}$ is the deformed template curve while γ^i_{targ} is the target curve. $E_{\gamma_i}(\phi_1 \cdot \gamma^i_{temp}, \gamma^i_{targ})$ quantifies the closeness of the i^{th} paired curves $\phi_1 \cdot \gamma^i_{temp}$ and γ^i_{targ} by computing the similarity of the tangent vectors of these two curves.

As illustrated in Figure 4.2, fourteen sulcal and twelve gyral curves were semi-automatically delineated for each subject and subsequently used for the LDDMM-curve mapping in this study. These curves were chosen because they are consistently present and readily identifiable on the cortex. The anatomical definitions of these curves are described elsewhere (136) (`www.bioeng.nus.edu.sg/cfa/mapping/curveprotocol.html`). Briefly, the initial starting and ending points of each curve were manually defined on the fiducial surface and the gyral (or sulcal) curve between them was automatically generated using dynamic programming by maximizing (or minimizing) the curvature information along the curve (141). In this study, we deformed the fiducial surface of each individual subject to the template surface by interpolating the deformation field obtained from the LDDMM-curve algorithm via the diffeomorphic flow.

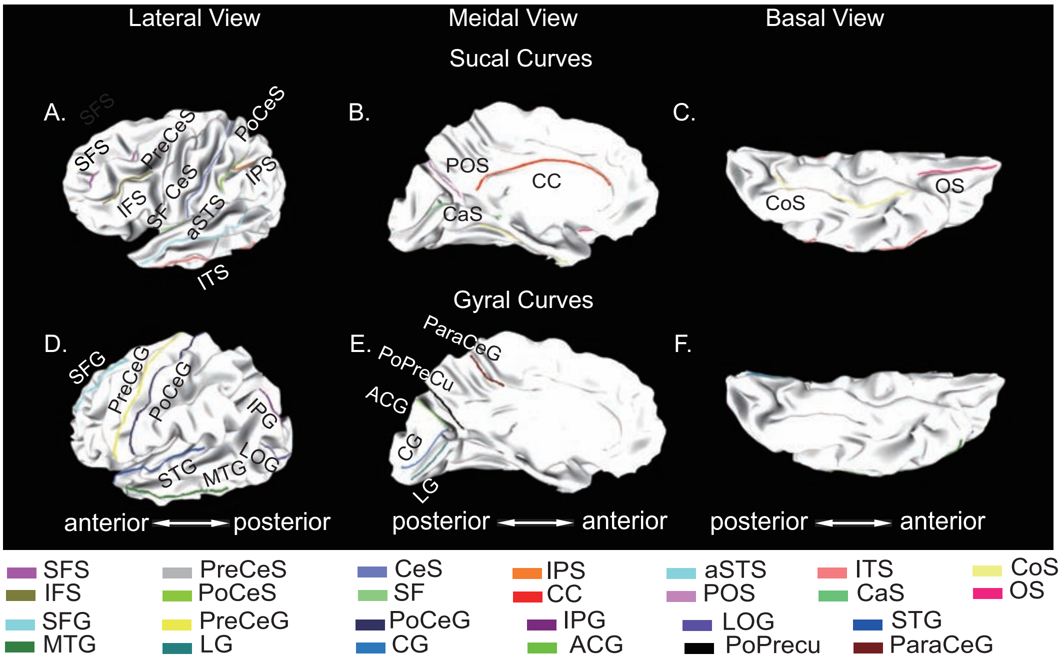

Figure 4.2: Fourteen sulcal curves and twelve gyral curves are illustrated in the lateral (panels A, D), medial (panels B, E), and basal (panels C, F) views of the template surface. The top and bottom rows show sulcal and gyral curves respectively.
Note: Panel (A): SFS(1)-superior frontal sulcus, IFS(2)-inferior frontal sulcus, PreCeS(3)-precentral sulcus, CeS(23)-central sulcus, PoCeS(4)- postcentral sulcus, IPS(5)-intraparietal sulcus, SF(6)-sylvian fissure, aSTS(7)-anterior segment of the superior temporal sulcus, ITS(8)-inferior temporal sulcus; Panel (B): CC(24)-superior callosal sulcus, POS(9)-parieto-occipital sulcus, CaS(25)-calcarine sulcus; Panel (C): OS(10)- olfactory sulcus, CoS(11)-collateral sulcus; Panel (D): PreCeG(12)-precentral gyrus, PoCeG(13)- postcentral gyrus, STG(26)-superior temporal gyrus, MTG(14)-middle temporal gyrus, IPG(15)-intraparietal gyrus, SFG(20)-superior frontal gyrus, LOG(22)-lateral occipital gyrus; Panel (E): LG(16)-lingual gyrus; CG(17)-cuneus gyurs; ACG(18)-anterior border of the cuneus gyrus, PoPrecu(19)- posterior border of the precuneus, ParaCeG(21)-paracentral gyrus.

LDDMM-surface: We assume the cortical surface embedded in R^3 to be a two-dimensional manifold in the sense that the neighborhood of every point on the surface is equivalent to a two-dimensional plane in Euclidean space. Such a plane can be uniquely defined by a point and a vector originated at this point and normal to the plane. Next, we defined $E(\phi_1 \cdot I_{temp}, I_{targ})$ for registering surfaces in the LDDMM setting based on their position and normal vectors, in which $E(\phi_1 \cdot I_{temp}, I_{targ})$ in Eq. (4.1), is given in the form of

$$E(\phi_1 \cdot I_{temp}, I_{targ}) = E_S(\phi_1 \cdot S_{temp}, S_{targ}) \ ,$$

where $E_S(\phi_1 \cdot S_{temp}, S_{targ})$ quantifies the closeness of the deformed template and target surfaces by computing the similarity of their normal vectors. In our study, the LDDMM-surface algorithm was used to deform the fiducial surface of each individual subject to the template surface.

MM-LDDMM: We assume the cortical surface embedded in R^3 to be a multi-manifold, integration of one- and two-dimensional manifolds (curves and surfaces). Multi-manifold large deformation diffeomorphic metric mapping (MM-LDDMM) (136) was designed to integrate the gyral/sulcal curves and the fiducial surface together and thus, allowed carrying the cortical surface and its gyral/sulcal curves simultaneously from one to the other through a flow of diffeomorphisms. MM-LDDMM incorporates anatomical priors through gyral and sulcal curves to constrain regional alignment, and the geometry of the fiducial surface to constrain regional and global alignment. Thus, we represented our mapping object, I, as $I = S, \gamma^i, i = 1, 2, ...n_c$, where S is the fiducial surface associated with a set of vertices and their normal vectors. $\{\gamma^i\}_1^{n_c}$ is a set of gyral and sulcal curves on the surface associated with a series of points and their tangent vectors. In the MM-LDDMM setting, we defined $E(\phi_1 \cdot I_{temp}, I_{targ})$ for aligning the fiducial surface as well as sulcal and gyral curves in the form of

$$\beta E(\phi_1 \cdot I_{temp}, I_{targ}) = \beta_S E_S(\phi_1 \cdot S_{temp}, S_{targ}) + \sum_{i=1}^{n_c} \beta_{\gamma_i} E_{\gamma_i}(\phi_1 \cdot \gamma^i_{temp}, \gamma^i_{targ}) \ ,$$

where $E_{\gamma_i}(\phi_1 \cdot \gamma^i_{temp}, \gamma^i_{targ})$ and $E_S(\phi_1 \cdot S_{temp}, S_{targ})$ were described previously. β_S and β_{γ_i} are the trade-off parameters for surface closeness and curve closeness respectively. In our study, the fiducial surface of each individual subject was deformed to the template surface using the MM-LDDMM algorithm where the fiducial surface in the LDDMM-surface algorithm as well as the fourteen sulcal and twelve gyral curves in the LDDMM-curve algorithm were considered as mapping objects.

4.2.3.2 FreeSurfer Cortical Mapping

Unlike LDDMM approaches, the cortical mapping algorithm in FreeSurfer requires spherical parameterization of the cortical surface and then aligns cortical patterns (e.g. cortical convexity, cortical curvature) in the spherical coordinates. For these, Fischl and colleagues proposed several variational problems for cortical inflation, and spherical mapping (2, 108). As illustrated in Figure 4.1(B), the folded cortical surface was first inflated to remove its intrinsic folding pattern while minimizing metric distortion and a spring force that constrained the smoothness of the surface. Thus, the cortical inflation provided a representation of the cortical hemisphere that retained much of the shape and metric properties of the original surface, yet allowing for better visualization of functional activity occurring within sulci. The inflated surface was then projected onto a unit sphere by moving each vertex in the tessellation of the inflated surface to the closest point on the sphere based on surface normal vector. The metric distortion introduced in this projection procedure was further minimized. Once the spherical representation was established, standard spherical coordinate systems (e.g., longitude and latitude) were used to index a point on the folded cortical surface for a given subject. Finally, alignment of the cortical surface with a template in the spherical coordinates was implemented by minimizing the mean squared difference between the cortical convexities (108) of the individual and the template. The spherical mapping in FreeSurfer (v4.0.2) was applied in this study.

4.2.3.3 CARET Cortical Mapping

The cortical surface mapping in CARET is a landmark-based spherical registration approach (87). To apply it, we first manually delineated six curves, including the central sulcus (CeS), sylvian fissure (SF), anterior half of the superior temporal gyrus (aSTG), calcarine sulcus (CaS), the medial wall dorsal segment, and the medial wall ventral segment, on the folded cortical surface of each individual subject based on the protocol given on website (`brainvis.wustl.edu/help/landmarks_core6/landmarks_core6.html`). The curves were then projected to the spherical coordinates of the cortical surfaces. Note that the spherical representation of each individual cortical surface was generated using the cortical inflation and spherical projection approaches in FreeSurfer in order to reduce potential errors in evaluation measurements due to different cortical spherical parameterizations. Examples of the curve representation on the sphere are illustrated in Figure 4.1(C). Finally, the subject sphere was deformed to the template sphere by forcing the subject landmarks into alignment with the template landmarks and also minimizing local shape distortion of the subject sphere. This landmark-based spherical mapping in CARET (v5.61) was applied in this study.

4.2.4 Quantitative Measures of Cortical Mapping Accuracy

4.2.4.1 Curve Variation Error

We introduced Hausdorff distance to evaluate anatomical variation based on the local features of the sulcal and gyral curves. For each subject, the fourteen sulcal and twelve gyral curves (used in the LDDMM mappings) and six landmarks (used in the CARET mapping) were first transformed to the folded template surface coordinates based on the transformation found using the LDDMM, FreeSurfer, or CARET cortical mapping algorithms. We denoted a specific sulcal/gyral curve of subjects, i and j, in the template coordinates as γ^i and γ^j . The Hausdorff distance (142) was then computed for these paired curves as

$$d(\gamma^i, \gamma^j) = 0.5\frac{1}{N_1}\sum_{x\in\gamma^i}\min_{y\in\gamma^j}|x-y| + 0.5\frac{1}{N_2}\sum_{y\in\gamma^j}\min_{x\in\gamma^i}|x-y| \ ,$$

where N_1 and N_2 were the number of points on γ^i and γ^j, respectively. $|x-y|$ denoted the Euclidean distance between points x and y . The first term in the above equation was the average minimum distance of each point in curve γ^i to a point in curve γ^j, and the second term is the average minimum distance of each point in γ^j to a point in γ^i.

To evaluate the anatomical variation of a specific sulcal/gyral curve among subjects, which cannot be characterized by the deformation found using the cortical mapping, we further calculated a curve variation error (143) as

$$VAR = \frac{1}{2J(J-1)}\sum_{i=1}^{J}\sum_{j=1}^{J}\left[d(\gamma^i, \gamma^j)\right]^2 ,$$

where J is the number of subjects in the study. Lower value indicates better alignment for this curve.

4.2.4.2 Surface Alignment Consistency and Overlap Ratio of Sulcal Regions

Surface alignment consistency (SAC) was initially introduced by (87) for quantifying the anatomical variability of a sulcal region among a group of subjects that can be characterized by the cortical mapping algorithm. Assume J to be the number of subjects involved in the SAC study whose cortical surfaces were transformed to the folded template surface coordinates using the transformation found through one of the cortical mapping algorithms. We considered the sulcal region on the template surface which consisted of the vertices of the sulcal region transformed from all the J subjects as a reference and denoted its vertex location as x . For every x , we first computed the probability map, $p(x)$, to represent the chance of location x being this sulcal region where $p(x)$ can be approximated as $\frac{i-1}{J-1}, i = 1, 2, ...J$. We then integrated $p(x)$, over the sulcal region and normalized it by this sulcal area of the template surface. In the discrete case, where the cortical surface was a triangulated mesh, we can define SAC as

$$SAC = \frac{1}{N} \sum_{i=1}^{J} \frac{i-1}{J-1} n_i$$

where N is the total number of vertices in this sulcal region on the template surface and n_i is the number of vertices in this sulcal region with probability of $p(x) = \frac{i-1}{J-1}$. SAC is ranged from 0 to 1, i.e., the higher the value, the better the sulcal alignment.

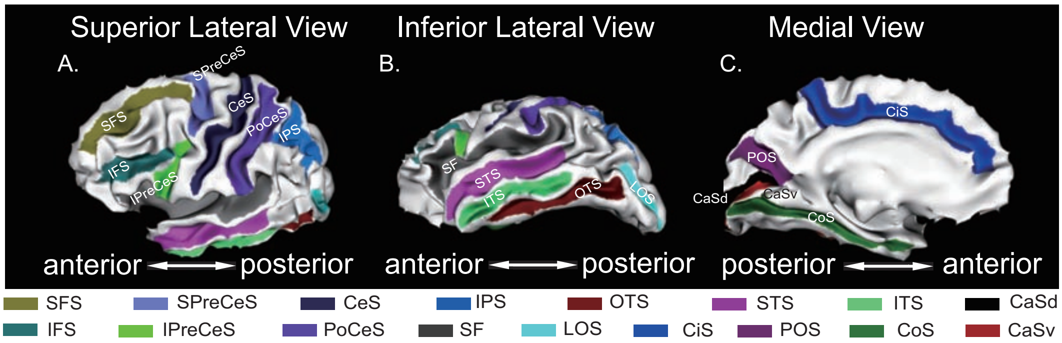

Figure 4.3: Seventeen sulcal regions are shown in the superior (A), inferior (B), and medial (C) views of one subject's surface. The names of the sulcal regions are listed in Table 4.1.

In our study, one rater (DYLP) manually delineated seventeen sulcal regions for each of 40 subjects (see detailed protocol in (87) and on the website (`www.bioeng.nus.edu.sg/cfa/mapping/sulcalprotocol.html`). These sulcal regions were chosen because they are distributed broadly over the cortical surface as illustrated in Figure 4.3. These sulcal regions were also used for quantifying cortical mapping accuracy in previous studies (87). We computed SAC for each of these seventeen sulcal regions. To test the intra-reliability of the manual delineation of each region within a subject for ensuring that SAC results were not influenced by the delineation error, the seventeen sulcal regions of five subjects were delineated twice (rater: DYLP). The second delineation was done three weeks after the first delineation. We computed an overlap ratio for each sulcal region as

$$R = \frac{2N_{S_1 \cap S_2}}{N_{S_1} + N_{S_2}}$$

where $N_{S_1 \cap S_2}$ represents the number of vertices having being labeled as the sulcal region in both manual delineations, while $N_{S_i}, i = 1, 2$ denotes the number of vertices having being labeled as the sulcal region in the i^{th} delineation. Furthermore, the overlap ratio was also computed to quantify the consistency of the sulcal region alignment between individual subjects and the template, where S_1 denoted the sulcal region of the template and S_2 represented the sulcal region of a subject deformed to the template coordinates. While the aim of delineating the sulcal regions on the surfaces is to test the mapping accuracy of different mapping methods, this SAC measure would be less influenced as long as the regions are consistently delineated by one rater. On the other hand, inter-rater reliability analysis is to guarantee the sulcal regions are delineated less subjectively, which is not the aim of the delineation. So the inter-rater reliability is not analyzed in this study.

4.2.4.3 Curvature Correlation

The purpose of the cortical surface mapping is to deform one surface to the other such that local and global shape characteristics of the two surfaces are similar. To test it, we computed curvature correlation of the subject's deformed cortical surface and the template surface. The mean curvature of the subject's deformed surface in the template coordinates was calculated by transferring the mean curvature of the subject folded cortical surface to the template based on the transformation found using one of the cortical mapping algorithms. When $\rho = 1$, the global shape pattern of the subject's deformed surface well matches with that of the template surface. The lower value of ρ signals worse registration with a theoretical minimum of $\rho = 0$.

4.2.4.4 Local and Global Deformation Errors

To directly quantify deformation fields that each mapping algorithm characterizes, we conducted a simulation experiment in which folded cortical surfaces were generated from a template by moving its vertices by known deformation. To do this, we modeled deformation, $U(x)$, as random fields in the template coordinates, which can be generated using equation

$$U(x) = \overrightarrow{U_0} + \sum_{i=1}^{n} U_i \Psi_i(x) \overrightarrow{N}(x) \,, \tag{4.2}$$

where $\overrightarrow{U_0}$ is a random vector with three elements. $\overrightarrow{N}(x)$ is the normal vector at location x on the template surface. $\Psi_i(x)$ is the i^{th} Laplace-Beltrami basis function defined in the template surface (144). Figure 4.4 shows examples of the Laplace-Beltrami basis functions on the template surface in the lateral and medial views. The regions with positive values are colored red, while the ones with negative values are in blue. $\{U_i\}_{i=1}^n$ are random variables associated with $\Psi_i(x)$. In our experiment, we used the first ten Laplace-Beltrami basis functions and applied this model for constructing ten cortical surfaces from the template where $\{U_i\}_{i=1}^n$ and $\overrightarrow{U_0}$ were randomly generated based on Gaussian distribution. Specifically, $\{U_i\}_{i=1}^n$ and $\overrightarrow{U_0}$ were randomly chosen such that each individual constructed surface had average deformation displacement across the entire surface about 1-2 *mm*. Nevertheless, the maximum deformation displacement across the entire surface can be as large as 5.20 *mm*.

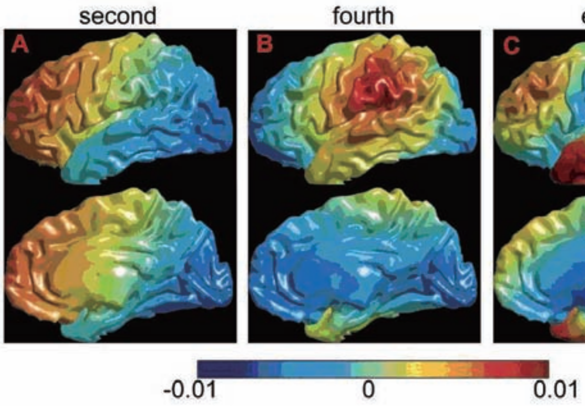

Figure 4.4: Panels (A-C) illustrate the second, fourth, eighth Laplace-Beltrami basis functions respectively on the template surface. The top and bottom rows of each panel show the template surface in the lateral and medial views respectively.

We employed the MM-LDDMM, FreeSurfer, and CARET cortical mapping algorithms to align the ten individual surfaces to the template. The deformation at a specific location of the cortical surface that cannot be carried out by the mapping algorithms was quantified by the absolute value of the difference between the true deformation obtained in Eq. (4.2) and deformation fields found through each of the mapping algorithms. We termed it as local deformation error in this thesis. The mean value of the local deformation error over the template surface was also computed to give an overall evaluation of the deformation errors, referred to as global deformation error. Since the template was the one used to generate the simulated surfaces, these local and global deformation errors only quantified the amount of deformation that each mapping algorithm can characterize but not the anatomical difference between the template and simulated dataset (e.g. missing gyri or sulci).

4.3 Results

We evaluated the accuracy of the LDDMM, FreeSurfer, and CARET cortical mapping algorithms using cortical surfaces of the 40 subjects in Sections (4.3.1 to 4.3.3) and ten simulated cortical surfaces in Section 4.3.4.

4.3.1 Curve Variation Errors

We computed the variation errors of the twenty six curves used in the LDDMM mapping (see Figure 4.2) and the six curves used in the CARET mapping (see Figure 4.1(C))among the 40 subjects for each of the mapping algorithms. Figure 4.5 illustrates these errors to indicate the gyral/sulcal variability that cannot be characterized by the deformation found using the LDDMM, FreeSurfer, and CARET mapping algorithms.

As illustrated in Figure 4.5(A), the variation errors of the twenty six curves suggested that the LDDMM-curve mapping algorithm provided the lowest curve variation errors for most of the twenty six curves in comparison to the other mapping algorithms. Compared with FreeSurfer and LDDMM-surface mapping algorithms, the CARET cortical mapping showed relatively lower variation errors of the curves involved in the mapping process, including the central sulcus (index 23), calcarine sulcus (index 24), superior temporal gyrus (index 25), and dorsal segment in the medial wall (close to callosum, index 26), as well as their adjacent curves, including precentral (12) and postcentral (13) gyri, lingual (16) and cuneus (17) gyri. However, the CARET mapping showed larger or comparable variation errors for these curves when compared with the LDDMM-curve mapping. Furthermore, the anatomical variation of the other curves cannot be well carried out using the CARET mapping deformation. In addition, the MM-LDDMM algorithm balanced the geometry of the curves and surfaces when aligning two cortical surfaces. Thus, it provided better curve alignment than the LDDMM-surface, FreeSurfer, and CARET algorithms but had comparable results with the LDDMM-curve algorithm. Overall, the variation errors averaged over all twenty six curves were 5.77 (±3.08) for LDDMM-curve, 6.36 (±3.31) for MM-LDDMM, 14.38 (±6.77) for FreeSurfer, 14.41 (±7.17) for LDDMM-surface, 14.89 (±9.19) for CARET. Figure 4.5(B) illustrates the variation errors of the six curves defined for the CARET mapping. Our results suggested that CARET provided the lowest variation errors of these six curves when compared with the other mapping algorithms. Notice that among these six curves, four curves (central sulcus, calcarine sulcus, superior temporal gyrus, and superior callosal sulcus) were defined similarly to those used for

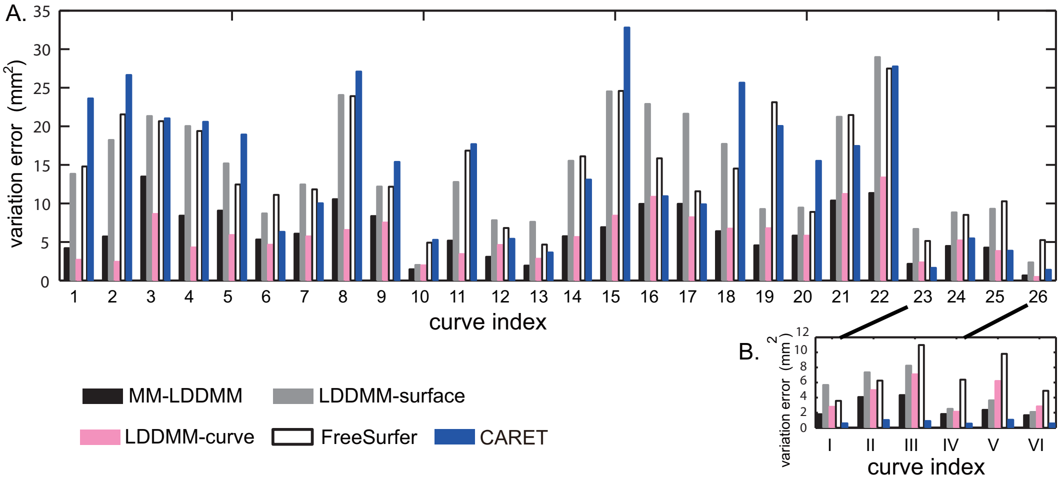

Figure 4.5: Panel (A) shows the variation errors of the twenty six curves defined for the LDDMM mapping. The full name and index of each curve are given in Figure 4.2. Panel (B) illustrates the variation errors of the six curves defined for the CARET mapping, including the central sulcus (I), calcarine sulcus (II), anterior segment of the superior temporal gyrus (III), the medial dorsal segment (IV), and the medial wall ventral segment (V), and sylvian fissure (VI). The first four curves were defined similar to those indexed as 23-26 in panel (A). Black, gray, pink, white, and blue bars are the curve variation errors among 40 subjects that cannot be characterized by MM-LDDMM, LDDMM-surface, LDDMM-curve, FreeSurfer, and CARET cortical mapping algorithms respectively.

the LDDMM mapping. The variation errors of these four curves from the LDDMM, CARET, and FreeSurfer mappings were comparable with those shown in Figure 4.5(A) (curve indices: 23-26). Overall, the variation errors averaged over these six curves were 0.78 (±0.24) for CARET, 2.67 (±1.21) for MM-LDDMM, 4.33 (±2.05) for LDDMM-curve, 4.92 (±2.57) for LDDMM-surface, and 6.98 (±2.86) for FreeSurfer.

4.3.2 Overlap Ratio and Surface Alignment Consistency (SAC)

The second column in Table 4.1 lists the overlap ratio of two manual delineations of each sulcal region averaged over five subjects. The lowest value of the average overlap ratio was 0.90 for the inferior frontal sulcus while the highest value was 0.96 for the Sylvian fissure. The average overlap ratio is above 0.90 for all seventeen sulcal regions. The third to seventh columns in Table 4.1 list the overlap ratio of each sulcal region averaged over the forty subjects for the MM-LDDMM, LDDMM-surface, LDDMM-curve, FreeSurfer, and CARET mappings, respectively. Regardless of the mapping algorithms, both the central sulcal region and Sylvian fissure had higher overlap ratios (ranged from 0.56 to 0.64) than other sulcal regions, while the lateral occipital and inferior frontal sulcal regions had lower overlap ratios (ranged from 0.21 to 0.38) than others. This was consistent with the intra-reliability of the manual delineation, which thus explained that the mapping accuracy was dependent on the variability of anatomical regions across subjects. Overall, the average overlap ratios across the 17 sulcal regions were 0.49(±0.08) for MM-LDDMM, 0.45(±0.09) for LDDMM-surface, 0.45(±0.07) for LDDMM-curve, 0.47(±0.09) for FreeSurfer, and 0.45(±0.11) for CARET. One sample Student's t-tests revealed that the average overlap ratio was significantly decreased in the order of the MM-LDDMM, FreeSurfer, and CARET mapping algorithms (MM-LDDMM vs FreeSurfer: $p=0.0084$; FreeSurfer vs CARET: $p=0.0355$). The LDDMM-surface, LDDMM-curve, and CARET performed equivalently in terms of this overlap ratio.

Figure 4.6 shows SAC measures of each individual sulcal region for the MM-LDDMM (black), LDDMM-surface (gray), LDDMM-curve (pink), FreeSurfer (white), and CARET (blue) mapping algorithms. Regardless of the mapping algorithms, both the central sulcal region and Sylvian fissure had higher SAC values (ranged from 0.35 to 0.45) than other sulcal regions, while the lateral occipital sulcal region had the lowest SAC values (around 0.15). This suggests that the mapping accuracy is highly dependent on the intrinsic anatomical variability of the region. Again, the landmark-based mapping (LDDMM-curve and CARET) provided higher SAC values in the regions where the landmarks were placed. For instance, CARET

Table 4.1: The average overlap ratios (mean(standard deviation, SD)) are listed to quantify intra-reliability of the manual sulcal delineation (the second column) and sulcal alignment accuracy of each mapping algorithm (the rest columns).

Sulcal Region	IR	MM	S	C	FreeSurfer	CARET
Central Sulcus (CeS)	0.95(0.02)	0.63(0.02)	0.59(0.05)	0.60(0.03)	0.63(0.03)	0.61(0.02)
Parieto-occipital Sulcus (POS)	0.95(0.03)	0.57(0.06)	0.53(0.09)	0.54(0.07)	0.54(0.08)	0.53(0.08)
Cingulate Sulcus (CiS)	0.94(0.02)	0.51(0.05)	0.51(0.05)	0.49(0.05)	0.49(0.05)	0.51(0.06)
PostCentral Sulcus (PoCeS)	0.92(0.04)	0.53(0.06)	0.49(0.08)	0.49(0.06)	0.54(0.04)	0.51(0.05)
Collateral Sulcus (CoS)	0.91(0.05)	0.46(0.06)	0.45(0.05)	0.46(0.06)	0.47(0.08)	0.44(0.06)
Superior Frontal Sulcus (SFS)	0.91(0.02)	0.52(0.06)	0.52(0.08)	0.50(0.06)	0.53(0.07)	0.52(0.09)
Inferior PreCentral Sulcus (IPreCeS)	0.91(0.04)	0.47(0.08)	0.37(0.13)	0.40(0.07)	0.39(0.11)	0.25(0.11)
Superior PreCentral Sulcus (SPreCeS)	0.93(0.02)	0.46(0.05)	0.47(0.05)	0.42(0.06)	0.46(0.05)	0.49(0.05)
Inferior Frontal Sulcus (IFS)	0.90(0.05)	0.37(0.08)	0.32(0.08)	0.35(0.08)	0.35(0.10)	0.21(0.12)
Inferior Temporal Sulcus (ITS)	0.91(0.04)	0.42(0.10)	0.39(0.11)	0.38(0.09)	0.39(0.10)	0.37(0.11)
Lateral Occipital Sulcus (LOS)	0.90(0.04)	0.38(0.17)	0.34(0.15)	0.36(0.15)	0.34(0.15)	0.38(0.17)
Sylvian Fissure (SF)	0.96(0.01)	0.64(0.02)	0.63(0.02)	0.56(0.04)	0.64(0.02)	0.62(0.02)
Superior Temporal Sulcus (STS)	0.92(0.02)	0.48(0.05)	0.43(0.08)	0.39(0.05)	0.46(0.06)	0.44(0.06)
Ventral Calcarine Sulcus (CaSv)	0.91(0.02)	0.46(0.07)	0.35(0.12)	0.42(0.08)	0.41(0.08)	0.35(0.09)
Dorsal Calcarine Sulcus (CaSd)	0.91(0.04)	0.44(0.08)	0.32(0.10)	0.42(0.08)	0.41(0.09)	0.40(0.11)
Occipital Temporal Sulcus (OTS)	0.91(0.06)	0.41(0.09)	0.41(0.08)	0.37(0.08)	0.41(0.10)	0.44(0.11)
Intraparietal Sulcus (IPS)	0.92(0.04)	0.51(0.05)	0.47(0.06)	0.44(0.06)	0.54(0.06)	0.51(0.05)

Note: IR—Intra-Reliability; MM—MM-LDDMM; S—LDDMM-surface; C—LDDMM-curve

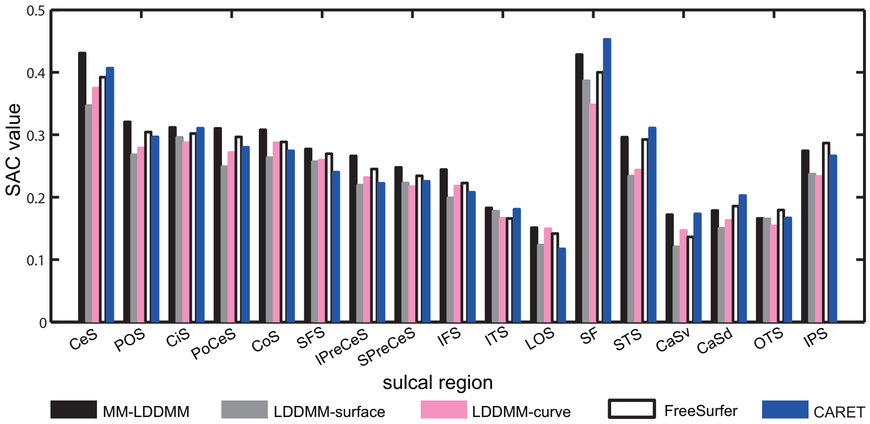

Figure 4.6: Surface alignment consistency of the seventeen sulcal regions are shown for the MM-LDDMM (black), LDDMM-surface (gray), LDDMM-curve (pink), FreeSurfer (white), and CARET (blue) mapping algorithms. The anatomical definition of each sulcal region is illustrated in Figure 4.3. The structural names are listed in Table 4.1.

provided the best alignment in the regions of the Sylvian fissure and superior temporal sulcus. Compared to the LDDMM-surface, the LDDMM-curve had higher SAC values in the regions of the central sulcus, parieto-occipital fissure, postcentral sulcus and so on. Nevertheless, among the three LDDMM mapping algorithms, the MM-LDDMM consistently gave better alignments for all seventeen sulcal regions, suggesting that the MM-LDDMM algorithms aligned the local shapes of the cortex well. The SAC for MM-LDDMM was larger than that for FreeSurfer in 14 out of total 17 sulcal regions except the occipital temporal sulcus, the intraparietal sulcus and the dorsal bank of the calcarine sulcus. The SAC for MM-LDDMM was higher than that for CARET in 12 out of total 17 sulcal regions except the dorsal and ventral banks of the calcarine sulcus, the occipital temporal sulcus, the Sylvian fissure, and the superior temporal sulcus that were involved in or closed to the landmarks in the CARET mapping. Overall, the SAC values averaged across the 17 sulcal regions were 0.27 (±0.08) for MM-LDDMM, 0.26 (±0.08) for FreeSurfer, 0.25 (±0.09) for CARET, 0.24 (±0.07) for LDDMM-curve and 0.23 (±0.07) for LDDMM-Surface. One sample Student's t-tests revealed that SAC for MM-LDDMM was significantly higher than FreeSurfer and CARET (MM-LDDMM vs FreeSurfer: p=0.0011; MM-LDDMM vs CARET: p=0.0107). The FreeSurfer and CARET mappings performed equivalently in terms of the SAC value. This conclusion was in line with that obtained using the overlap ratio of the sulcal regions.

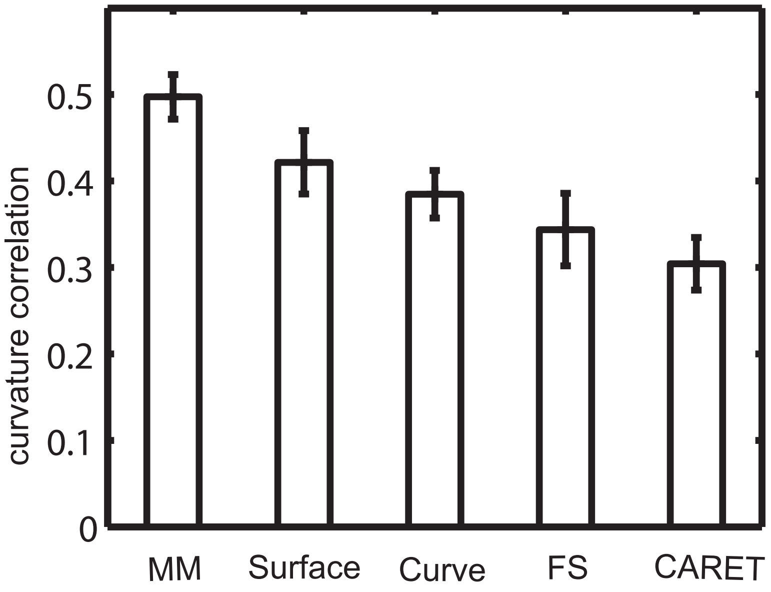

Figure 4.7: Bar plot of curvature correlation for the MM-LDDMM (MM), LDDMM-surface (Surface), LDDMM-curve (Curve), FreeSurfer (FS), and CARET mapping algorithms

4.3.3 Curvature Correlation

Figure 4.7 shows the mean and standard deviation of the curvature correlation between the template and deformed subject surfaces among the 40 subjects. The Student's t-tests on the correlation scores of the 40 subjects revealed the decreasing accuracy of the curvature pattern alignment in the order of the MM-LDDMM, LDDMM-surface, LDDMM-curve, FreeSurfer, and CARET mapping algorithms (MM-LDDMM vs LDDMM-surface: $p<0.0001$; LDDMM-surface vs LDDMM-curve: $p<0.0001$; LDDMM-curve vs FreeSurfer: $p<0.0001$; FreeSurfer vs CARET: $p<0.0001$).

4.3.4 Local and Global Deformation Errors

We quantified how much deformation can be carried out by the MM-LDDMM, FreeSurfer, and CARET mapping algorithms using the ten simulated cortical surfaces whose deformation fields relative to the template surface were known. Figure 4.8(A, B) illustrates two simulated surfaces colored by their true deformation displacement relative to the template surface. The MM-LDDMM, FreeSurfer, and CARET mapping algorithms were directly applied to align these simulated surfaces to the template. Figure 4.8(C-H) shows the deformation displacements carried by the three algorithms. Figure 4.9 illustrates local deformation error maps averaged over the ten simulated datasets and their distribution for each of the mapping algorithms. This

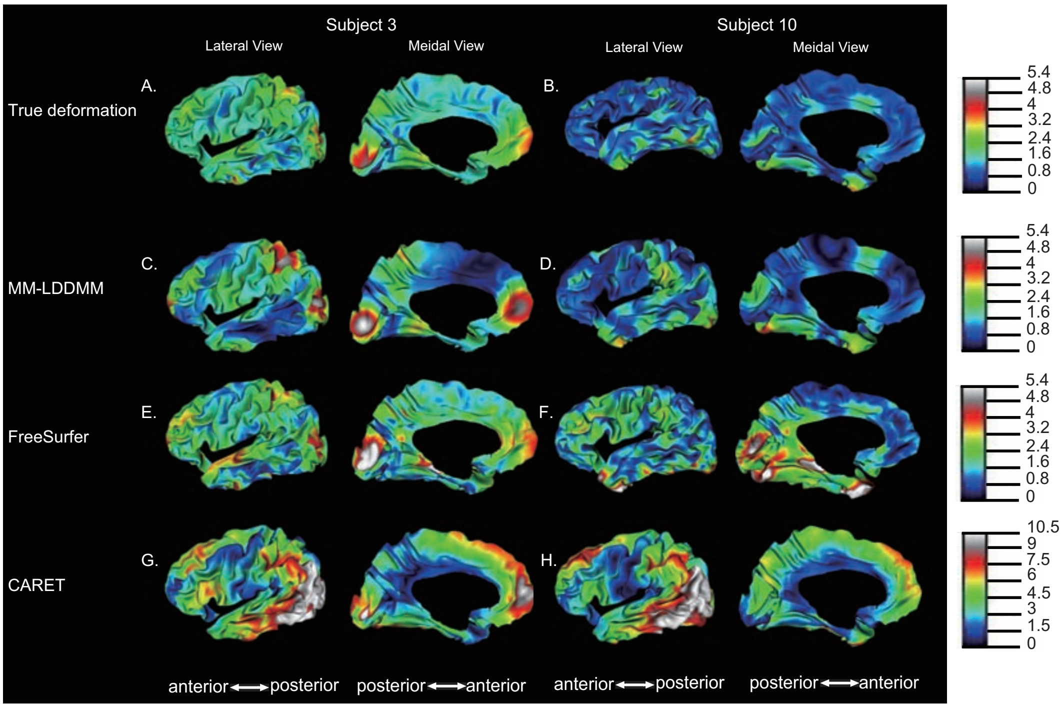

Figure 4.8: Left and right panels show two simulated surfaces colored by deformation displacements of the ground truth (A, B), MM-LDDMM (C, D), FreeSurfer (E, F), and CARET (G, H) relative to the template surface. Each cortical surface is illustrated in both lateral and medial views.

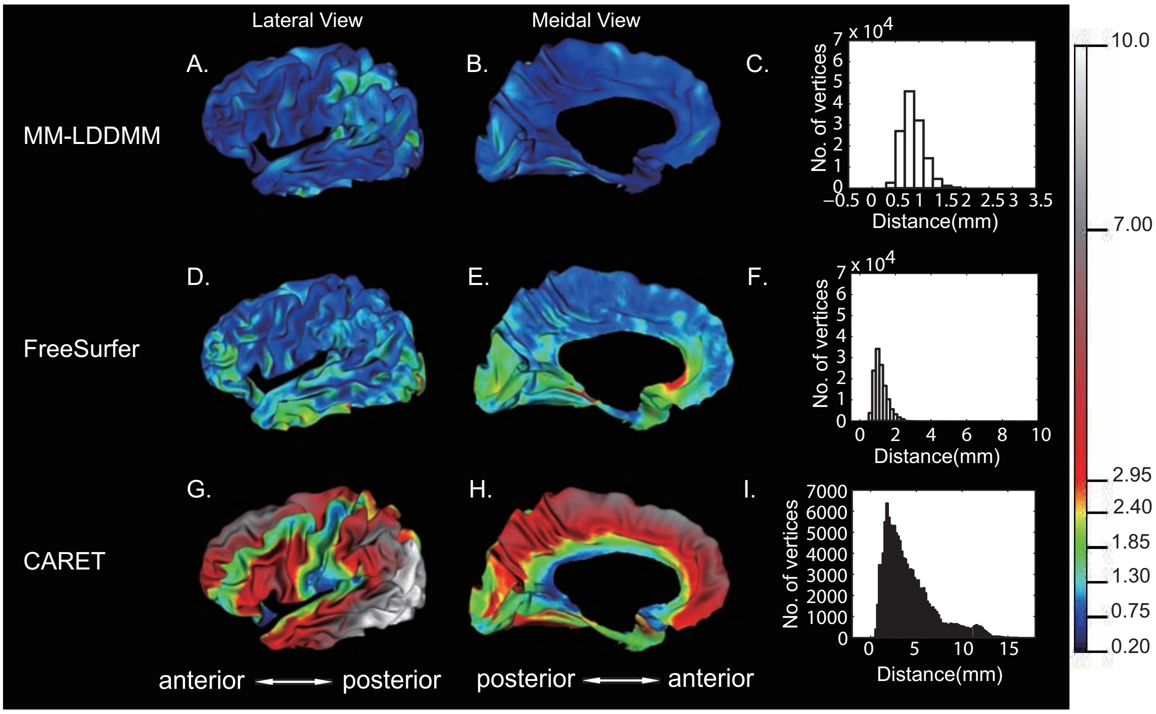

Figure 4.9: The local deformation error maps averaged over the ten simulated cortical surfaces and their distributions are shown for the MM-LDDMM (A-C), FreeSurfer (D-F), and CARET (G-I).

figure indicates that the MM-LDDMM mapping algorithm had the local deformation errors across the entire surface ranged from 0.35 to 1.93mm. 74.4% of vertices had the local deformation errors that were less than 1mm, which is the resolution of MR images. Furthermore, the local deformation errors were relatively uniformly distributed over the surface with the exception of the posterior parietal region. For FreeSurfer, the local deformation errors ranged from 0.43 to 8.74mm. 35.5% of vertices had the local deformation errors that were less than 1mm. Large deformation errors were most apparent in the inferio-medial aspect of the frontal lobe, the inferior region of the temporal lobe, and the occipital lobe. For CARET, the local deformation errors ranged from 0.35 to 16.16mm. 2.85% of vertices had the local deformation errors that were less than 1mm. Small deformation errors occurred in regions adjacent to the curve landmarks involved in the mapping process. Large deformation errors were most pronounced in the superior regions of the frontal lobe, the inferior region of the temporal lobe, and the lateral aspect of occipital lobe. Overall, average global deformation errors across the ten simulated data are respectively 0.87 (±0.14), 1.20 (±0.15), and 4.21 (±0.21) for the MM-LDDMM, FreeSurfer, and CARET cortical mapping algorithms, respectively. Student's t-tests on global deformation errors of the ten simulated datasets revealed the MM-LDDMM, FreeSurfer, and CARET mapping algorithms were ranked as decreasing order in terms of their alignment accuracy (MM-LDDMM vs FreeSurfer: $p=0.0006$; FreeSurfer vs CARET: $p<0.0001$).

4.4 Discussion

We quantitatively evaluated the accuracy of the five cortical surface mapping algorithms (MM-LDDMM, LDDMM-surface, LDDMM-curve, FreeSurfer, CARET) using the 40 MRI scans and 10 simulated datasets. We computed the curve variation error, overlap ratio of sulcal regions, and surface alignment consistency for assessing the mapping accuracy of local cortical features and the curvature correlation for measuring the mapping accuracy in terms of overall cortical shape. Furthermore, the simulated datasets facilitated the investigation of mapping error distribution over the cortical surface when the MM-LDDMM, FreeSurfer, and CARET mapping algorithms were applied. Our results revealed that the LDDMM-curve, MM-LDDMM and CARET approaches best aligned the local curve features involved in these mapping algorithms. The MM-LDDMM approach best aligned the local regions and cortical shape patterns (e.g. curvature) as compared to the other mapping approaches. The simulation experiment also revealed that the MM-LDDMM mapping had less local and global deformation errors than the CARET and FreeSurfer mappings. The deformation errors in the MM-LDDMM mapping were relatively uniformly distributed over the surface, but they were not apparent in the same manner in the CARET and FreeSurfer mappings.

Among the five mapping algorithms, LDDMM-curve and CARET registered cortical surfaces based on gyral/sulcal curves, while FreeSurfer and LDDMM-surface aligned cortical surfaces based on features or geometry of the entire cortical surface. As expected, our study showed that the LDDMM-curve and CARET mappings characterized curve anatomical variations and regions adjacent to landmarks well when compared to the FreeSurfer and LDDMM-surface. Thus, LDDMM-curve and CARET can be suggested as the suitable methods in studies on anatomical variations of curves and sulcal regions as well as functional or anatomical studies in specific ROIs (93, 145). FreeSurfer and LDDMM-surface mapping algorithms may be more appropriate for cortical parcellation when anatomical priors are not available and for whole brain exploratory studies. Nevertheless, statistical outcomes from group studies using these methods may be spurious and dependent on the pattern of the deformation errors as those illustrated in Figure 4.9. This can be overcome by introducing weight functions into the FreeSurfer and LDDMM-surface algorithms, where weight functions are defined by adapting regionally-specific anatomical variations obtained from postmortem studies (3). The MM-LDDMM algorithm was a more advanced technique that takes advantage of the strengths of both the landmark-based and surface-based cortical mapping approaches by incorporating anatomical priors and minimizing dissimilarity of cortical shape patterns. As automated methods for gyral/sulcal curve delineation (146, 147) are made available, the MM-LDDMM mapping will be easily used for mapping cortical surfaces in a variety of studies.

In this chapter, we classified the mapping algorithms in FreeSurfer and CARET as the spherical-based approaches and the LDDMM algorithms as native-space based approaches. Our results showed that the LDDMM-curve mapping accuracy was comparable to that of the CARET mapping and the LDDMM-surface mapping provided comparable alignments to the FreeSurfer in terms of the curve variation errors, SAC, and curvature correlation. Nevertheless, the MM-LDDMM mapping had more uniform deformation errors and provided better alignment of the sulcal regions when compared with FreeSurfer and CARET. The evidences observed in this study suggested that warping cortical surfaces in their own native folded space in general produced comparable or potentially better alignments as that in the spherical space. One reason could be due to the distortion introduced during the surface parameterization.

In terms of computation time, under the same computer setting, LDDMM-curve and CARET took around 5 minutes to finish the mapping of one surface, while LDDMM-surface, MM-LDDMM and FreeSurfer took around one hour to finish surface mapping. This is as expected because LDDMM-curve and CARET only used the coarse information -curves, as the constraint for registration. And LDDMM-surface, MM-LDDMM and Freesurfer used the information from the whole surface as constraints, which was much more than the curve information. While we already showed that MM-LDDMM can perform better than CARET and Freesurfer in both local and global alignment, it would be worth of computation time due to the importance of high registration accuracy in group structural and functional studies(9).

The quantitative measurements (curve variation errors, SAC, and curvature correlation) involved in our study have been previously examined in several existing studies for assessing and evaluating landmark-based and surface-based cortical surface registrations (87, 93, 143). We chose these measurements because they were commonly used and can become standard measures for evaluating accuracy of cortical surface mapping algorithms. Moreover, they can quantify mapping accuracy from the aspects of both local (gyral/sulcal curves and sulcal regions) and global (curvature pattern) anatomical features. Using these measures allowed us to compare our study with previous studies and extend our findings to other mapping algorithms that we did not investigate in this study. Pantazis (2009) suggested that the FreeSufer mapping was better than the landmark-based approach (148) and Brainvoyager (version 1.9.10) (149) in terms of curvature correlation. Taking the above into consideration with our findings, the LDDMM mapping algorithms were likely to also provide better alignment than the landmark-based approach (148) and Brainvoyager (149) . Furthermore, Van Essen (87) computed SAC of eighteen sulcal regions for the CARET mapping. These sulcal regions were all included in our study, with the exception of the middle frontal sulcus which we cannot reliably delineate. Our results for the CARET mapping were consistent with those in Van Essen (87) according to the SAC distribution across the sulcal regions, i.e., high SAC values in the Sylvian fissure and central sulcal regions and low SAC values in the lateral occipital sulcal region. However, SAC values in our study for each sulcal region were lower than those reported in Van Essen (87), which may be because MRI scans used in our study were from healthy subjects in a wide age range (20 80 years old) and dementia subjects while MRI volumes of only young healthy adults (18 24 years old) were incorporated in Van Essen (87). To ensure that the SAC value was reasonable when compared with that reported in Van Essen (87), we recalculated it for the CARET mapping based on the ten young subjects in our study. The averaged SAC value across the seventeen sulcal regions was 0.29 for the CARET mapping, while it was 0.34 in Van Essen (87). This discrepancy could be due to the difference in templates. In Van Essen (87), the average template was created using the same subjects as those in the validation. However, a single subject template was used in our study, which could potentially increase mapping errors. An average template was not able to be used in our study since the evaluation of the cortical surface alignment may be biased to the mapping algorithm for the template construction. We have made all datasets, including MRI scans, manually delineated curves and sulcal regions, and simulated surfaces, available online (`www.bioeng.nus.edu.sg/cfa/mapping/index.html`) for researchers' further investigation.

5

Template Generation for the Sulci and Cortical Hemispheric Surfaces

Brain registration has been widely applied in brain structural and functional studies for shape analysis and functional location identification (e.g. (133, 150, 151))). While brain registration accuracy is template dependent, a suitable template which can represent the brain morphology and individual variability would lead to more reliable result for those structural and functional studies. As the existing template generation procedure depends on the registration accuracy, better registration method would give a more representative template. Having developed MM-LDDMM registration method and showed its better registration performance, a representative template can be generated based on it and would be useful for other structural and functional studies.

5.1 Introduction

Cortical convolutions of the human cerebral cortex are very complex and vary greatly from one individual to the other. Due to the large variations in brain anatomical shape across human populations, the construction of a suitable template that can represent morphology and individual variability, which human brain registration and the statistical analysis for the functional study are dependant on, has received great attention.

Some human cortical templates are represented by an individual brain or hemisphere, which accurately represents cortical shape in the selected individual but fails to represent variability across population (83, 152). The wide structure variation of individual subject relative to the single-subject template may cause the failure of the brain registration. Other templates are obtained based on averaging MRI volumes in a population via linear registration (153, 154) which have been widely used in functional studies and volume-based morphometry (VBM) (154, 155, 156). Although these averaging template can capture some shape consistencies across subjects, but the detailed anatomical information was blurred. Recently, researchers developed the template generation methods based on high-dimensional non-rigid registration (157, 158, 159), which can give more detailed cortical structural information than the linear-averaged template. However, as the cortical structure with sulci and gyri is important in functional brain registration and surface-based registration, the surface-based brain template is also attractive (5, 87, 110, 140). Van Essen (5) did a comprehensive work on developing a Population-Average, Landmark- and Surface-based (PALS) atlas of human cerebral cortex. The PALS-12 is a surface-based population-average atlas of 12 normal young adults, which incorporates spherical non-rigid registration method. This study shows that fMRI findings were biased when using single subject as a template while the use of average template can avoid this bias as average template can represent morphology and individual variability. Lyttelton et al. (110) developed a surface group template which is an unbiased, high-resolution iterative registration template from a group of 222 subjects hemispheres. The resulting template provided better alignment of subjects than single-subject templates. Recently, Allassonniere et al. (160) and Ma et al. (161) developed a probabilistic framework coupled to the expectation-maximization (EM) algorithm for generating templates from populations. This template is metrically centered via the diffeomorphic metric (119), which has been used to construct the template for the subcortical structures (162, 163). As these template generation processes are all based on registration between subjects, the representation of the new template will be affected by the registration accuracy. Thus only good registration during the template generation process would give meaningful new template over a population.

In chapter 4, we have shown that our MM-LDDMM algorithm can align the local regions and cortical shape patterns (e.g. curvature) better as compared to the other LDDMM mapping approaches, CARET and FreeSurfer algorithms. In this chapter, we aim to generate an average template via the diffeomorphic metric using our MM-LDDMM algorithm with the template generation method proposed by Vaillant et al., (121).

5.2 Methods

5.2.1 MM-LDDMM Template Generation

The MM-LDDMM algorithm provides the optimal initial momenta that encode the shape variations of the target surface relative to the template surface in a linear space. This reduces the problem of studying shapes of a population in a nonlinear diffeomorphic metric space to a problem of studying the initial momenta in a linear space as has been done for landmarks and surfaces by (121, 164). Thus, it provides a natural way for computing the average of the cortical shapes among a population by calculating the mean of the initial momenta. We extended the previous template generation for landmarks (121) using the geodesic shooting of the averaged initial momenta to one for the sulcal curves and cortical surfaces when the MM-LDDMM algorithm is served as a diffeomorphic mapping tool. This template estimation requires minimization of the functional

$$
\begin{aligned}
J(\boldsymbol{\alpha}_{\mathbf{0}}^{(\boldsymbol{k})}, \gamma_{temp}, S_{temp}) \quad = \quad & \inf_{\boldsymbol{\alpha}_{\mathbf{0}}^{s}, \boldsymbol{\gamma}_{\boldsymbol{temp}}, \boldsymbol{S}_{\boldsymbol{temp}}} \sum_{k=1}^{N} \Big[\sum_{i=1}^{n} \sum_{j=1}^{n} \alpha_j^{(k)}(0)^* [k_V(x_i(0), x_j(0)) \alpha_i^{(k)}(0)] \\
& + \sum_{i=1}^{n_c} \beta_{\gamma_i} E_{\gamma_i}(\phi_1 \cdot \gamma_{temp}^{i}, \gamma_{targ}^{i(k)}) + \sum_{i=1}^{n_s} \beta_{S_i} E_{S_i}(\phi_1 \cdot S_{temp}^{i}, S_{targ}^{i(k)}) \Big],
\end{aligned}
$$

where N denotes the number of subjects, γ and S denote the curves and surface. For detailed information about this equation, please see section 3.2.2 in chapter 3. Once the template of the curves and the cortical surface is initialized, the MM-LDDMM algorithm is applied for seeking the optimal initial momentum that generates a trajectory connecting the template to subject $k, k = 1, 2, \cdots, N$. The mean of the initial momenta among all subjects represents the average of the cortical shape variation, which is thus used to generate a new template via the geodesic shooting given in Eqs. (3.5) and (3.6).

5.2.2 Subjects and Process

We randomly selected forty subjects with ten youths (5 males and 5 females, age: 23.4±2.55), ten adults (5 males and 5 females, age: 49.3±1.89), ten elders (5 males and 5 females, age: 73.9±2.02), and ten patients with dementia (5 males and 5 females, age: 76.4±2.55) from the OASIS dataset (126) based on gender, age, and diagnosis. The initial template was produced by using an MR image from a female subject aged 54, which was not otherwise included in the

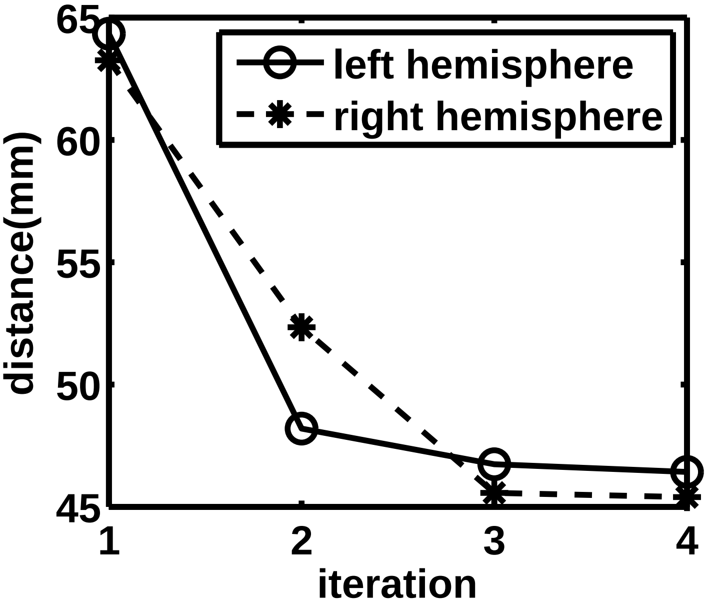

Figure 5.1: Figure shows the metric distance averaged among the forty subjects in every iteration of the template generation process. Solid and dashed lines respectively correspond to the left and right cortical hemispheres.

forty subjects. The cortical surface and its fourteen sulcal curves were extracted according to the description given in Section 3.2.3.

The deformation from the template to the 40 subjects was performed iteratively. During each iteration of the template generation, the initial momenta encoding the deformation of the updated templates to each individual subject were found by following the MM-LDDMM mapping process given in Section 3.2.3. The new templates for the sulcal curves and surfaces were updated by solving the geodesic shooting equations in Eqs. (3.5) and (3.6) when the initial momenta averaged among the forty subjects were given as initial conditions. The template generation process was stopped when the change of the mean metric distance over the forty subjects in two subsequent iterations was less than 5% (Figure 5.1). Total of four iterations were taken in the template process.

5.3 Results

Figure 5.2(A,B) show the initial and estimated templates of the left and right cortical hemispheres in the lateral and medial views. To inspect shape differences between the initial template and the estimated template, we computed the Euclidean distance between their correspondence points. Figure 5.3 shows the estimated templates colored by this distance measure, which indicates the middle frontal, lateral parietal, lateral and basal temporal regions, anterior cingulate, precuneus, as well as calcarine region with large distances in both left and right hemispheres. This suggests that these regions are anatomically highly variable across individuals. To be specific, major sulci on the estimated template are less deep and gyri are less sharp than those on the initial template because of sulcal and gyral variations in the population (see arrow in Figure 5.2(A)). Small sulci or gyri were removed in the estimated template. For instance, the arrow in Figure 5.2(B) points the place where in the medial superior frontal region becomes flat after the template generation process. Nevertheless, our estimated templates provide more detailed sulco-gyral pattern than those in (5). This evidence has also been indicated in the MRI volume template estimation: i.e., better alignments create image templates with more detailed structures (118, 165, 166).

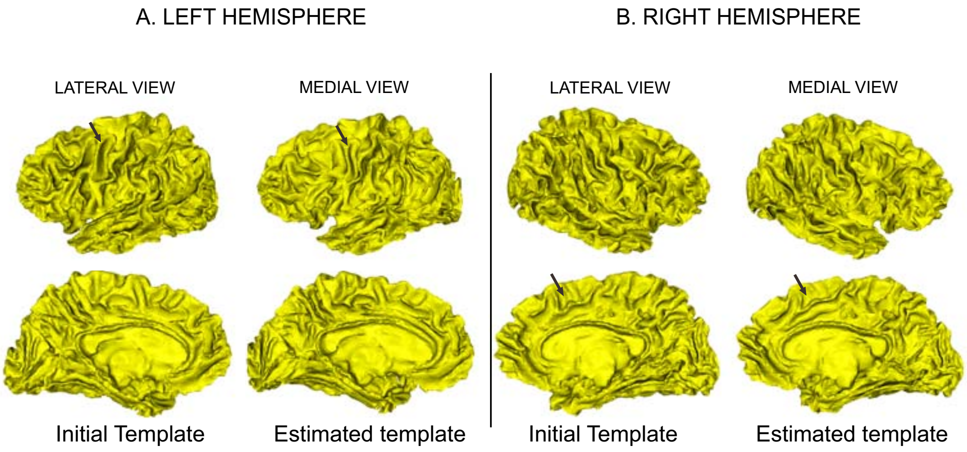

Figure 5.2: Panels(A,B) respectively show the initial template (left column) and estimated template (right column) of the left and right hemispheres. The lateral view is shown in the top row; the medial view is shown in the bottom row. The arrow on panel A points out the region where becomes less deep or less sharp on the estimated template. The arrow on the panel B points out the superior frontal region with small gyri and sulci on the initial and estimated templates.

5.4 Discussion

In this chapter, we generated an average template based on the newly developed MM-LDDMM algorithm. As this algorithm was developed based on a conservation law of momentum for the geodesics of diffeomorphic flow (119, 120), the initial momenta obtained from the MM-LDDMM characterize non-linear shape variations across anatomies in a linear space, which provides a simple way to compute the average of the anatomical deformations via the average of the initial momenta and then construct average geodesic in a metric shape space through the geodesic shooting. This has previously been studied for paired landmark points (121). Our estimated templates for the cortical surface (download from `http://www.bioeng.nus.edu.sg/cfa/template/index.html`) maintain the detailed sulco-gyral pattern but not limit to major deep sulci as shown in (5), which indicates that the MM-LDDMM algorithm improves the quality of the alignment. The estimated template will be useful in the shape study on cortical structures in a variety of neurodegenerative diseases and healthy aging. It is representative for the population in terms of its metric distance to each individual subject in the population.

Regarding to the use of MM-LDDMM algorithm to generate average templates, the surfaces must be completed surface. If the subject surfaces have infarction, it would not be able to generate average surface across subjects as the correspondence would not be correct. If an average template for clinical groups is needed, e.g. dementia group, researchers can choose those subjects with dementia but the surfaces are well preserved, so that the average template can contain the characteristics of the dementia group.

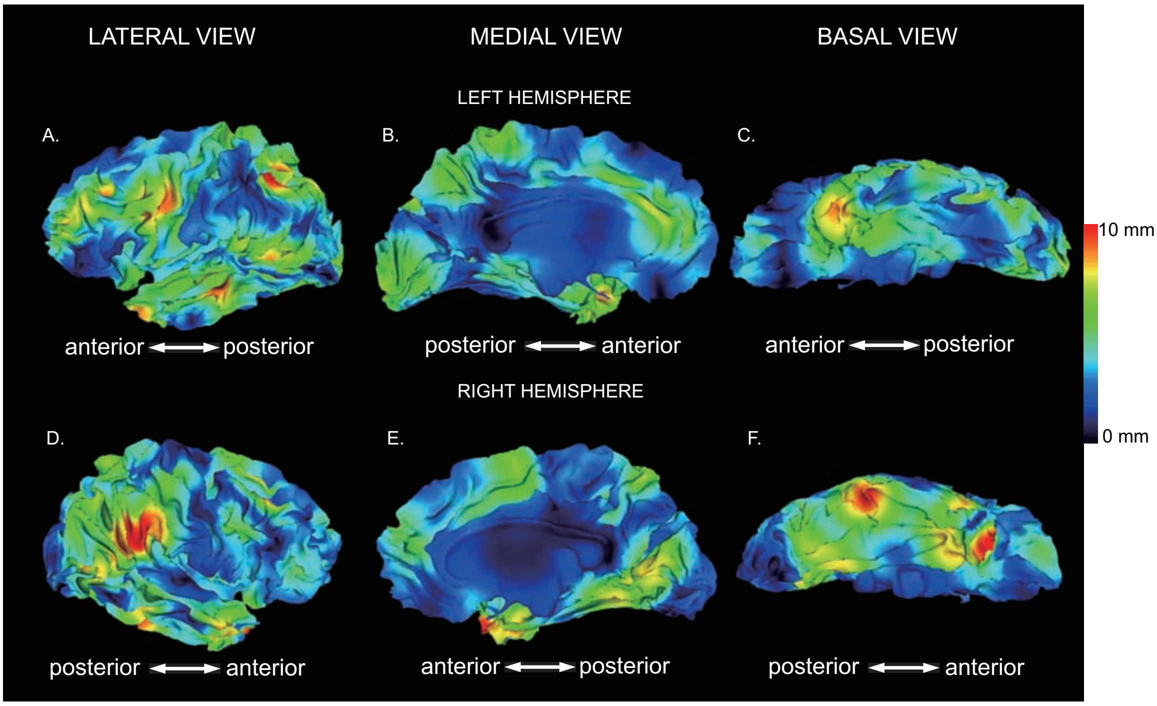

Figure 5.3: The top row shows the left estimated template surface colored by its distance to the initial template surface in Figure 5.2 (A). The lateral, medial, and basal views are respectively shown in panels (A, B, C). Similarly, the right estimated template surface is illustrated in panels (D, E, F).

6

Intrinsic Functional Networks in Six-year-old Healthy Children: a large scale resting-state fMRI study

Other than used in structural studies, brain registration is widely used in functional group studies for defining location with particular function (1, 167, 168). Cortical surface spherical registrations have been shown with superior power in detecting functional activations as compared to automated Talairach registration (2) and affine volume-based registration approaches (9). As we have demonstrated the better registration performance of MM-LDDMM in controlling both local and global information with comparison to the widely used spherical registrations in CARET and FreeSurfer, our MM-LDDMM can be applied to functional studies for investigating the functional activations and connectivities. In this chapter, we would apply the MM-LDDMM method and investigate functional connectivity in six-year-old healthy children, which fills the gap for understanding the brain intrinsic functional networks in young healthy children while the early childhood is critical for detecting neurodevelopmental disorders.

6.1 Introduction

The human brain is a complex network, in which spatially distributed regions were linked with similar functions by continuously sharing information with each other. This network keeps changing and reshaping through development into adulthood by both structural dynamics (e.g., myelination, synaptic pruning, or lesions (77, 169, 170, 171, 172, 173) and functional dynamics

(59, 72, 80, 174, 175, 176, 177). Understanding this network and its trajectory across human life span is necessary for us to investigate the network's organizational changes during the neurologic and psychiatric brain disorders, including ADHD, Alzheimer's disease, depression, dementia and schizophrenia. While there are a lot of studies investigating the infants (57, 61, 62) and adults (37, 178, 179) functional networks, it is not clear about the brain intrinsic functional networks in young healthy children. However, the early childhood is a critical period for detecting neurodevelopment disorders whose origins are mainly in infancy or during childhood, such as ADHD. Although there is one study by de Bie et al. (180) investigating the resting state networks in children aged between 5 and 8 years old, they only studied a small sample (18 subjects) and failed to investigate the networks for each age group. While the subjects between 5 and 8 years old differed in education and Rosenberg-Lee et al (181)showed even the narrow one-year interval was characterized by significant arithmetic task-related changes in brain response and connectivity for children between 7 and 9 years, we would predict there are significant developmental changes during early childhood between 5 and 8 years old. Thus, combing the data from children between 5 and 8 years old and studying them together may fail to present age-specific information. This study fills this gap and presents the first large-scale rsfMRI study to investigate primary sensory networks, higher-level cognitive networks, and default mode network (DMN) in six-year-old healthy children.

Recently, functional MRI were introduced to measure the brain's activity noninvasively and examine the functional connectivity between brain regions. Functional connectivity is defined as the temporal correlation of neuronal activities measured in different brain areas (30). In the past 15 years, increasingly studies started to measure the functional connectivity between brain regions by using spontaneous blood-oxygen level-dependent (BOLD) signal fluctuations, recorded during resting state (36, 178, 182). Resting-state fMRI is a relatively novel fMRI approach which can overcome the limitations met by the task-related fMRI study. Because task-related study needs the subjects to finish a task in the scanner, while some clinical populations with cognitive impairment may have difficulty to do so. In contrast, during these resting-state fMRI (rsfMRI)scanning, subjects are only required to rest quietly with their eyes closed for several minutes with their spontaneous BOLD signal fluctuations measured. During the resting state, the spontaneous low-frequency (< 0.08 Hz) fluctuations (LFF) of the blood oxygenation level-dependent (BOLD) signal are presented and show high temporal correlations between spatially distinct but functionally related regions (22, 36, 52, 75). Numerous rsfMRI studies have found functional connectivities in somatomotor cortex (22), visual cortex (32), auditory cortex (52, 75, 183, 184, 185) several other higher order cognitive networks (79, 179, 186), and the default mode network (36, 37, 187). During human brain development, the default mode network was found to exist in early childhood and even infancy (62, 188) but with stronger correlation between some components of the network than that in the adults (80, 81). For the higher cognitive connectivity, it was found that networks are more specialized with development (186, 189). But there is still lack of information about how the networks like for 6-year old children.

There are two kinds of methods to process the rsfMRI: data-driven and model-dependent methods. Data-driven approaches include the Independent or Principal Component Analyses (48, 55, 190, 191, 192), clustering (185) method, etc. They can examine the general patterns of whole-brain connectivity. However, it is difficult to explain the network detected by these methods. In contrast, the model-dependent method, also called seed-based method, provides a clear view of with which regions a particular region (called as seed) is functionally connected. It examines the temporal correlation of the resting state time course of a seed region with the time course of all other regions, resulting in a functional connectivity map defining the functional connections of the seed region. Thus, it provides an elegant and straightforward way for examining functional connectivity in the human brain. For example, seeds in visual cortex tend to result in maps that highlight occipital cortex (32), demonstrating high correlations in rsfMRI signal throughout the visual system.

Thus, in this chapter, we investigated functional connectivity in six-year-old healthy children with the seed-based method. To constrain the gender related differences in brain activation patterns (193, 194), only boys were studied to get relatively accurate intrinsic networks in this small age range. We studied the primary sensory networks, the default mode network, and the networks associated with higher cognitive functions. Generally we expected to find a similar pattern of functional connectivity in children for primary networks as it is involved in primary information processing and more diffuse pattern of connectivity for higher order functions which would be influenced more by emotion, cognitive and environment factors. This study will enrich our understanding of children's intrinsic functional networks.

6.2 Materials and Methods

6.2.1 Subjects

Ninety-one children (all boys, average age=78 ± 3.5 months) participated in this study after providing written informed consent from their parents. The study protocol was approved by the Institutional Review Board of National University of Singapore. The children recruited were healthy, ethnically Chinese, Singaporean boys.

6.2.2 Image Acquisition

Structural and functional MR images were acquired using a 3 Tesla Siemens Magnetom Trio system (Siemens, Erlangen, Germany).

Structural MRI: A high-resolution T1-weighted Magnetization Prepared Rapid Gradient Recalled Echo (MPRAGE) was applied to generate the anatomical image. Volumes consisted of 160 axial slices of 1 mm thickness with no gap (voxel size = 1×0.99×0.99; TR = 2 ms; TE = 2.08 ms; flip angle = 9°; FOV = 190×190 mm; acquisition matrix = 192×192).

Functional MRI: During the resting state, subjects were instructed not to think of anything in particular, but just simply to keep their eyes closed. Functional images were acquired using single-shot echo-planar imaging (EPI) with 42 ascending 3 mm (no gap) axial slices parallel to the AC-PC plane (voxel size = 2.969×2.969×3; TR = 2.4 s, TE = 27 ms; flip angle = 90 °; FOV = 190 mm; acquisition matrix = 64×64). The functional imaging lasted for 6 minutes and 150 EPI volumes were collected in total.

6.2.3 Data Preprocessing and Analysis

6.2.3.1 Structural MRI Data Preprocessing

The structural images were first transformed to the Montreal Neurological Institute (MNI) space by affine registration (195) and then the inner/outer surfaces of individual hemispheres were segmented and reconstructed in Freesurfer (`http://surfer.nmr.mgh.harvard.edu`). The center of the inner and outer surfaces was then generated as fiducial surface to be geometric representation of the cortex in the rest of the paper. To allow group analysis, we employed a multi-manifold large deformation diffeomorphic metric mapping (MM-LDDMM) algorithm

(136) to align the subjects' cortical fiducial surfaces to a template generated from one participant in the study, while the alignment accuracy of the algorithm has been evaluated in Zhong et al., (196).

6.2.3.2 Functional MRI Data Preprocessing

The functional scans were first preprocessed with slice timing, motion correction, skull stripping, band-pass filtering (0.01-0.08 Hz) and grand mean scaling of the data (to whole brain modal value of 100) using SPM5 (Wellcome Trust Centre for Neuroimaging) and FSL (`www.fmrib.ox.ac.uk/fsl/`). To remove several sources of spurious or regionally nonspecific variance, regression of nuisance variables including six parameters obtained by motion correction, ventricular and white matter signals was conducted and the residual volumes were retained as the resting state signals. Thus, the breath-to-breath effects, with frequency of 0.3 Hz, are removed by the band-pass filter. The cardiac and respiratory signals are removed by removal of the signals from the ventricles and white matter instead as those regions contain a relatively high proportion of noise caused by the cardiac and respiratory cycles (197, 198).

The fMRI data was analyzed on a cortical surface model as surface-based registration is superior to volume-based registration in fMRI group analysis (9). To allow surface-based fMRI analysis, the preprocessed fMRI images were first aligned to their corresponding structural images by rigid registration and then projected to their corresponding cortical surface and hippocampal surface. During the projection, the functional data in the 3D volume was assigned to vertices on the surface based on their locations (199). For fMRI group analysis, individual functional data were transferred to the template surface based on the correspondence derived from the MM-LDDMM and spatially smoothed on it via orthonormal bases of the Laplace-Beltrami operator (equivalent to Gaussian smoothing with a kernel of 12 mm FWHM) (113, 144) to remove the noise.

6.2.3.3 Data analysis

Functional networks were examined using a seed-based correlation method. The time series of each seed were averaged over the 8 mm square region centered on foci defined on the template in the MNI space (Table 6.1). These seed ROIs included seeds defined for primary visual (VC) (200), somatomotor (SM) (22, 201) and auditory (Aud) (202) networks, for the higher order cognitive networks: attention network (37) (the intraparietal sulcus (IPS)) and the executive control network(the bilateral anterior insula/frontal opercular region (LOP and ROP) (203), and for default mode network (the lateral parietal cortex (LP), the medial prefrontal cortex (MPFC), and the posterior cingulate/precuneus region (PCC)) (204). While the above mentioned literatures gave the coordinates of the seeds in the Talairach space, we transformed them into the MNI space using a non-linear transformation (`http://imaging.mrc-cbu.cam.ac.uk/imaging/MniTalairach`), this may present some discrepancies on the location of the seeds. However, visual comparison of the locations in our template and the literatures shows they are still in the very similar region. While our seeds are 8 mm square regions around the seed centers, this made the influence of the discrepancy not so significant. Figure 6.1 showed the seed ROIs on the template surface for visualization.

Table 6.1: Regional network seeds.

Network	Seed Region name	MNI coordinates (X Y Z)		
Sensory	Left visual (LVC)	-19	-99	-9
	Right visual (RVC)	23	-99	5
	Right somatomotor (LSM)	-39	-29	54
	Right somatomotor (RSM)	38	-29	51
	Left auditory (LAud)	-57	-15	12
	Right auditory (RAud)	53	-17	13
Attention	Left intraparietal sulcus(LIPS)	-23	-70	46
	Right intraparietal sulcus (RIPS)	26	-62	53
Executive Control	Left operculum (LOP)	-35	14	6
	Right operculum (ROP)	36	16	5
Default Mode	Left lateral parietal (LLP)	-47	-67	36
	Right lateral perietal (RLP)	53	-67	36
	Left medial prefrontal (LMPFC)	-3	39	-2
	Right medial prefrontal (RMPFC)	1	54	21
	Posterior parietal/precuneus (PCC)	-2	-39	38

6.2.3.4 Statistical Analysis:

Functional connectivity is computed as the correlation between the average time courses within the seed region and every vertex on the left and right cortical surfaces. Correlation maps were converted to z maps using Fisher's r-to-z transformation (205) so that the distribution of the correlations can be normalized. The group data were evaluated using a random effect analysis. A one sample t-test was conducted to obtain regions reliably correlated across subjects.

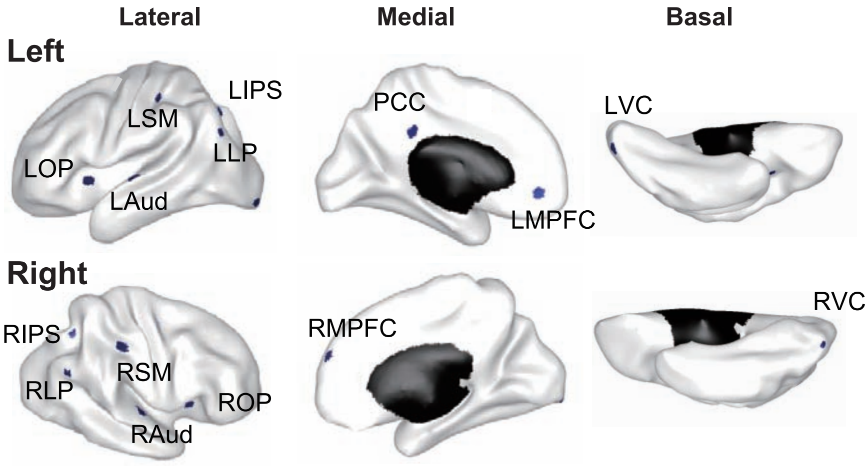

Figure 6.1: The seed ROIs on the template surface in the lateral, medial and basal views. The seed names are listed in Table 6.1.

For visualization, the t-statistical maps were generated on the smoothed surface template and thresholded at an uncorrected significance level of $p < 0.001$.We set a cluster size threshold at 123 mm^2, corresponding to a corrected significance level of $p < 0.05$.

6.3 Results

Figure 6.2 shows intrinsic primary sensory networks, including visual, somatomotor, and auditory networks. These networks mainly involve their own primary and association cortices. The auditory network also involves primary motor cortex, somatosensory cortex, supplementary motor area (SMA), anterior cingulate cortex (ACC), ventral ACC (vACC), insula, cuneus and lingual gyrus.

Figure 6.3 shows the attention, executive control networks, and Figure 6.4 shows default mode network. The attention network connected to the intraparietal sulcus (IPS) involves the dorsal and ventral attention pathways, such as the frontal eye field, inferior precentral sulcus, middle frontal gyrus, and IPS extending to the lateral occipital cortex and inferior temporal gyrus. The executive control network includes the insula/operculum, inferior frontal, orbital frontal and anterior cingulate cortex. The posterior cingulate (PCC), middle temporal gyrus, inferior parietal, superior frontal gyrus extending to ventral medial prefrontal cortex (vMPFC) are present in DMN.

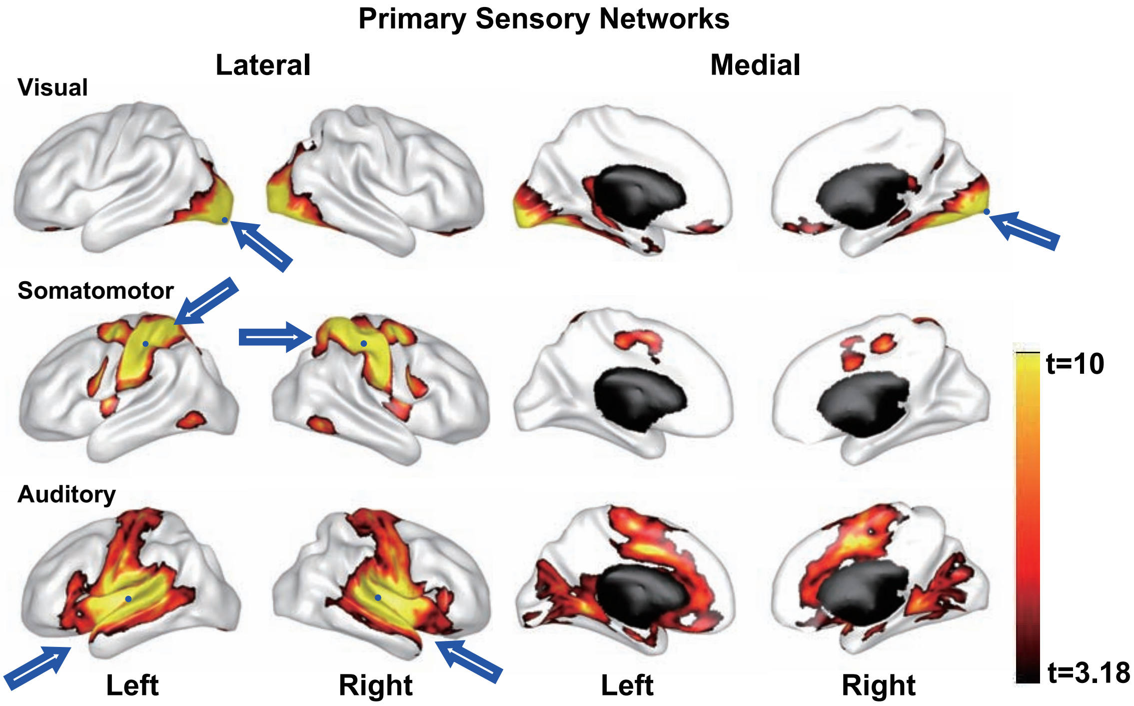

Figure 6.2: Primary sensory networks in children are shown. Seed ROIs are indicated by blue dots in all cases, and the blue arrows are pointing the seed ROIs for your reference.

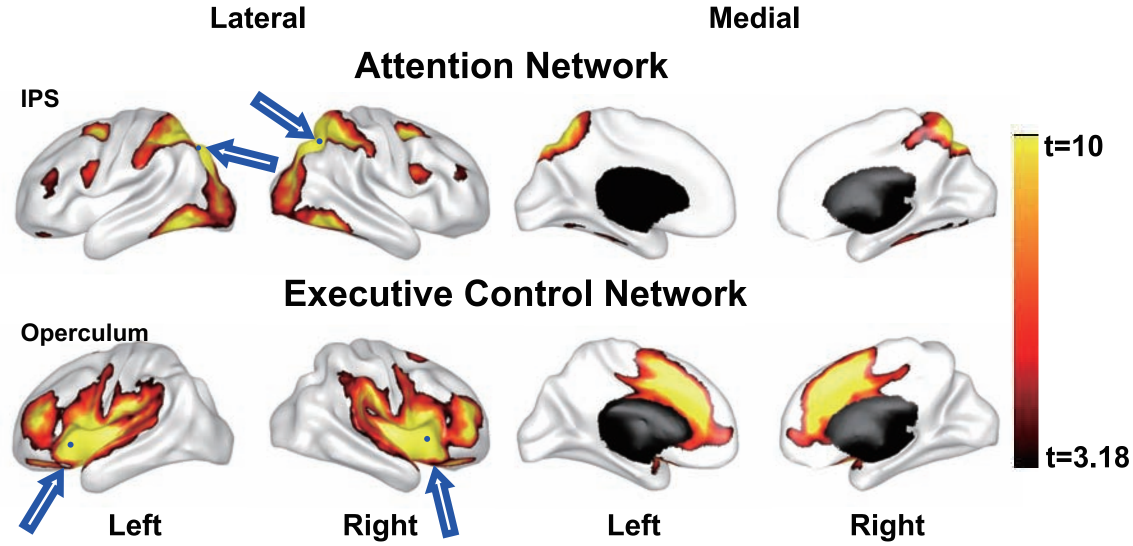

Figure 6.3: Higher cognitive networks for attention and executive control in children are shown. Seed ROIs are indicated by blue dots in all cases, and the blue arrows are pointing the seed ROIs for your reference.

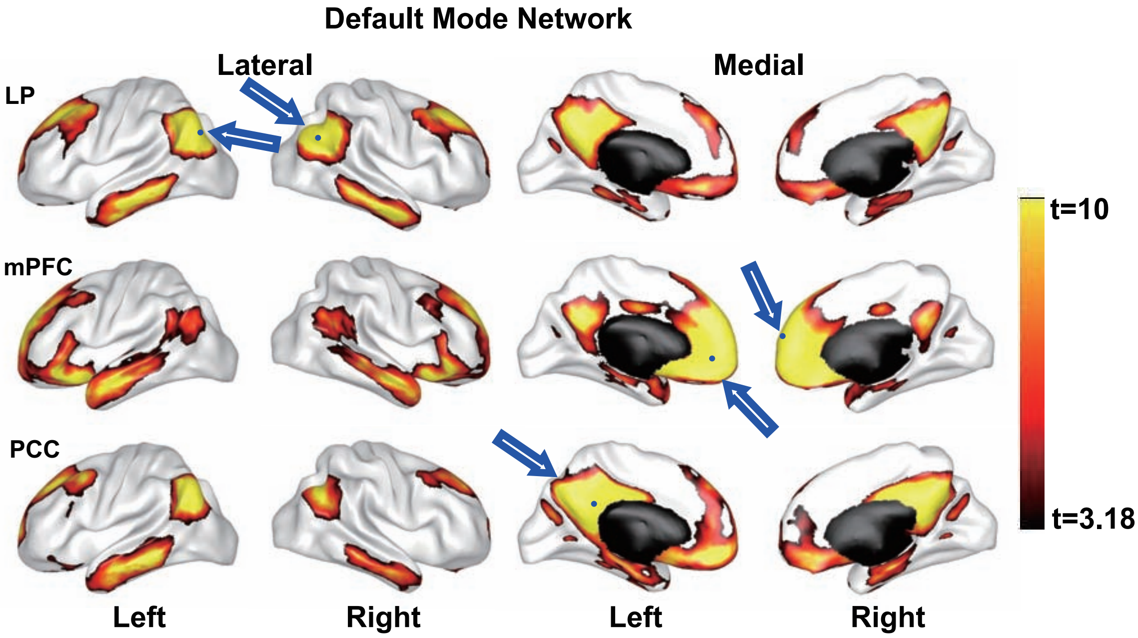

Figure 6.4: Default mode networks in children are shown. Seed ROIs are indicated by blue dots in all cases, and the blue arrows are pointing the seed ROIs for your reference.

6.4 Discussion

In this study, we examined cortical functional networks in 91 6-year-old children based on resting state fMRI. Through seed-based correlation analysis, we found primary visual, somatomotor and auditory networks, higher order networks such as the attention and executive control networks, and default mode network. The results suggest that the primary visual and somatomotor networks are well-developed in early childhood but the auditory, attention, executive networks, and DMN are still in the maturation process at six years of age.

Primary networks: Primary visual and somatomotor networks included the primary cortices and the corresponding associated cortices respectively. The related regions are similar to those of infants (57, 61), older children (79) and adults (183, 206) which are known to be active for visual and somatomotor processing respectively. This is reasonable as the structural and functional development of these regions starts earlier and faster than the frontal regions (207, 208) and the basic configuration of functional networks in the brain has been established by the age of 12 (79). However, the primary auditory networks not only included the primary auditory cortex and auditory association cortex, but also other regions like the motor related cortex, insula, cuneus/lingual gyrus and SMA. Thus the auditory network is not only related to auditory perception, but also with other higher cognitive functions. This maybe due to the auditory network being involved in the complicated brain functions related to language (79), i.e. SMA/cingulate related to articulation (209) and cuneus/lingual gyrus related to rhyme perception (210) and a visual image creation (211).

Higher order networks: The regions in the attention network are related to modulation of attention and working memory (212). The network pattern is similar to those of adults (37, 79, 201, 206, 212, 213), but our regions are of a larger area. For instance, the whole occipital area is involved in the network while this is not seen in the attention network of adults.

Using the operculum as the seed, the executive control network involve mainly the SMA/ACC region, inferior frontal and insula region. This result is similar to that in (186, 203, 206). The ventral frontal region is related to response suppression (214), while the ACC in processing errors and conflict (215, 216, 217). The dorsal ACC and orbital fronto-insula are also activate in response to pain (218), metabolic stress, hunger, or pleasurable touch (219), uncertainty, and social rejection (220).

Default Mode Network: Similar components were obtained for the default mode network for all three seeds in LP, PCC, and MPFC, which are similar to the DMN found in adults (37, 206, 221). Recent developmental studies have found that a primitive DMN can be identified in two-week old infants and it would be more evident as the children are getting older (188). The finding is consistent with this trajectory. This network is related to self-referential mentalizing and social cognition.

From the networks we can see that, the correlation of MPFC with PCC and LP are weak, which is consistent with the findings by Fair et al. (81) and Supekar et al. (222). When studies found stronger correlation between PCC and MPFC in the adults (81, 222), they claim that the change may be due to the maturation of myelination continuing into young adulthood (223). On the other hand, although the components of the DMN in children are the same as those of the adults, the spatial extent of each component is higher. This is in agreement with the idea that children employ both a larger area of cortex and a wider range of interactions of brain regions that include and extend beyond those used in adults (224).

6.5 Conclusion

In summary, we identified the primary, higher order networks and default mode network in 6-year-old children. The primary visual and somatomotor networks are similar to those in infants and young adults (62). The primary auditory, attention, executive control networks in six-year-old children are more widespread when compared to those in young adults (79, 206). DMN in six-year-old children is in the similar pattern as shown in adults (81) but the connectivity strength of vMPFC and PCC may be weaker than that of adults (81). This study suggests that intrinsic functional networks of the brain are formed with well-developed visual and somatomotor networks but developing auditory, attention, executive networks, and DMN at six years of age.

7

Rapidly Developing Functional Circuits and Their Relation with Executive Functions in Early Childhood

As seen in the previous chapter, the functional connectivities in 6-year-old children are formed with developing high order functional networks and default mode network. To understand the functional connectivity development during early childhood, we now study the functional connectivity changes for subjects between 6 and 10 years old and their relationship with cognitive performance. This study also demonstrates the use of the MM-LDDMM method as the statistical basis for the analysis.

7.1 Introduction

Understanding the functional development of human brain is critical for getting profound insight into brain functions and organization with age increase as well as for investigating disorders such as attention deficit hyperactivity disorder (ADHD), Autism Spectrum Disorder (ASD), and Turner syndrome (TS), where normal developmental processes are disrupted. Furthermore, understanding the functional development in the early childhood is important for us to better understand disordered developments as many neurodevelopmental disorders have their origins in infancy or during childhood. Early childhood is a critical period when significant changes occur in brain structures and their functional activations ((225, 226, 227), for reviews). These changes could be reflected through increased cognitive abilities in executive functions such as sustained attention, response inhibition, and memory. These cognitive development has been shown with both positive and negative relationships with the executive functional activation changes from children to adults in different task-related studies (151, 176, 228, 229, 230, 231). In spite of the evidence from these studies for brain activation pattern development, the functional connectivity trajectory and its relationship with executive functions during early childhood is not well understood.

A lot of studies have shown significant changes in both structures and functional activities in brain development and their relationship with cognitive performance ((229), for a review). In general, the brain structures showed significant changes in the regions related to high order cognitive functions during early childhood. For instance, with age increase, cortical thinning was most prominent in the occipital, parietal and frontal lobes for children of ages 5 to 11 (232) or 6 to 10 (233). While fMRI studies have shown that these regions are involved in high order cognitive processes such as attention, response inhibition and working memory (234, 235, 236, 237, 238, 239), developmental fMRI studies also reported significant changes in their functional activations during cognitive task performance for subjects from early childhood to adolescence (151, 176, 177, 228, 229, 230, 231, 238, 240, 241, 242, 243). For example, both the frontal and parietal regions showed higher activation in working memory task (176) and lower activation in attention task (228) for adolescents around age 20 than children around age 10 with improved performance. Both progressive and regressive age related activation changes were thought to shift from diffuse to focal, fine-tuned systems as synapses eliminates and efficiency for synaptic connection improves (229, 230, 244). Nevertheless, some other studies (231) also suggested the recruitment of a wider distributed attention network from ages 8 to 27. Thus, the relationship between functional development and cognitive development from children to adults is very complex.

As mentioned earlier, while these studies showed the functional activity changes in the regions involved in executive functions for subjects in a relative large age range, little is known about their functional connectivity trajectory during early childhood and its relationship with executive functions. Based on the finding that even the narrow one-year interval was characterized by significant arithmetic task-related changes in brain response and connectivity for children between 7 and 9 years (243), we would predict significant developmental changes during early childhood between 6 and 10 years old, especially for the executive functional networks. As many neurodevelopmental disorders have their origins in infancy or during childhood, knowledge about the normal developmental trajectory in this period will enable us to better understand any disordered developments and evaluate therapeutic interventions designed to help place children back onto the normal track (227).

Subjects in their early childhood may not be able to perform tasks well in a scanner, and as an advantage, resting state fMRI (rsfMRI) provides a welcomed alternative for the study of functional connectivity changes, without requiring the participants to perform any specific task. Using rsfMRI, researchers found different functional networks such as the motor (22), attention (201), cognitive control (245) and memory networks (179) which were originally found to be engaged in cognitive tasks, and the default mode network which was present in task free status (187). Based on seed correlation, they found both a segregation of local and integration of distal functional connectivity development involved in attention and cognitive control (174, 186) and the default network (39) from early childhood to young adults. Similar result was found for functional brain network development using graph theoretical approach (28, 42, 72, 174, 186, 246). RsfMRI, therefore, is feasible for studying the functional connectivity change during early childhood. Furthermore, a positive correlation between executive task performance and lateral parietal nodes of the executive-control network connectivity (245) lends further testament to the feasibility of rsfMRI in studying the association between the resting functional connectivity and cognitive performance. However, to our knowledge, the developmental changes in functional connectivity during early childhood and its relationship with the executive functions have not yet been investigated.

The aim of this study is to investigate functional circuits associated with rapidly developing brain structures during the early childhood using both structural MRI and resting-state fMRI, and to understand their relations with cognitive development in attention, response inhibition, spatial and visual memory. We generated seed regions based on structural differences across age and investigated the functional connectivity changes related to those seeds. Next, we detected the connection strengths between seeds and the regions of interest (ROIs) which were significantly functionally connected to the seeds and investigated their relationship with age and cognitive performance. Graph theory was also applied to observe the functional development and its relationship with cognitive performance in the graph network view.

7.2 Materials and Methods

7.2.1 Subjects

A total of fifty-two boys (age range: 72-121 months, average age: 97.06 ± 16.97 months) participated in this study after providing written informed consent from their parents. The study protocol was approved by the Institutional Review Board of National University of Singapore. The children recruited were healthy, ethnically Chinese, Singaporean boys.

7.2.2 Image Acquisition

Structural and functional MR images were acquired using a 3 Tesla Siemens MagnetomTrio system (Siemens, Erlangen, Germany). A high-resolution T1-weighted Magnetization Prepared Rapid Gradient Recalled Echo (MPRAGE) was applied to generate the anatomical image. Volumes consisted of 160 axial slices of 1 *mm* thickness with no gap (voxel size = 1×0.99×0.99; TR = 2 *s*; TE = 2.08 *ms*; flip angle = 9°; FOV = 190×190 *mm*; acquisition matrix = 192×192). To get the functional images in the resting state, subjects were instructed not to think of anything in particular, but just simply to keep their eyes closed. Functional images were acquired using single-shot echo-planar imaging (EPI) with 42 ascending 3 *mm* (no gap) axial slices parallel to the AC-PC plane (voxel size = 2.969×2.969×3; TR =2.4 *s*, TE = 27 *ms*; flip angle = 90°; FOV = 190 *mm*; acquisition matrix = 6464). The functional imaging lasted for 6 minutes and 150 EPI volumes were collected in total.

7.2.3 Structural MRI Data Preprocessing

The structural images were first transformed to the Montreal Neurological Institute (MNI) space by affine registration (195) and then the inner/outer surfaces of individual hemispheres were segmented and reconstructed in Freesurfer (`http://surfer.nmr.mgh.harvard.edu`). Cortical thickness was calculated as the distance from the inner surface to the outer surface at each vertex on the tessellated surface (76). The center of the inner and outer surfaces was then generated as fiducial surface to be geometric representation of the cortex in the rest of the paper. To allow group analysis, we employed a multi-manifold large deformation diffeomorphic metric mapping (MM-LDDMM) algorithm (136) to align the subjects' cortical fiducial surfaces to a healthy 6-year-old boy which was not included in the analysis, while the alignment accuracy of the algorithm has been evaluated in (196). While an average children template is not available yet, we chose this template based on its more generalized sulco-gyral pattern by visually comparing with other subjects. After the surface registration, individual cortical thickness data were transferred to the template surface based on the correspondence derived from the MM-LDDMM and spatially smoothed on it via orthonormal bases of the Laplace-Beltrami operator (equivalent to Gaussian smoothing with a kernel of 20 *mm* FWHM) (113, 144) to reduce noise in thickness measurements (247) and from thickness translation.

7.2.4 Functional MRI Data Preprocessing

The functional data preprocessing follows the same procedure in section 6.2.3.2. In short, the functional scans were preprocessed with slice timing, motion correction, skull stripping, band-pass filtering, grand mean scaling and regression of motion parameters, ventricular and white matter signals. The residual volumes were retained as the resting state signals. Then, to allow surface-based fMRI analysis, the preprocessed fMRI images were aligned to their corresponding structural images and then projected to their corresponding cortical surface. For fMRI group analysis, individual functional data were transferred to the template surface based on the correspondence derived from the previous MM-LDDMM and spatially smoothed on it with a kernel of 12 *mm* FWHM to remove the noise.

7.2.5 Executive Functions

In order to probe the relationship between the functional connectivity and cognitive performance, children received a series of tests of specific executive functions at the time of the MRI scan. These tests, involved in the Cambridge Neuropsychological Test of Automated Battery (CANTAB), included stop-signal test (SST), spatial working memory (SWM), and delayed-matching-to-sample (DMS) task.

Stop signal task (SST). The SST was used to measure response inhibition wherein participants were asked to respond to a stimulus (i.e., the ”go” signal) as quickly as possible, but to withhold responding on trials accompanied by a ”beep” sound (i.e., the stop signal). While latency of response to the ”Go” signal was related to inattention and hyperactivity/impulsivity (248), the mean reaction time (MRT), which was the measure of the speed to respond to the ”go” signal on the screen, was thus examined as reaction measures in response inhibition process. Shorter reaction time meant better attention. In addition, the standard deviation of the reaction time (SDRT) indicated the variation in reaction time over the task and the stop-signal reaction time (SSRT) was the measure of the ability to inhibit the response to the ”go” signal.

Spatial working memory (SWM). The SWM referred to the ability to maintain and manipulate spatial information, and was tested through a self-ordered searching task: six boxes, some of which hide blue tokens, and a column appear on a screen. Participants were instructed to fill the column with tokens without returning to a box from which a token had already been removed. A between-search error was scored when participants returned to a box where a token had already been found and was used as the measure for spatial working memory.

Delayed-matching-to-sample task (DMS). The DMS was a measure of visual memory referred to the ability to briefly maintain visual information. Participants were required to remember an abstract pattern (sample) for 0, 4 or 12 seconds. Participants were then told to select the pattern identical to the sample. The number of correct answers was used as the measure of visual working memory. The more the correct answers the participants got, the better memory performance they had. Analyses of all time delay trials were reported.

7.2.6 Statistical Analysis

Anatomical Statistical analysis: Age related changes in cortical thickness across the whole subjects were analyzed at each vertex on the template surface using a linear regression model with children’s ages in months as a continuous variable. We did not include total intracranial volume as a covariate, as cortical thickness and brain volume are poorly correlated (249, 250). For visualization, the t-statistical maps were generated on the smoothed surface template and thresholded at an uncorrected significance level of $p < 0.01$. We set a cluster size threshold at 695 mm^2, corresponding to a corrected significance level of $p < 0.05$.

Functional Statistical analysis: To investigate the functional connectivity related to the region with rapid structural changes in early childhood, seed ROIs were selected from the clusters which showed significant cortical changes across age from our thickness statistical analysis. After selecting a one-vertex seed-point with the peak t-value in each cluster on the thickness statistical map, the final seed ROIs were generated as a 6 mm square region centered on the seed-point within the clusters. Based on these seed ROIs, functional networks were examined using a seed-based correlation method. The average time series of each seed were correlated with all the vertices on bilateral surfaces to get the functional correlations for each subject. Correlation maps were converted to z maps using Fisher’s r-to-z transformation (205) so that the distribution of the correlations can be normalized.

The group functional connectivity maps related to the seed ROIs across all subjects were evaluated based on one sample t-test. For visualization, the t-statistical maps were generated on the smoothed surface template and thresholded at an uncorrected significance level of $p < 0.001$ with a cluster size threshold at 121 mm^2, corresponding to a corrected significance level of $p < 0.05$.

Relation between functional connectivity and age/cognitive performance: The clusters from the functional connectivity maps were taken as mask ROIs related to each seed network. To study the functional change of each mask ROI, we calculated connection strength as the correlation between average time series of each seed and their related mask ROIs for each subject. Then, a regression analysis revealing the connection strength changes with age were performed. In addition, for those connections changing significantly with age, the regression analyses of the cognitive performance over the connection strengths were performed. To link the structural change with the functional connection strength change with cognitive performance, the regression of the cognitive performance over the thickness was also performed. Before all the analyses related to cognitive performance were done, the association between cognitive performance and age was assessed using linear regression with age as main factor to assure the existence of the age effects age on cognitive performance.

Relation between graph properties and age/cognitive performance: Except for the study of the relationship between connection strength and age/cognitive performance, we also investigated the functional change in the graph network view. A graph matrix was consisted of nodes and edges. For our graph, the aforementioned mask ROIs from each connectivity map were taken as the node and the correlations between mask ROIs over their mean BOLD time series were the edges. The graph was constructed for each subject and each seed related network. Using weighted graph matrices with non-negative correlations (70) and the matlab toolbox for graph property calculation (`http://www.brain-connectivity-toolbox.net`), we calculated several commonly used graph properties, including the global properties, like characteristic path length (67, 251) and global efficiency (67), and the local properties, such as the clustering coefficient, and betweenness centrality of node and edge (68, 252). Both the characteristic path length and global efficiency measured how efficiently the network is to exchange the information at the global level (67). The clustering coefficient measured the extent of local inter-connectivity of a network. On the other hand, the betweenness centrality of a node or an edge measured the number of the shortest paths between pairs of other nodes in the network pass through it. A node or an edge with high centrality was thus important

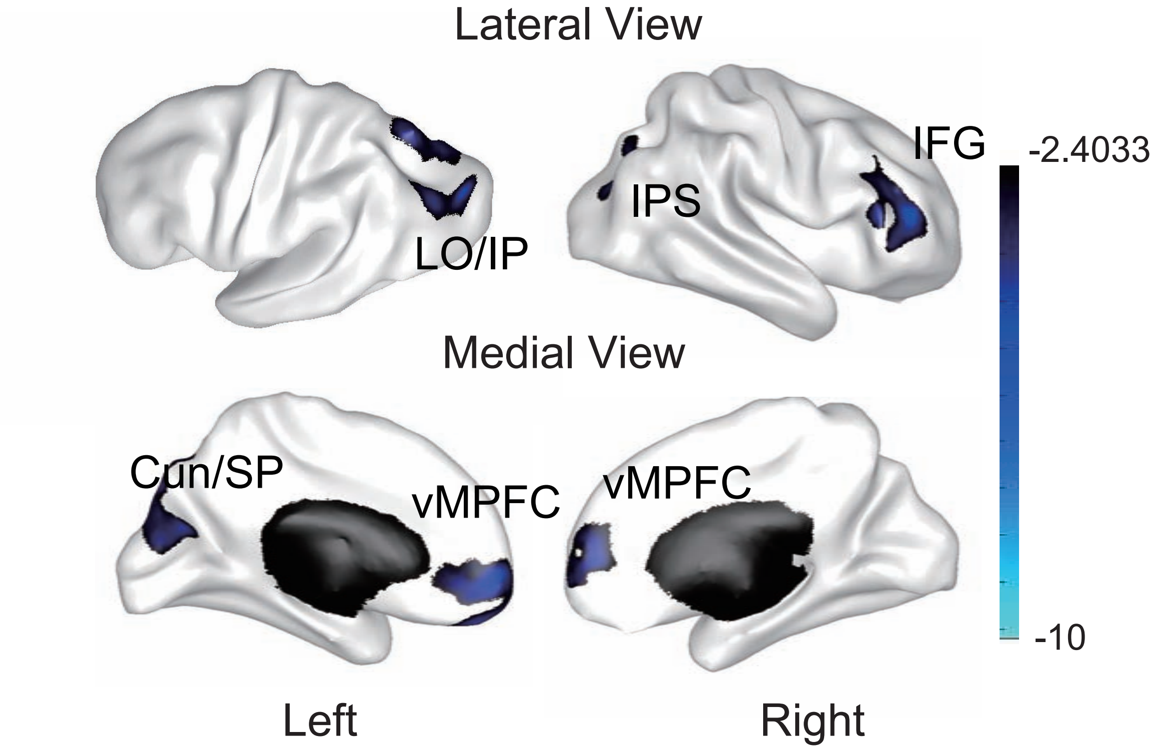

Figure 7.1: Cortical thickness of significantly thinning with age is shown on the smoothed template surfaces in lateral and medial views (vertex level p < 0.01; cluster level p < 0.05). Left column is for the left hemisphere and right column row is for the right hemisphere. The color bar indicates t-scores for the age effects on cortical thinning.

for efficient communication. A detailed description of the properties was in section 2.3.3.3. For each property, the regression analysis with age was performed to show the age effects on it. For those properties with significantly age-related changes, the relationship between them cognitive performance measures was detected for further analysis.

7.3 Results

Several cortical areas showed significant thickness changes over age (Figure 7.1). Significant thinning was observed in the left cuneus/superior parietal (Cun/SP) and lateral occipital/ inferior parietal (LO/IP), right intraparietal sulcus (IPS), right inferior frontal gyrus (IFG) and bilateral ventral medial prefrontal cortex (vMPFC) in the frontal lobe.

With the regions showing significant cortical changes as seeds, the functional connectivity maps presented different patterns which are related to visual, high order cognitive and the default mode networks. The correlated functional connectivity maps across subjects were shown in Figure 7.2, while the seeds were shown on the smoothed template surface for visualization (Figure 7.2, blue dots on the surface). Upper row of panel A in Figure 7.2 shows left Cun/SP seed correlation mainly involved visual-related regions. Across all fifty-two subjects, significant correlation was found in bilateral lateral and medial occipital lobe, posterior cingulate cortex (PCC)/precuneus, superior temporal gyrus (STG), left middle temporal gyrus (MTG), rostral anterior cingulate (RAC), medial prefrontal cortex (MPFC) and right PreCentral Gyrus (PreCeG). The other two posterior seeds, left LO/IP and IPS, were similar to each other and consistent with the attention network of children (79). Left LO/IP seed was significantly correlated with bilateral lateral and medial occipital/parietal (Occi/Pariet) and left superior temporal sulcus (STS) regions (Figure 7.2, upper row of panel B). Similarly, right IPS seed was positively correlated with bilateral Occi/Pariet regions, right supramarginal (SM) and inferior frontal gyrus (IFG) (Figure 7.2, upper row of panel C).

The significant correlations related to lateral and medial frontal seeds were mainly involved in executive functions and default mode networks respectively. Right IFG seed was significantly correlated with bilateral IFG, insula, intraparietal sulci/posterior central sulcus (IPS/PoCeS), inferior temporal gyri (ITG), medial frontal cortex (MFC), right ACC and middle frontal gyrus (MFG) (Figure 7.2, upper row of panel D). This network was related to both executive control (230, 245, 253) and working memory (194, 254). Bilateral vMPFC seeds were both positively correlated with bilateral MPFC, PreCuneus and PCC. In addition, while left vMPFC seed was correlated with left MTG, right temporal pole (TP), right vMPFC was correlated with bilateral MTG and supramarginal (SM) cortex (Figure 7.2, upper row of panels E and F), which was in accordance with the default mode network found in subjects in early childhood (79, 180).

With the functional connectivity ROIs as masks, significant age effects were found for the connection strength between the frontal seeds and mask ROIs. The relation between the connection strengths and age were given in the lower row of Figure 7.2 for each connection. The red line indicated positive relationship between that connection with age while the black line indicated negative relationship. The thicker line represented significant relationship between the connection strength and age. The figure showed that for the frontal seeds (IFG, LvMPFC, and RvMPFC), they had positive relations between connection strength of seed ROI-proximal mask ROIs and age, negative relations between connection strength of seed ROI-distal mask ROIs and age. There was no clear trend for the seeds in the posterior region of the brain. Sig-

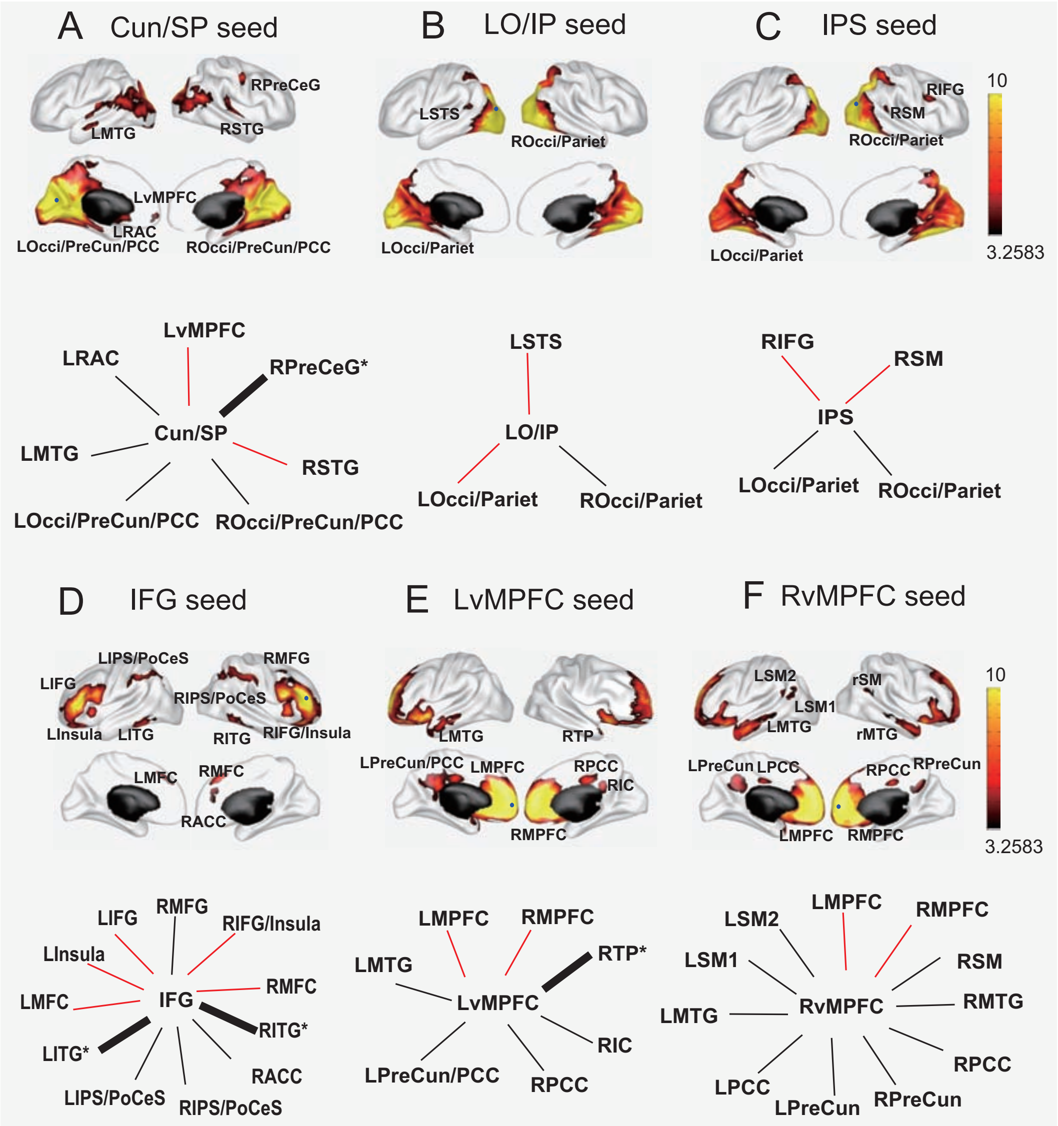

Figure 7.2: The functional connectivity maps for each seed across all subjects (upper row of each panel) are shown on the smoothed template surface (vertex level $p < 0.001$; cluster level $p < 0.05$). The seed ROIs are indicated by blue dots on the surface and the color bar indicates t-scores for group statistics. The regression effects for age on the connection strength of seed ROI and mask ROIs are shown in the lower row of each panel. The negative relationships are present in black line while the positive ones are in red line. The thicker line represents the connection strength over age is significant. Connectivities of Cun/SP-RPreCeG, IFG-LITG, IFG-RITG, and LvMPFC-RTP are significantly decreasing with age.

Note: MTG- middle temporal gyrus; STG- superior temporal gyrus; PreCeG- precentral gyrus; Occi/Pariet- occipital/parietal lobe; RAC- rostral anterior cingulate; vMPFC- ventral medial prefrontal cortex; STS- superior temporal sulcus; IFG- inferior frontal gyrus; SM- supramarginal; insula- insula; MFG- middle frontal gyrus; ITG- inferior temporal gyrus; IPS/PoCeS- intraparietal sulcus/postcentral sulcus; ACC- anterior cingulate cortex; MFC- medial frontal cortex; TP- temporal pole; PCC- posterior cingulate cortex; MPFC- medial prefrontal cortex; PreCun- Precuneus; IC- isthmus cingulate; SM1- anterior part of supramarginal; SM2- posterior part of supramarginal.

Table 7.1: The regression coefficients for effects of seed thickness and connection strength of seed ROI-mask ROI on cognition of subjects.

Cognitive measures	seed cortical thickness					
	Cun/SP	LO/IP	IPS	IFG	LvMPFC	RvMPFC
SST MRT	216.10	**340.67*****	**209.80***	165.43	**196.58***	**175.29****
SST SDRT	154.15	**279.16*****	115.94	81.23	104.96	**122.94****
SST SSRT	132.33*	**99.37***	20.48	57.67	**78.25***	44.86
SWM Error	**11.79***	**9.16***	**8.46***	**9.40****	6.01	3.28
DMS correct answers	**-5.31****	**-3.73****	-2.23	-1.71	**-3.04***	**-1.91***

Cognitive measures	seed ROI-mask ROI functional connection strength			
	Cun/SP-RPreCeG	LvMPFC-RTP	IFG-LITG	IFG-RITG
SST MRT	63.56	**237.75***	129.05	53.47
SST SDRT	66.60	**169.09***	101.04	23.47
SST SSRT	43.65	73.46	**77.90***	60.15
SWM Error	**15.55****	3.51	2.85	**6.76***
DMS correct answers	**-5.83****	-1.30	-0.49	**-3.14****

Note: SST = stop-signal task; MRT = mean reaction time; SDRT= standard deviation of reaction times; SSRT= stop signal reaction time; SWM = spatial working memory task; DMS = delayed-matching-to-sample task.
*p < 0.05. **p < 0.01. ***p < 0.001.

nificantly negative relationship between connection strength of seed ROI-distal mask ROIs and age were found for Cun/SP-RPoCeG, LvMPFC-RTP, IFG-LITG and IFG-RITG (p < 0.05).

The regression analysis of cognitive measures over age confirmed that the older subjects had improved performance related to attention, response inhibition and memory functions. To be specific, MRT (p=0.0250), SDRT (p=0.0018), and SSRT (p=0.0349), errors made in SWM tasks (p < 0.0010)were significantly negatively correlated with age, which indicated older subjects showed faster reaction and better response inhibition over signal and better spatial working memory. In contrast, correct answers of DMS (p < 0.0010) were positively correlated with age. Thus the older the subjects were, the better their memory for visual information was.

Cortical thinning in the seeds were related to improved cognitive performance and the connection strengths which decreased significantly with age were found related to different executive functions. The regression of the cognitive performance over the cortical thickness in the seeds were shown in the upper table of Table 7.1, which showed that cortical thinning in the frontal, occipital and parietal regions were related to improved cognitive performance of attention, response inhibition and memory. In addition, for those seed ROI-mask ROI connection strengths being significantly decreasing with age (lower row of Figure 7.2), the relationships between them with cognitive performance were also investigated (lower table of Table 7.1). We found that these long seed ROI-mask ROI connections were also significantly correlated with cognitive performance.

Attention: Thickness of LO/IP, IPS, bilateral vMPFC were found to be significantly positively related to mean reaction time (MRT), which suggested shorter reaction on signals was related to cortical thinning in parietal and vMPFC seeds. And the connection strength of LvMPFC-RTP was positively correlated with MRT (beta=237.7541, $p < 0.05$) and SDRT (beta=169.0855, $p < 0.05$), which indicated when the connection strength of LvMPFC-RTP was low, the boys showed a shorter reaction time and smaller variation on reaction time over the task.

Response inhibition: Thickness of LO/IP, RvMPFC were found to be significantly positively related to SDRT and that of Cun/SP, LO/IP, LvMPFC related to SSRT, which indicated better inhibition ability was related to cortical thinning in occipital, parietal and vMPFC seeds. The connection strength of IFG-LITG was significantly positively correlated with SSRT (beta=77.8980, $p < 0.05$) which indicated that the lower connection strength was corresponding to better ability for maintaining execution and inhibition process.

Memory: Thickness of Cun/SP, LO/IP, IPS and IFG were found to be significantly positively related to errors made in SWM task and that of Cun/SP, LO/IP, bilateral vMPFC were related to answers for DMS. This indicated cortical thinning in posterior seeds were related to better performance in both visual and spatial memory, while that of lateral frontal seed related to better spatial memory, and medial frontal seeds related to better visual memory. Both the connection strengths of Cun/SP-RPoCeG and IFG-RITG were positively related to the error of SWM task ($p < 0.05$) and negatively related to the correct answers for DMS ($p < 0.01$) significantly. This implied that when the connection strengths of Cun/SP-RPoCeG and IFG-RITG were low, the participants had better memory for visual and spatial information.

Graph analyses showed no significant age-related changes of global properties and clustering coefficient (Table 7.2), while betweenness centrality showed significant changes in the

Table 7.2: The regression coefficients ($\times 10^{-2}$) for effects of age on graph properties of each seed network.

Seed-Network	Cun/SP	LO/IP	IPS	IFG	LvMPFC	RvMPFC
Cp	-0.06	-0.07	0.03	-0.07	-0.13	-0.23
Lp	-0.07	0.06	-0.08	0.06	0.14	-0.22
Eglo	119.77	-0.61	-2.62	1.68	961.73	11.66

Note: Cp- clustering coefficient; Lp: characteristic path length; Eglo: Global efficiency. Cun/SP- cuneus/superior parietal; LO/IP- lateral occipital/ inferior parietal; IPS- intraparietal sulcus; IFG- inferior frontal gyrus; vMPFC- ventral medial prefrontal cortex.
*$p < 0.05$.

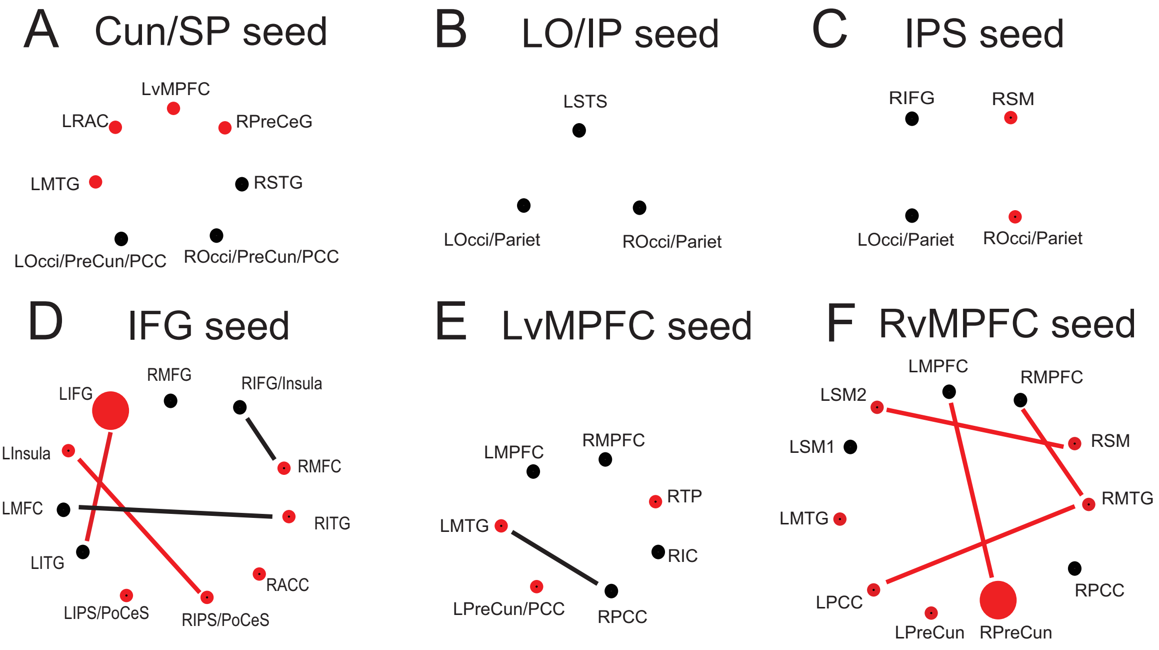

Figure 7.3: The regression effects for age on the Node betweenness centrality (N_{bc}) of mask ROIs and Edge betweenness centrality (E_{bc}) of inter-mask ROI connections. For each network, the dots represent the nodes, which are the mask ROIs in each connectivity map (see upper row of each panel in Figure 7.2), and the lines between nodes are the edges, which are the connections between mask ROIs. The black dots represent the negative relation between nodes and age, while the red ones represent the positive relationship. The big dots indicate significant relationship with age. To simplify the figure, only the inter-mask ROI connections with significant changes in E_{bc} over age are shown. Black line represents the negative relationship between E_{bc} of that connection and age while red line represents positive relationship. For abbreviations please refer to Note of Figure 7.2.

network related to frontal seeds. Figure 7.3 showed the regression effects of Node betweenness centrality (N_{bc}) of mask ROIs and Edge betweenness centrality (E_{bc}) of inter-mask ROI connections over age. For each network, the dots represented the nodes, which were the mask ROIs in each connectivity map (see upper row of each panel in Figure 7.2), and the lines between nodes were the edges, which were the connections between mask ROIs. The black dots represented the negative relation between nodes and age, while the red ones represented the positive relationship. The big dots indicated significant relationship with age. ROIs with high N_{bc} were important in managing the flow of information across the network because they were more likely to reside on the shortest path between other regions. We found that N_{bc} of left IFG (LIFG) in IFG network and right precuneus (RPreCun) in RvMPFC network increased significantly with age (bigger dot in Figure 7.3). This indicated that for the IFG network, left IFG became more important in managing the flow of information across the network in older children. Likewise, for the RvMPFC network, right precuneus was more important in older children.

Similarly to N_{bc}, E_{bc} identified critical connections in each functional network. Network connections with high E_{bc} were more likely to reside on the shortest connection between any 2 regions. The edges with significant changes over age were shown in Figure 7.3. To simplify the figure, only the inter-mask ROI connections with significant changes in E_{bc} over age were shown. Black line represented the negative relationship between E_{bc} of that connection and age while red line represented positive relationship. Connections with significant changes of E_{bc} over age were all in the network related to frontal seeds. For the IFG network, E_{bc}s of LInsula-RIPS/PoCeS and LIFG-LITG were significantly increasing with age and those of LMFC-RITG and RIFG/Insula-RMFC were significantly decreasing with age, which suggested the two connections' importance changed differently over age. For the LvMPFC network, significant decrease of E_{bc} with age was found in LMTG-RPCC, suggesting that this connection in the LvMPFC network became less important in older subjects. And for the RvMPFC network, significant increase of E_{bc} with age was found in RPrecun-LMPFC, LPCC-RMTG, RMPFC-RMTG, and LSM2-RSM. This indicated that these connections of the RvMPFC network became more important in older subjects.

The influence of the N_{bc} and E_{bc} with significant age related changes over cognitive performance was detected and we found improvement of response inhibition and memory function being related to changes of the betweenness centrality. There were no significant changes over cognitive performance for the N_{bc} of LIFG in IFG network and RPreCun in RvMPFC default

Table 7.3: The regression coefficients for effects of graph properties of each seed network on cognition of subjects.

Cognitive measures	LvMPFC	RIFG				RvMPFC			
	LMTG-RPCC	LIFG-LITG	LInsula-RIPS/PoCeS	LMFC-RITG	RIFG/Insula-RMFC	LPCC-RMTG	RMPFC-RMTG	LMPFC-RPreCun	LSM2-RSM
SST MRT	7.32	-0.66	-12.26	7.12	6.32	-5.58	-10.28	-13.81	-16.82
SST SDRT	7.46	-0.34	-6.85	7.54	3.19	-6.23	-9.48	-8.84	1.17
SST SSRT	0.01	-0.94	1.27	2.15	3.49	**-5.52***	-4.32	-5.80	-6.38
SWM Error	0.60	-0.37	0.02	0.04	**0.87***	-0.33	**-0.78***	-0.49	-0.33
DMS correct answers	**-0.34***	0.11	0.10	-0.02	**-0.32***	0.18	0.13	-0.09	0.05

Note: For abbreviations please refer to Note of Figure 7.2.
*$p < 0.05$.

network. The regression coefficients of the cognitive performance over the E_{bc} with significant age-related changes were shown in Table 7.3.

Response inhibition: We found that the E_{bc} of LPCC-RMTG in RvMPFC network (beta=-5.5200, $p < 0.05$) were negatively related to the stop signal reaction time significantly. This indicated that the larger the E_{bc}, the shorter the reaction time.

Memory: The E_{bc} of RMTG-RMPFC in RvMPFC network (beta=-0.7759, $p < 0.05$) were negatively and that of RIFG/Insula-RMFC in IFG network (beta=0.8716, $p < 0.05$) were positively related to the errors made in SWM tasks significantly. As E_{bc} of RMTG-RMPFC was increasing with age and RIFG/Insula-RMFC was decreasing with age, the result suggested that with age increase, the changes of E_{bc} were related to better spatial memory performance. In addition, we found that the E_{bc} of LMTG-RPCC in LvMPFC network (beta=-0.3371, $p < 0.05$) and that of RIFG/Insula-RMFC in IFG network (beta=-0.3126, $p < 0.05$) were negatively related to the correct answers for DMS significantly. This suggested that smaller E_{bc} of the connections was related to better visual memory.

7.4 Discussion

This is the first study to examine the functional connectivity associated with developing brain structures during early childhood and its relationship with cognitive performance. We generated seed regions in occipital, parietal and frontal cortex based on cortical thinning over age and found that functional connectivity between seed ROIs and distal connected regions (mask ROIs) was reduced over age and related with improved cognitive performance in attention, response inhibition and memory. In addition, based on graph analysis, both progressive and regressive changes of the importance (in terms of betweenness centrality) of regions and inter-regional connections were found in the frontal networks with age increase. These changes were related to cognition improvement in response inhibition and memory functions. Thus, with the functional seed correlation and graph theoretical approach, we found that during early development, both regional activation and functional interactions between regions, especially for those in frontal networks, are changing prominently, which can be partly due to structural changes and has important relationship with cognitive performance for executive functions. These findings provide new information about normal neurodevelopmental trajectories during early childhood within a small age range.

Structural Maturation and its relation with cognitive performance: In agreement with previous studies, our results revealed that older children showed better performance in attention, response inhibition and memory functions, hence confirming the protracted developmental trajectory of high order functions (174, 255). The findings of significant cortical thinning in occipital, parietal and frontal regions were consistent with a study by (233), which reported the trajectory of normal brain development between ages 6 to 10 years. Similarly, the relation of cortical thinning in these regions with improved cognitive performance has also been repeatedly demonstrated in many studies (232, 255, 256, 257). Since cortical thinning is related to cortical maturation in the form of synaptic pruning, proliferation of myelin (232), trophic glial and vascular changes, and possible cell shrinkage (258), cognitive maturation may reflect the cortical maturation process to some extent.

Functional connectivity development and its relationship with cognitive performance: The reported functional results support the idea that high order functions develop with a protracted trajectory. During early childhood, decreases of long distance connection strength between seed ROI and mask ROI were associated with cognitive improvement. Improved spatial and visual memory was related to decreased connection strength of Cun/SP-RPreCeG, and RIFG-RITG. Likewise, shorter SSRT was found to be related to weaker RIFG-LITG connection strength in the control network. These results were consistent with the previous findings where lateral frontal and parietal regions were involved in memory and control functions (176, 194, 241, 245, 253, 254). Lastly, shorter reaction time and smaller SDRT were associated with weaker LvMPFC-RTP connection in the default mode network. This is in agreement with the finding by (259) that the components in default network are not only activated in task free status, but also related to monitor cognitive performance. The functional connection decrease associated with an improvement in cognitive performance may be partly due to structural changes. Significantly, positive correlation was found between the Cun/SP-RPreCeG connection strength and Cun/SP thickness (beta=0.3201, $p < 0.05$), and LvMPFC-RTP connection strength and LvMPFC thickness (beta=0.3164, $p < 0.01$). Thus, the aforementioned long path connection decrease, significantly related to seed cortical thinning, may be caused by synaptic pruning and myelination for more efficient processing (151, 257).

In general, our results show that in frontal seeds, age is positively related to seed ROI-proximal mask ROIs connection but negatively related to seed ROI-distal mask ROIs connection. However, different from our result, previous literature reported both a segregation of local functional connectivity and integration of distal functional connectivity during normal functional development from subjects in early childhood to young adults, in both the attention and cognitive control network (174, 186) and the default network (39). This discrepancy between our result and current literature may suggest that this connection strength is developing nonlinearly as high order functional networks have a protracted developmental trajectory. Particularly for the long range paths, the trajectory maybe following a U shape curve from early childhood to adults.

Importance of Nodes (mask ROIs) and edges (inter-mask ROIs) of networks change over age and its relationship with cognitive performance: Mask ROIs and inter-mask ROI connections with prominent change across age were found mainly in frontal seed networks by graph theoretical analysis. More specifically, LIFG ROI in IFG network and RPreCun ROI in RvMPFC network showed increasing importance across age, although they were not significantly related to cognitive performance. Thus, left IFG is, significantly, of increasing importance in information flow in the control network. While previous studies found reduced lateralization of activations in children compared to adults (260, 261), our results may suggest that the laterality reduces during early childhood and then increases until adults (262, 263). The Right Precuneus becoming increasingly important for information transfer in the default mode network is consistent with previous results of increasing involvement of Precuneus in the default network over development (39, 42).

Prominent changes of connection between ROIs were only found in frontal networks, further suggesting that connectivity related to frontal regions were under rapid development during early childhood. Long range inter-mask ROI (LIFG-LITG and LInsula-RIPS/PoCeS) connections showed increased importance in information flow over development in the IFG control network. On the other hand, short range RIFG/Insula-RMFC and long range LMFC-RITG connections were decreasingly important with age in the control network. Thus, the importance of the long range inter-mask ROI connection are changing both progressively and regressively, although only prominent decreases with age were found in our function connection between seed with the distal mask ROIs. These facts suggest that during early childhood, the control network undergoes complex functional changes that are generally related to improved cognitive performance. We found that the decreased E_{bc} of RIFG/Insula-RMFC is related to improved visual and spatial memory functions. As the lateral frontal and parietal regions are the key regions related to memory functions (176, 194, 254) while MFC is mainly related to social cognition and mental states representation (264), it is possible that, MFC, which is not critically related to memory functions, will be less involved with increasing age.

For the LvMPFC related default network, LMTG-RPCC connection showed decreasing importance in information flow over development, which was related to improvement in visual memory performance. For the RvMPFC related default network, significant positive changes in the connections were observed during development, of which the RPMFC-RMTG and LPCC-RMTG connections were related to improved spatial memory and response inhibition respectively. The different trends for the connection change in the two networks are related to different functions. As mentioned by Hampson et al., (259), connectivity between components of the default network, especially the PCC and MPFC, exist not only in resting state but also during working memory task. In addition, under these two conditions, positive correlations between connection strength and working memory performance were also found. Thus, the LMTG-RPCC and RMPFC-RMTG connections in the default mode network may function to facilitate or monitor memory performance. Similarly, increased E_{bc} of LPCC-RMTG connection in the default network related to improved response inhibition ability may also be monitoring the executive control function.

These results are based on the resting state fMRI whose role in investigating brain functional connectivities should be appreciated. However, we may still take note that this does not mean we should nullify the use of task fMRI. Resting state fMRI functional network can only tell which regions are highly functionally connected. It can not tell whether these exactly same regions would be activated during some specific task, which can be fulfilled by task-related fMRI. Thus, with both resting state fMRI and task-related fMRI, a clearer view related to brain function can be generated in the future.

In conclusion, our results demonstrate the relationship between protracted functional development and executive functions during early childhood. For this same time period, our findings suggest that, functional connectivity does not develop in the general way of ”segregation of local connectivity and integration of distal connectivity”. Instead, long range connectivity decreases for more efficient processing of cognitive functions. For the information transfer, progressive and regressive changes of the regions related to frontal networks were present for improvement of cognitive performance. These changes are partly related to cortical thinning caused by synaptic pruning and myelination during development (255).

8

Conclusions

8.1 Conclusions

In this thesis we proposed a registration method which can well control both global (cortical surfaces) and local (curves) information of the cortical surfaces in their own coordinates, and based on this method, we investigated both structural and functional studies which are useful and informative for future related studies.

To get reliable structural and functional group analytical results, accurate brain registration is necessary. We proposed a registration method, multi-manifold large deformation diffeomorphic metric mapping (MM-LDDMM), for deforming the cortical hemispherical surfaces by controlling both global (cortical surfaces) and local (curves) information in their own coordinates. The MM-LDDMM framework was introduced in chapter 3. Compared to the LDDMM-curve and LDDMM-surface approaches that only consider either local or global information for deformation, our method showed improvement registration accuracy. Moreover, our MM-LDDMM could better align both the local regions (curves and ROIs) and cortical shape patterns (e.g. curvature) with comparison to the previous registration methods in the LDDMM framework and the popular spherical registrations implemented in CARET and FreeSurfer softwares, as MM-LDDMM took both global and local information into consideration during alignment. In addition, we conducted simulation experiment revealing that the MM-LDDMM mapping had less local and global deformation errors than the CARET and FreeSurfer mappings did.

Having developed our registration method, we subsequently adopted it to both structural and functional studies which would help future related studies. As is well known, the brain registration and the statistical analysis for functional study are dependent on the template. Due to large variations in brain anatomical shape across human populations, a suitable template which can represent morphology and individual variability would show less bias during the brain registration. While the average template generation is based on registration, only good registration would give representative and meaningful new template over a population. With our MM-LDDMM registration, we generated an average template for a sample of subjects including young healthy adults to the healthy elders as well as the dementia patients shown in Chapter 5. MM-LDDMM provided a simple way to compute the average of the anatomical deformations via the average of the initial momenta and then constructed average geodesic in a metric shape space through the geodesic shooting, as the MM-LDDMM algorithm was developed based on a conservation law of momentum for the geodesics of diffeomorphic flow, the initial momenta obtained from it characterized non-linear shape variations across anatomies in a linear space. Our newly generated template for the cortical surface maintained the detailed sulco-gyral pattern but this was not limited to major deep sulci. It was representative for the population in terms of its metric distance to each individual subject in the population. This template would be useful in the shape study on cortical structures in a variety of neurodegenerative diseases and healthy aging.

Other than structural studies, good brain registration is also required in functional studies, to locate which brain region is related to the specific function. As our MM-LDDMM registration can provide good registration in both local region and global shape pattern, fMRI analysis based on our method would be meaningful in functional location identification. While the functional connectivity of the brain in the early childhood was not clear but very important for our understanding of the normal brain development and functional changes in patients with neurodegenerative diseases, we conducted resting state functional MRI analyses based on MM-LDDMM algorithm presented in Chapters 6 and 7. We analyzed the resting state functional connectivity of 6-year-old children's brain based on the cortical surface model. Our large scale study identified the primary, higher order networks and default mode network (DMN) in 6-year-old children, which filled the knowledge gap for our understanding of the functional connectivity from in early childhood. While the primary visual and somatomotor networks were similar to those in infants and young adults, the primary auditory, attention, executive control networks were more widespread when compared to those in young adults. DMN in six-year-old children was in the similar pattern as shown in adults but the connectivity strength of vMPFC and PCC may be weaker than that of adults. Our study suggested that intrinsic functional networks of the brain were formed with well-developed visual and somatomotor networks but developing auditory, attention, executive networks, and DMN at six years of age. Moreover, to better understand the functional development during early childhood and its relationship with cognitive development, we also investigated the resting state functional connectivities development between 6 and 10 years old children and examined their relations with cognitive performance by applying this registration algorithm. Using the functional seed correlation method, we found connection between seed regions of interest (ROI) and distal connected ROIs (mask ROIs) were significantly decreasing with age increase and cognition improvement in attention, response inhibition and memory functions. Also, graph analyses revealed significant changes of betweenness centrality for mask ROIs and inter-mask ROI connections in the frontal seeds networks across age, with cognition improvement in response inhibition and memory functions. Thus, our study showed a protracted developmental trajectory for functional circuits, with decreased connectivity related to improved cognitive performance during early childhood. In addition, both progressive and regressive changes of the importance of specific inter-mask ROI connections in the frontal networks were associated with cognitive performance improvement during early childhood. These findings presented that, during early development, both regional activation and functional interactions between regions, especially for those in frontal networks, were changing prominently, which can be partly due to structural changes and has important relationship with cognitive performance for executive functions. This study provided new information about normal neurodevelopmental trajectories during early childhood, which could enable us to better understand any abnormal developments for those neurodevelopmental disorders.

8.2 Future Directions

Throughout the thesis, we discussed the improvement of the brain registration method and its application in both structural and functional studies. We now draw up the outlines of the future directions of research:

In this thesis, we have proposed the MM-LDDMM registration method which can well align both local regions and global cortical shape, which provides a reliable basis for future structural and functional analysis. While for our method, the curves were semi-automatically tracked on each cortical surface via dynamic programming (141) which need a lot of manual work and was very time consuming, one of the future directions is to incorporate an algorithm to track the curves automatically. There have been several automatic curve extraction algorithms (265, 266, 267, 268), but these algorithms mainly focus on extracting the sulci but not gyri. While we found that the gyri are also important for representing the surface and constraining the registration, algorithms need to be extended in this direction. Another problem is these automatic methods are used to extract the curves without labeling them, which also makes the registration between subjects hard as the registration need to have corresponding curves as objects. Thus, if we can solve the two problems, incorporating the algorithms to extract the sulcal and gyral curves automatically will enhance the robustness of the MM-LDDMM method and also save a lot of time and labor.

We have generated a template which is representative for the adults population including dementia patients. This template serves as a base for our future shape analysis, e.g. thickness changes, on subjects of healthy aging or neurodegenerative diseases. Firstly, we can compare the analytical results generated from average template and single subject template to further prove the usefulness and representativeness of the average template. Secondly, we could define the shape changes of the brain in some specific period of aging and in the patients with specific disease to understand how these changes are related to healthy aging and diseases. Similarly, for different population, different average templates would be needed. As we already have a large set of children data, we also can generate an average template for the early children population, which can be used as the template for other children-related studies.

On the other hand, we have applied the MM-LDDMM algorithm to investigate the resting state functional network in 6-year-old children, as well as the functional development with related to cognitive performance in the early childhood (between 6 and 10 years old). These studies showed us the functional connectivity pattern in a short time period in the early childhood, and the local functional changes related to better cognitive performance in attention, response inhibition and memory functions. As there are rapid structural changes from infants to adults, registration methods only based on either curves or surfaces can not fully capture the global and local changes for brains in these stages. Our MM-LDDMM is more useful in the sense that it incorporates both curves and surfaces to control the registration, so the application of MM-LDDMM for the quantitative comparison between functional connectivity in infants, children and adults will also be valuable for a clearer idea of the functional development from infants to adults. This will be useful as a reference for the researches related to brain diseases, such as Attention Deficit Hyperactivity Disorder(ADHD), Alzheimer’s Disease (AD) and Parkinson’s disease.

Currently our MM-LDDMM registration method is only applied to the cerebral cortex. It also can be used to other brain parts, such as the subcortical regions and the cerebellum. However, no curves may be needed for registration of subcortical regions as their structures are relatively simpler and not in the complex sulco-gyral pattern. Thus, during the registration, the trade-off parameter for curves can be set as 0, which method is called LDDMM-surface mapping method. For cerebellum, it is challenging because the convolutions of the cerebellar cortex are more complex than cerebral cortex. One distinctive aspect of cerebellar surface geometry is that the folds tend to run parallel to one another. One of the challenges would be defining the corresponding curves across subjects. If correct corresponding curves on the cerebellum can be delineated across subjects, MM-LDDMM can be applied for cerebellum and help for the cerebellum-related analysis.

References

[1] Ozcan M., Baumgartner U., Vucurevic G., Stoeter P., and Treede R.-D. **Spatial resolution of fMRI in the human parasylvian cortex: Comparison of somatosensory and auditory activation**. *NeuroImage*, **25**:877–887, 2005. 2, 20, 73

[2] B. Fischl, M.I. Sereno, R.B.H. Tootell, and A.M. Dale. **High-resolution inter-subject averaging and a surface-based coordinate system.** *Hum. Brain Mapp.*, **8**:272–284, 1999b. 2, 19, 20, 21, 27, 28, 40, 41, 42, 49, 73

[3] B. Fischl, N. Rajendran, E. Busa, J. Augustinack, O. Hinds, B.T. Yeo, H. Mohlberg, K. Amunts, and K. Zilles. **Cortical folding patterns and predicting cytoarchitecture**. *Cereb Cortex*, **18**:1973–1980, 2008. 2, 63

[4] A.M. Dale, B. Fischl, and M.I. Sereno. **Cortical surface-based analysis: I. Segmentation and surface reconstruction.** *NeuroImage*, **9**:179–194, 1999. 2, 34, 44

[5] D.C. van Essen. **A population-average, landmark- and surface-based (PALS) atlas of human cerebral cortex.** *NeuroImage*, **28**:635–662, 2005. 2, 21, 27, 40, 41, 67, 70, 71

[6] Yonggang Shi, Paul M. Thompson, Ivo Dinov, Stanley Osher, and Arthur W. Toga. **Direct cortical mapping via solving partial differential equations on implicit surfaces**. *Medical Image Analysis*, **11**:207–223, 2007. 2, 20, 22

[7] Anqi Qiu and Michael I. Miller. **Cortical Hemisphere Registration via Large Deformation Diffeomorphic Metric Curve Mapping**. In *the 10th International Conference on Medical Image Computing and Computer Assisted Intervention*, **10**, pages 186–193, 2007. 2, 24, 25, 27, 28, 37, 40

[8] J. Glaunès, A. Qiu, M. I. Miller, and L. Younes. **Large deformation diffeomorphic metric curve mapping**. *International Journal of Computer Vision*, **80**(3):317–336, 2008. 2, 22, 24, 26, 31, 42, 44, 46

[9] A. Anticevic, D.L. Dierker, S.K. Gillespie, G. Repovs, J.G. Csernansky, D.C. Van Essen, and D.M. Barch. **Comparing surface-based and volume-based analyses of functional neuroimaging data in patients with schizophrenia**. *NeuroImage*, **41**:835–848, 2008. 2, 21, 38, 41, 42, 64, 73, 77

[10] MORRIS MOSCOVITCH and GORDON WINOCUR. **Frontal Lobes, Memory, and Aging**. *Annals of the New York Academy of Sciences*, **769**(1):119–150, 1995. 6

[11] J. M. NIELSEN. **Occipital Lobes, Dreams and Psychosis**. *Journal of Nervous and Mental Disease*, **121**(1):50–52, 1955. 6

[12] Hans Lassmann, Mascha Schmied, Karl Vass, and William F. Hickey. **Bone marrow derived elements and resident microglia in brain inflammation**. *Glia*, **7**(1):19–24, 1993. 7

[13] Arvidsson A., Collin T., Kirik D., Kokaia Z., and Lindvall O. **Neuronal replacement from endogenous precursors in the adult brain after stroke**. *Nature Medicine*, **8**(9):963–970, 2002. 7

[14] Robin L. Brey. **Cigarette smoking and multiple sclerosis (MS): Yet another reason to quit**. *Neurology*, **61**(8):E11–E12, 2003. 7

[15] JAMES A. COOPER, HARVEY J. SAGAR, NIGEL JORDAN, NORMAN S. HARVEY, and EDITH V. SULLIVAN. **COGNITIVE IMPAIRMENT IN EARLY, UNTREATED PARKINSON'S DISEASE AND ITS RELATIONSHIP TO MOTOR DISABILITY**. *Brain*, **114**(5):2095–2122, 1991. 7

[16] Squire LF and Novelline RA. *Squire's fundamentals of radiology*. Harvard University Press, 5 edition, 1997. 8

[17] L Pauling and CD Coryell. **The Magnetic Properties and Structure of Hemoglobin, Oxyhemoglobin and Carbonmonoxyhemoglobin**. *PNAS*, **22**:210–6, 1936. 13

[18] Thulborn KR, Waterton JC, Matthews PM, and Radda GK. **Oxygenation dependence of the transverse relaxation time of water protons in whole blood at high field**. *Biochim. Biophys. Acta*, **714**(2):265–70, 02 1982. 13

[19] J. Belliveau, D. Kennedy, R. McKinstry, B. Buchbinder, R. Weisskoff, M. Cohen, J. Vevea, T. Brady, and B. Rosen. **Functional mapping of the human visual cortex by magnetic resonance imaging.** *Science*, **254**:716–719, June 1991. 13

[20] Roger B. H. Tootell, Nouchine K. Hadjikhani, Wim Vanduffel, Arthur K. Liu, Janine D. Mendola, Martin I. Sereno, and Anders M. Dale. **Functional analysis of primary visual cortex (V1) inhumans**. *Proceedings of the National Academy of Sciences*, **95**(3):811–817, 1998. 13

[21] S.-G. Kim, J. Ashe, A. P. Georgopoulos, H. Merkle, J. M. Ellermann, R. S. Menon, S. Ogawa, and K. Ugurbil. **Functional imaging of human motor cortex at high magnetic field**. *J Neurophysiology*, **69**:297–302, 1993a. 13

[22] B Biswal, FZ Yetkin, VM Haughton, and JS Hyde. **Functional connectivity in the motor cortex of resting human brain using echo-planar MRI**. *Magn Reson Med : ,*, **34**:537–541, 1995. 13, 15, 17, 74, 77, 86

[23] R. M. Hinke, X. Hu, A. E. Stillman, S.-G. Kim, H. Merkle, R. Salmi, and K. Ugurbil. **Functional magnetic resonance imaging of Broca's area during internal speech**. *NeuroReport*, pages 675–678, 1993. 13

[24] Gemma A. Calvert, Edward T. Bullmore, Michael J. Brammer, Ruth Campbell, Steven C. R. Williams, Philip K. McGuire, Peter W. R. Woodruff, Susan D. Iversen, and Anthony S. David. **Activation of Auditory Cortex During Silent Lipreading**. *Science*, **276**(5312):593–596, 1997. 13

[25] Matthew D. Robson, Jennifer L. Dorosz, and John C. Gore. **Measurements of the Temporal fMRI Response of the Human Auditory Cortex to Trains of Tones**. *NeuroImage*, **7**(3):185 – 198, 1998. 13

[26] Jessica A. Church, Steven E. Petersen, and Bradley L. Schlaggar. **The Task B problem and other considerations in developmental functional neuroimaging**. *Human Brain Mapping*, **31**(6):852–862, 2010. 14

[27] Michael C. Stevens. **The developmental cognitive neuroscience of functional connectivity**. *Brain and Cognition*, **70**(1):1 – 12, 2009. 14

[28] K Supekar, M Musen, and V. Menon. **Development of large-scale functional brain networks in children.** *PLoS Biol*, **7**:1–15, 2009. 14, 15, 86

[29] Michael D. Fox and Marcus E. Raichle. **Spontaneous fluctuations in brain activity observed with functional magnetic resonance imaging**. *nat ure reviews,neuro science*, **8**:700–711, 2007. 15

[30] K.J. Friston, C.D. Frith, P.F. Liddle, and R.S. Frackowiak. **Functional connectivity: the principal-component analysis of large (PET) data sets**. *J. Cereb. Blood Flow Metab*, **13**:5C14, 1993. 15, 74

[31] Martijn P. van den Heuvel and Hilleke E. Hulshoff Pol. **Exploring the brain network: A review on resting-state fMRI functional connectivity**. *European Neuropsychopharmacology*, **20**(8):519 – 534, 2010. 15, 17

[32] M.J. Lowe, B.J. Mock, and J.A. Sorenson. **Functional connectivity in single and multislice echoplanar imaging using restingstate fluctuations**. *Neuroimage*, **7**(2):119C132, 1998. 15, 74, 75

[33] Michael Greicius. **Resting-state functional connectivity in neuropsychiatric disorders**. *Current Opinion in Neurology*, **21**(4), 2008. 15

[34] Koene R. A. Van Dijk, Trey Hedden, Archana Venkataraman, Karleyton C. Evans, Sara W. Lazar, and Randy L. Buckner. **Intrinsic Functional Connectivity As a Tool For Human Connectomics: Theory, Properties, and Optimization**. *Journal of Neurophysiology*, **103**(1):297–321, 2010. 15, 16

[35] Shulman GL, Fiez JA, Corbetta M, Buckner RL, Miezin FM, Raichle ME, and Petersen SE. **Common blood flow changes across visual tasks: II. Decreases in cerebral cortex**. *J Cognit Neurosci*, **9**:648C663, 1997. 15

[36] M.D Greicius, Ben Krasnow, Allan L. Reiss, and Vinod Menon. **Functional connectivity in the resting brain: A network analysis of the default mode hypothesis**. *PNAS*, **100**(1):253–258, 2003. 15, 74, 75

[37] Michael D. Fox, Abraham Z. Snyder, Justin L. Vincent, Maurizio Corbetta, David C. Van Essen, and Marcus E. Raichle. **The human brain is intrinsically organized into dynamic, anticorrelated functional networks**. *Proceedings of the National Academy of Sciences of the United States of America*, **102**(27):9673–9678, 2005. 15, 74, 75, 77, 82

[38] Peter Fransson. **Spontaneous low-frequency BOLD signal fluctuations: An fMRI investigation of the resting-state default mode of brain function hypothesis**. *Human Brain Mapping*, **26**(1):15–29, 2005. 15

[39] Damien A. Fair, Alexander L. Cohen, Nico U. F. Dosenbach, Jessica A. Church, Francis M. Miezin, Deanna M. Barch, Marcus E. Raichle, Steven E. Petersen, and Bradley L. Schlaggar. **The maturing architecture of the brain's default network**. *Proceedings of the National Academy of Sciences*, **105**(10):4028–4032, 2008. 15, 17, 86, 101

[40] Peter Fransson, Beatrice SkiLd, Mathias EngstrM, Boubou Hallberg, Mikael Mosskin, Ulrika Den, Hugo Lagercrantz, and Mats Blennow. **Spontaneous Brain Activity in the Newborn Brain During Natural Sleep-An fMRI Study in Infants Born at Full Term**. *Pediatric Research*, **66**(3), 2009. 15

[41] W. Lin, Q. Zhu, W. Gao, Y. Chen, C.-H. Toh, M. Styner, G. Gerig, J.K. Smith, B. Biswal, and J.H. Gilmore. **Functional Connectivity MR Imaging Reveals Cortical Functional Connectivity in the Developing Brain**. *American Journal of Neuroradiology*, **29**(10):1883–1889, November 2008. 15, 17

[42] Kaustubh Supekar, Lucina Q. Uddin, Katherine Prater, Hitha Amin, Michael D. Greicius, and Vinod Menon. **Development of functional and structural connectivity within the default mode network in young children**. *NeuroImage*, **52**:290–301, 2010. 15, 86, 101

[43] Lucina Q Uddin, Kaustubh Supekar, and Vinod Menon. **Typical and atypical development of functional human brain networks: insights from resting-state fMRI**. *Frontiers in Systems Neuroscience*, **4**, 2010. 15, 16, 17

[44] Dietmar Cordes, Victor M. Haughton, Konstantinos Arfanakis, Gary J. Wendt, Patrick A. Turski, Chad H. Moritz, Michelle A. Quigley, and M. Elizabeth Meyerand. **Mapping Functionally Related Regions of Brain with Functional Connectivity MR Imaging**. *AJNR Am J Neuroradiol*, **21**(9):1636–1644, 2000. 15

[45] Michael D. Fox, Dongyang Zhang, Abraham Z. Snyder, and Marcus E. Raichle. **The Global Signal and Observed Anticorrelated Resting State Brain Networks**. *Journal of Neurophysiology*, **101**(6):3270–3283, June 2009. 15

[46] Adrien E. Desjardins, Kent A. Kiehl, and Peter F. Liddle. **Removal of Confounding Effects of Global Signal in Functional MRI Analyses**. *NeuroImage*, **13**(4):751 – 758, 2001. 16

[47] Andreas Weissenbacher, Christian Kasess, Florian Gerstl, Rupert Lanzenberger, Ewald Moser, and Christian Windischberger. **Correlations and anticorrelations in resting-state functional connectivity MRI: A quantitative comparison of preprocessing strategies**. *NeuroImage*, **47**(4):1408 – 1416, 2009. 16

[48] K.J. Friston. **The disconnection hypothesis**. *Schizophr. Res.*, **30**(2):115C125, 1998. 16, 75

[49] V. D. Calhoun, T. Adali, G. D. Pearlson, and J. J. Pekar. **A method for making group inferences from functional MRI data using independent component analysis**. *Human Brain Mapping*, **16**(2):131–131, 2002. 16

[50] Dietmar Cordes, Vic Haughton, John D. Carew, Konstantinos Arfanakis, and Ken Maravilla. **Hierarchical clustering to measure connectivity in fMRI resting-state data**. *Magnetic Resonance Imaging*, **20**(4):305 – 317, 2002. 16

[51] Martijn van den Heuvel, Rene Mandl, and Hilleke Hulshoff Pol. **Normalized Cut Group Clustering of Resting-State fMRI Data**. *PLoS ONE*, **3**(4):e2001, 04 2008. 16

[52] J. S. Damoiseaux, S. A. R. B. Rombouts, F. Barkhof, P. Scheltens, C. J. Stam, S. M. Smith, and C. F. Beckmann. **Consistent resting-state networks across healthy subjects**. *Proceedings of the National Academy of Sciences*, **103**(37):13848–13853, 2006. 16, 74, 75

[53] Sporns O Bullmore E. **Complex brain networks: graph theoretical analysis of structural and functional systems**. *Nat Rev Neurosci*, **10**:186–198, 2009. 16, 17

[54] Vince D. Calhoun, Jingyu Liu, and Tlay Adal. **A review of group ICA for fMRI data and ICA for joint inference of imaging, genetic, and ERP data**. *NeuroImage*, **45**(1, Supplement 1):S163 – S172, 2009. ¡ce:title¿Mathematics in Brain Imaging¡/ce:title¿. 16

[55] Christian F Beckmann, Marilena DeLuca, Joseph T Devlin, and Stephen M Smith. **Investigations into resting-state connectivity using independent component analysis**. *Philosophical Transactions of the Royal Society B: Biological Sciences*, **360**(1457):1001–1013, 2005. 16, 75

[56] Michael C Stevens. **The developmental cognitive neuroscience of functional connectivity**. *Brain and Cognition*, **70**(1):1–12, 2009. 16

[57] Peter Fransson, Beatrice Skild, Sandra Horsch, Anders Nordell, Mats Blennow, Hugo Lagercrantz, and Ulrika den. **Resting-state networks in the infant brain**. *Proceedings of the National Academy of Sciences*, **104**(39):15531–15536, 2007. 16, 74, 81

[58] Wen-Ching Liu, Judy F. Flax, Kevin G. Guise, Vishad Sukul, and April A. Benasich. **Functional connectivity of the sensorimotor area in naturally sleeping infants**. *Brain Research*, **1223**(0):42 – 49, 2008. 16

[59] Thomason ME, Chang CE, Glover GH, Gabrieli JDE, Greicius MD, and Gotlib IH. **Default-mode function and task-induced deactivation have overlapping brain substrates in children.** *Neuroimage*, **41**:1493–1503, 2008. 16, 74

[60] M. C. Stevens, G. D. Pearlson, and V. D. Calhoun. **Changes in the interaction of resting-state neural networks from adolescence to adulthood**. *Human Brain Mapping*, **30**(1):2356–2366, 2009. 16

[61] PETER FRANSSON, BEATRICE SKIÖLD, MATHIAS ENGSTRÖM, BOUBOU HALLBERG, MIKAEL MOSSKIN, ULRIKA ÅDEN, HUGO LAGERCRANTZ, and MATS BLENNOW. **Spontaneous Brain Activity in the Newborn Brain During Natural Sleep-An fMRI Study in Infants Born at Full Term**. *Pediatric Research*, **66**(3):301–305, 2009. 16, 74, 81

[62] Peter Fransson, Ulrika Åden, Mats Blennow, and Hugo Lagercrantz. **The Functional Architecture of the Infant Brain as Revealed by Resting-State fMRI**. *Cerebral Cortex*, **21**(1):145–154, 2011. 16, 74, 75, 83

[63] A.M. Clare Kelly, Adriana Di Martino, Lucina Q. Uddin, Zarrar Shehzad, Dylan G. Gee, Philip T. Reiss, Daniel S. Margulies, F. Xavier Castellanos, and Michael P. Milham. **Development of Anterior Cingulate Functional Connectivity from Late Childhood to Early Adulthood**. *Cereb Cortex*, **19**:640–657, 2009. 17

[64] Randy L. Buckner and Justin L. Vincent. **Unrest at rest: Default activity and spontaneous network correlations**. *NeuroImage*, **37**(4):1091 – 1096, 2007. 17

[65] Murty USR Bondy JA. *Graph theory with applications*. New York: American Elsevier Pub. Co., 1976. 17

[66] E. W. Dijkstra. **A note on two problems in connexion with graphs**. *Numerische Mathematik*, **1**:269–271, 1959. 10.1007/BF01386390. 18

[67] V. Latora and M. Marchiori. **Efficient behavior of small-world networks**. *Phys. Rev. Lett.*, **87**(19):198701, 2001. 18, 90

[68] R.L Buckner, J Sepulcre, T Talukdar, F.M Krienen, H Liu, T Hedden, J.R Andrews-Hanna, R.A Sperling, and K.A. Johnson. **Cortical hubs revealed by intrinsic functional connectivity: Mapping, assessment of stability, and relation to Alzheimer's disease**. *J Neurosci*, **29**(6):1860–1873, 2009. 19, 90

[69] Sporns O Bullmore E. **Complex brain networks: graph theoretical analysis of structural and functional systems**. *Nat Rev Neurosci*, **10**:186–198, 2009. 19

[70] Rubinov M and Sporns O. **Complex network measures of brain connectivity: Uses and interpretations.** *NeuroImage*, **52**:1059–1069, 2010. 19, 90

[71] Watts DJ and Strogatz SH. **Collective dynamics of 'small-world' networks**. *Nature*, **393**:440–442, 1998. 19

[72] Damien A. Fair, Alexander L. Cohen, Jonathan D. Power, Nico U. F. Dosenbach, Jessica A. Church, Francis M. Miezin, Bradley L. Schlaggar, and Steven E. Petersen. **Functional Brain Networks Develop from a local to Distributed Organisation**. *PLoS Comput Biol*, **5**(5):e1000381, 05 2009. 19, 74, 86

[73] Liang Wang, Chaozhe Zhu, Yong He, Yufeng Zang, QingJiu Cao, Han Zhang, Qiuhai Zhong, and Yufeng Wang. **Altered Small-World Brain Functional Networks in Children With Attention-Deficit/Hyperactivity Disorder**. *Human Brain Mapping*, **30**:638C649, 2009. 19

[74] Sophie Achard, Raymond Salvador, Brandon Whitcher, John Suckling, and Ed Bullmore. **A Resilient, Low-Frequency, Small-World Human Brain Functional Network with Highly Connected Association Cortical Hubs**. *The Journal of Neuroscience*, **26**(1):63–72, 2006. 19

[75] Raymond Salvador, John Suckling, Martin R. Coleman, John D. Pickard, David Menon, and Ed Bullmore. **Neurophysiological Architecture of Functional Magnetic Resonance Images of Human Brain**. *Cerebral Cortex*, **15**(9):1332–1342, September 2005. 19, 74, 75

[76] B. Fischl and A. M. Dale. **Measuring the thickness of the human cerebral cortex from magnetic resonance images**. *Proc. Natl. Acad. Sci.*, **97**(20):11050–11055, 2000. 19, 87

[77] Yong He, Zhang J. Chen, and Alan C. Evans. **Small-World Anatomical Networks in the Human Brain Revealed by Cortical Thickness from MRI**. *Cerebral Cortex*, **17**(10):2407–2419, 2007. 19, 73

[78] B. Fischl and A.M. Dale. **Measuring the thickness of the human cerebral cortex from magnetic resonance images**. *Proc Natl Acad Sci USA*, **97**:11050–11055, 2000. 19, 41

[79] Dietsje D. Jolles, Mark A. van Buchem, Eveline A. Crone, and Serge A.R.B. Rombouts. **A Comprehensive Study of Whole-Brain Functional Connectivity in Children and Young Adults**. *Cerebral Cortex*, **21**(2):385–391, 2011. 19, 75, 81, 82, 83, 92

[80] Kaustubh Supekar, Mark Musen, and Vinod Menon. **Development of Large-Scale Functional Brain Networks in Children**. *PLoS Biol*, **7**:e1000157, 07 2009. 19, 74, 75

[81] Damien A. Fair, Alexander L. Cohen, Nico U. F. Dosenbach, Jessica A. Church, Francis M. Miezin, Deanna M. Barch, Marcus E. Raichle, Steven E. Petersen, and Bradley L. Schlaggar. **The maturing architecture of the brain's default network**. *Proceedings of the National Academy of Sciences*, **105**(10):4028–4032, 2008. 19, 75, 82, 83

[82] J. Talairach and G. Szikla. *Atlas of Stereotaxic Anatomy of the Telencephalon*. Masson and Cie, Paris, 1967. 20

[83] J. Talairach and P. Tournoux. *Co-planar Stereotaxic Atlas of the Human Brain: 3-Dimensional Proportional System - an Approach to Cerebral Imaging*. Thieme Medical Publishers, New York, NY, 1988. 20, 66

[84] Hill D.L.G., Batchelor P.G., Holden M., and Hawkes D.J. **Medical image registration**. *Phys. Med. Biol.*, **46**:R1–R45, 2001. 20

[85] H.A. Drury, D.C. Van Essen, C.H. Anderson, C.W. Lee, T.A. Coogan, and J.W. Lewis. **Computerized Mappings of the Cerebral Cortex: A Multiresolution Flattening Method and a Surface-Based Coordinate System**. *Journal of Cognitive Neuroscience Winter*, **8**(1):1–28, 1996. 20

[86] D.C. Van Essen, H.A. Drury, S. Joshi, and M.I. Miller. **Functional and structural mapping of human cerebral cortex: solutions are in the surfaces.** *Proc Natl Acad Sci.*, **95**:788–795, 1998. 20, 27, 41

[87] D.C. Van Essen, J. Harwell, D. Hanlon, and J. Dickson. *Surface based atlases and a database of cortical structure and function*. John Wiley and Sons, NJ,, 2005. 20, 38, 42, 49, 50, 51, 64, 65, 67

[88] A. Qiu and M.I. Miller. **Cortical hemisphere registration via large deformation diffeomorphic metric curve mapping.** *the 10th International Conference on Medical Image Computing and Computer Assisted Intervention*, **10**:186–193, 2007. 20, 22, 42, 44, 46

[89] S. C. Joshi, M. I. Miller, and U. Grenander. **On the geometry and shape of brain sub–manifolds**. *Int. J. Pattern Recognition and Artificial Intelligence*, **11**:1317–1343, 1997. 20

[90] R. Goebel, U. Hasson, I. Lefi, and R. Malach. **Statistical analyses across aligned cortical hemispheres reveal high-resolution: population maps of human visual cortex**. *Neuroimage*, **22(Suppl 2)**, 2004. 21

[91] B.T. Thomas Yeo, Mert R. Sabuncu, Tom Vercauteren, Nicholas Ayache, Bruce Fischl, and Polina Golland. **Spherical Demons: Fast Surface Registration**, 2008. 21

[92] B.T. Thomas Yeo, Mert R. Sabuncm, Tom Vercauteren, Nicholas Ayache, Bruce Fischl, and Polina Golland. **Spherical Demons: Fast Diffeomorphic Landmark-Free Surface Registration**. *IEEE TRANSACTIONS ON MEDICAL IMAGING*, 2009. 21, 42

[93] R. Desai, E. Liebenthal, E.T. Possing, E. Waldron, and J.R. Binder. **Volumetric vs. surface-based alignment for localization of auditory cortex activation**. *NeuroImage*, **26**:1019 – 1029, 2005. 21, 42, 63, 64

[94] J. Glaunès. *Transport par diff'eomorphismes de points, de mesures et de courants pour la comparaison de formes etl l'anatomie num'erique*. PhD thesis, Universit'e Paris, 2005. 22

[95] A. Qiu, M. Albert, L. Younes, and M.I. Miller. **Time sequence diffeomorphic metric mapping and parallel transport track time-dependent shape changes**. *Neuroimage*, **45**:S51CS60, 2009. 22, 28

[96] A. Trouvé. **Infinite Dimensional Group Action and Pattern Recognition**. Technical report, DMI, Ecole Normale Suprieure, 1995. 23, 29

[97] P. Dupuis, U. Grenander, and M. I. Miller. **Variational problems on flows of diffeomorphisms for image matching**. *Quaterly of Applied Math.*, **56**:587–600, 1998. 23, 29

[98] M. Vaillant and J. Glaunès. **Surface matching via currents.** *Lecture Notes in Comp Sci. Inform. Proc. in Med. Imaging*, **3565**:381–392, 2005. 24, 31, 42, 44, 46

[99] M. Vaillant, A. Qiu, J. Glaunès, and M.I. Miller. **Difffeomorphic metric surface mapping in subregion of the superior temporal gyrus**. *NeuroImage*, **34**(3):1149–1159, 2007. 24, 27, 31, 42, 44, 46

[100] S. Durrleman, X. Pennec, A. Trouv́e, P. Thompson, and N. Ayache. **Inferring brain variability from diffeomorphic deformations of currents: An integrative approach**. *Medical Image Analysis*, **12**:626–637, 2008. 24, 28, 31

[101] S. Durrleman, X. Pennec, A. Trouv́e, P. Thompson, and N. Ayache. **Measuring brain variability via sulcal lines registration: A diffeomorphic approach**. *MICCAI*, **1**:675–682, 2007. 24, 27, 28, 31

[102] S. Durrleman, X. Pennec, A. Trouv́e, P. Thompson, and N. Ayache. **Sparse approximation of currents for statistics on curves and surfaces**. *MICCAI*, **5242**:390–398, 2008a. 24, 28, 31

[103] Joan Glaunes, Alain Trouv̀e, and Laurent Younes. **Diffeomorphic Matching of Distributions: A New Approach for Unlabelled Point-Sets and Sub-Manifolds Matching**. *Computer Vision and Pattern Recognition, IEEE Computer Society Conference on*, **2**:712–718, 2004. 24

[104] M. Vaillant and J. Glaunès. **Surface Matching via Currents**. *Lecture Notes in Comp. Sci.: Inform. Proc. in Med. Imaging*, **3565**:381–392, 2005. 24, 25, 26, 28, 37, 40, 41

[105] Joan Glaunès, Anqi Qiu, Michael I. Miller, and Laurent Younes. **Large Deformation Diffeomorphic Metric Curve Mapping**. *submitted to IJCV*, 2008. 24, 25, 27, 28, 37, 40, 41

[106] Marc Vaillant, Anqi Qiu, Joan Glaunès, and Michael I. Miller. **Diffeomorphic Metric Surface Mapping in subregion of the Superior Temporal Gyrus**. *NeuroImage*, **34**:1149–1159, 2007. 25, 27, 28, 37, 40

[107] D.C. Van Essen. **Surface-based approaches to spatial localization and registration in primate cerebral cortex**. *NeuroImage*, **23**:s97Cs107, 2004b. 27, 40, 41, 42

[108] B. Fischl, M.I. Sereno, and A.M. Dale. **Cortical surface-based analysis: II. inflation, flattening, and a surface-based coordinate system.** *NeuroImage*, **9**:195– 207, 1999a. 27, 28, 34, 41, 42, 49

[109] C. Clouchoux, O. Coulon, D. Riviere, A. Cachia, J.F. Mangin, and J. Regis. **Anatomically constrained surface parameterization for cortical localization**. *MICCAI*, **3750**:344–351, 2005. 27, 41

[110] Oliver Lyttelton, Maxime Boucher, Steven Robbins, and Alan Evans. **An unbiased iterative group registration template for cortical surface analysis**. *NeuroImage*, **34**:1535–1544, 2007. 27, 41, 67

[111] S. Robbins, A. Evans, D. Collins, and S. Whitesides. **Tuning and comparing spatial normalization methods**. *Med. Image Anal.*, **8**:311C323, 2004. 27, 40, 41, 42

[112] P.M. Thompson, C. Schwartz, R.T. Lin, A.A. Khan, and A.W. Toga. **Three-dimensional statistical analysis of sulcal variability in the human brain**. *J. Neurosci.*, **16**:4261C4274, 1996. 27, 42

[113] M.K. Chung, S.M. Robbins, K.M. Dalton, R.J. Davidson, A.L. Alexander, and A.C. Evans. **Cortical thickness analysis in autism with heat kernel smoothing**. *NeuroImage*, **25**:1256C1265, 2005. 27, 41, 77, 88

[114] K. L. Narr, P. M. Thompson, P. Szeszko, D. Robinson, S. Jang, R. P. Woods, S. Kim, K. M. Hayashi, D. Asunction, A. W. Toga, and R. M. Bilder. **Regional specificity of hippocampal volume reductions in first-episode schizophrenia**. *NeuroImage*, **21**(4):1563–75, 2004. 27

[115] E. R. Sowell, P. M. Thompson, D. Rex, D. Kornsand, K. D. Tessner, T. L. Jernigan, and A. W. Toga. **Mapping sulcal pattern asymmetry and local cortical surface gray matter distribution in vivo: maturation in perisylvian cortices**. *Cereb Cortex*, **12**(1):17–26., 2002. 27, 34, 117

[116] Alan Anticevic, Donna L. Dierker, Sarah K. Gillespie, Grega Repovs, John G. Csernansky, David C. Van Essen, and Deanna M. Barch. **Comparing surface-based and volume-based analyses of functional neuroimaging data in patients with schizophrenia**. *Neuroimage*, **41**(3):835–848, 2008. 28

[117] P. Cachier, J.-F. Mangin, X. Pennec, D. Rivière, D. Papadopoulos-Orfanos, J. Régis, and N. Ayache. **Multisubject Non-Rigid Registration of Brain MRI using Intensity and Geometric Features**. In W.J. Niessen and M.A. Viergever, editors, *4th Int. Conf. on Medical Image Computing and Computer-Assisted Intervention (MICCAI'01)*, **2208** of *LNCS*, pages 734–742. Springer-Verlag, 2001. 28

[118] D.L. Collins, P. Neelin, T.M. Peters, and A.C. Evans. **Automatic 3D intersubject registration of MR volumetric data in standardized Talairach space**. *J. Comp. Assist. Tomog.*, **18**:192C205, 1994. 28, 70

[119] M. I. Miller, A. Trouvé, and L. Younes. **On Metrics and Euler-Lagrange Equations of Computational Anatomy**. *Ann. Rev. Biomed. Engng*, **4**:375–405, 2002. 28, 29, 67, 71

[120] M. I. Miller, A. Trouvé, and L. Younes. **Geodesic Shooting for Computational Anatomy**. *J. Mathematical Imaging and Vision*, **24**:209–228, 2006. 28, 29, 71

[121] M. Vaillant, M. I. Miller, L. Younes, and A. Trouvé. **Statistics on diffeomorphisms via tangent space representations**. *NeuroImage*, **23**:161–169, 2004. 28, 67, 68, 71

[122] V. I. Arnold. **Sur la géometrie differentielle des groupes de Lie de dimension infinie et ses applications à l'hydrodynamique des fluides parfaits**. *Ann. Inst. Fourier (Grenoble)*, **1**:319–361, 1966. 29

[123] C. Yang, R. Duraiswami, N. Gumerov, and L. Davis. **Improved fast gauss transform and effficient kernel density estimation**. *IEEE Int. Conf. Comput. Vis.*, page 464C471, 2003. 34

[124] M. Ono, S. Kubick, and C. Abernathey. *Atlas of the Cerebral Sulci*. Georg Thieme Verlag Thieme Medical Publishers, 1990. 34, 117

[125] J. T. Ratnanather, P. E. Barta, Honeycutt. N. A., N. Lee, N. G. Morris, A. C. Dziorny, M. K. Hurdal, G. D. Pearlson, and M. I. Miller. **Dynamic programming generation of boundaries of local coordinatized submanifolds in the neocortex: application to the planum temporale**. *NeuroImage*, **20**(1):359–377, 2003. 34, 117

[126] D. S. Marcus, T. H. Wang, J. Parker, J. G. Csernansky, J. C. Morris, and R. L. Buckner. **Open Access Series of Imaging Studies (OASIS): cross-sectional MRI data in young, middle aged, nondemented, and demented older adults**. *J Cogn Neurosci*, **19**:1498–1507, 2007. 38, 68

[127] Anqi Qiu, Laurent Younes, Lei Wang, J. Tilak Ratnanather, Sarah K. Gillepsie, Gillian Kaplan, John G. Csernansky, and Michael I. Miller. **Combining Anatomical Manifold Information via Diffeomorphic Metric Mappings for Studying Cortical Thinning of the Cingulate Gyrus in Schizophrenia**. *Neuroimage*, **37**:821–833, 2007. 40

[128] M. I. Miller, M. F. Beg, C. Ceritoglu, and C. Stark. **Increasing the power of functional maps of the medial temporal lobe by using large deformation diffeomorphic metric mapping**. *Proc Natl Acad Sci*, **102**:9685–9690, 2005. 40

[129] C. B. Kirwan, C.K. Jones, M. I. Miller, and C. E. Stark. **High-resolution fMRI investigation of the medial temporal lobe**. *Hum Brain Mapping*, **28**:959–966, 2007. 40

[130] Fischl B., van der Kouwe A., Destrieux C., Halgren E., Segonne F., Salat D.H., Busa E., Seidman L.J., Goldstein J., Kennedy D., Caviness V., Makris N., Rosen B., and Dale A.M. **Automatically parcellating the human cerebral cortex**. *Cereb. Cortex*, **14**:11–22, 2004. 41

[131] D.C. Van Essen. **Towards a quantitative, probabilistic neuroanatomy of cerebral cortex**. *Cortex*, **40**:211–212, 2004a. 41

[132] E. R. Sowell, B. S. Peterson, P. M. Thompson, S. E. Welcome, A. L. Henkenius, and A. W. Toga. **Mapping cortical change across the human life span**. *Nat. Neurosci.*, **6**:309–315, 2003. 41

[133] K.L. Narr, R.M. Bilder, E. Luders, P.M. Thompson, R.P. Woods, D. Robinson, P.R. Szeszko, T. Dimtcheva, M. Gurbani, and A.W. Toga. **Asymmetries of cortical shape: Effects of handedness, sex and schizophrenia**. *NeuroImage*, **34**:939–948, 2007. 41, 66

[134] X. Gu, Y. Wang, T.F. Chan, P.M. Thompson, and S.T. Yau. **Genus zero surface conformal mapping and its application to brain surface mapping**. *IEEE Trans Med Imaging*, **23**:949–958, 2004. 42

[135] M. K. Hurdal and K. Stephenson. **Cortical cartography using the discrete conformal approach of circle packing**. *NeuroImage*, **23**:119–128, 2004. 42

[136] J. Zhong and A. Qiu. **Multi-Manifold Diffeomorphic Metric Mapping for Aligning Cortical Hemisphere Surfaces**. *NeuroImage*, **49**:355–365, 2010. 42, 44, 46, 48, 77, 87

[137] A. Qiu, L. Younes, L. Wang, J.T. Ratnanather, S.K. Gillepsie, G. Kaplan, J.G. Csernansky, and M.I. Miller. **Combining anatomical manifold information via diffeomorphic metric mappings for studying cortical thinning of the cingulate gyrus in schizophrenia**. *Neuroimage*, **37**:821C833, 2007. 42

[138] D.S. Marcus, T.H. Wang, J. Parker, J.G. Csernansky, J.C. Morris, and R.L. Buckner. **Open access series of imaging studies (oasis), cross-sectional mri data in young, middle aged, nondemented, and demented older adults.** *J Cogn Neurosci*, **19**:1498–1507, 2007. 43

[139] B. Fischl, D.H. Salat, E. Busa, M. Albert, M. Dieterich, C. Haselgrove, A. Kouwe, R. Killiany, D. Kennedy, S. Klaveness, A. Montillo, N. Makris, B. Rosen, and A.M. Dale. **Whole Brain Segmentation: Neurotechnique Automated Labeling of Neuroanatomical Structures in the Human Brain**. *Neuron*, **33**:341–355, 2002. 44

[140] R. Toro and Y. Burnod. **Geometric atlas: modeling the cortex as an organized surface**. *Neuroimage*, **20**:1468–1484, 2003. 44, 67

[141] J.T. Ratnanather, P.E. Barta, N.A. Honeycutt, N. Lee, N.G. Morris, A.C. Dziorny, M.K. Hurdal, G.D. Pearlson, and M.I. Miller. **Dynamic programming generation of boundaries of local coordinatized submanifolds in the neocortex: application to the planum temporale**. *NeuroImage*, **20**:359–377, 2003. 46, 105

[142] M.-P. Dubuisson and A. Jain. **A modified Hausdorff distance for object matching**. *Proceedings of the 12th IAPR International Conference on Computer Vision and Image Processing*, **1**:566–568, 1994. 50

[143] D. Pantazis, A. Joshi, J. Jiang, D. Shattuck, L.E. Bernstein, H. Damasio, and R.M. Leahy. **Comparison of landmark-based and automatic methods for cortical surface registration**. *Neuroimage*, 2009. 50, 64

[144] A. Qiu, D. Bitouk, and M.I. Miller. **Smooth functional and structural maps on the neocortex via orthonormal bases of the Laplace-Beltrami operator**. *IEEE Trans Med Imaging*, **25**:1296–1306, 2006. 53, 77, 88

[145] A. Qiu, M. Vaillant, P. Barta, J.T. Ratnanather, and M.I. Miller. **Region-of-interest-based analysis with application of cortical thickness variation of left planum temporale in schizophrenia and psychotic bipolar disorder**. *Hum Brain Mapp*, **29**:973–985, 2008. 63

[146] J-F. Mangin, D. Riviere, A. Cachia, E. Duchesnay, Y. Cointepas, D. Papadopoulus-Orfanos, T. Ochiai, and J. Regis. **A framework for studying cortical folding patterns**. *NeuroImage*, 2004. 63

[147] C.Y. Kao, M. Hofer, G. Sapiro, J. Stem, K. Rehm, and D.A. Rottenberg. **A geometric method for automatic extraction of sulcal fundi**. *IEEE Trans Med Imaging*, **26**:530C540, 2007. 63

[148] A.A. Joshi, D.W. Shattuck, P.M. Thompson, and R.M. Leahy. **Surface-constrained volumetric brain registration using harmonic mappings**. *IEEE Trans Med Imaging*, **26**:1657–1669, 2007. 64

[149] R. Goebel, F. Esposito, and E. Formisano. **Analysis of functional image analysis contest (FIAC) data with brainvoyager QX: From single-subject to cortically aligned group general linear model analysis and self-organizing group independent component analysis**. *Hum Brain Mapp*, **27**:392–401, 2006. 64

[150] P. M. Thompson, C. Schwartz, and A. W. Toga. **High-resolution random mesh algorithms for creating a probabilistic 3D surface atlas of the human brain**. *NeuroImage*, **3**(1):19–34, 1996. 66

[151] Tessa Dekker, Denis Mareschal, Martin I. Sereno, and Mark H. Johnson. **Dorsal and ventral stream activation and object recognition performance in school-age children**. *NeuroImage*, **57**:659–670, 2011. 66, 85, 100

[152] D. C. VanEssen and H. A. Drury. **Structural and functional analyses of human cerebral cortex using a surface–based atlas**. *J. Neurosci.*, **17**(18):7079–7102, 1997. 66

[153] A. C. Evans, D. L. Collins, S. R. Mills, E. D. Brown, R. L. Kelly, and T. M. Peters. **3D statistical neuroanatomical models from 305 MRI volumes**. *Proc. IEEE-Nuclear Science Symposium and Medical Imaging Conference*, **1445**:1813C1817, 1993. 67

[154] K.J. Friston, J. Ashburner, C.D. Frith, J.-B. Poline, J. D. Heather, Liddle, and R.S.J. Frackowiak. **Spatial Registration and Normalization of Images**. *Human Brain Mapping*, **2**:165–189, 1995. 67

[155] J. Ashburner and K. J. Friston. **Voxel-Based Morphometry-The Methods**. *NeuroImage*, **11**:805–821, 2000. 67

[156] C.D. Good, I.S. Johnsrude, J. Ashburner, R.N.A. Henson, K.J. Friston, and R.S.J. Frackowiak. **A Voxel-Based Morphometric Study of Ageing in 465 Normal Adult Human Brains**. *NeuroImage*, **14**:21–36, 2001. 67

[157] P. Kochunov, J. Lancaster, P. Thompson, A.W. Toga, P. Brewer, J. Hardies, and P. Fox. **An optimized individual target brain in the Talairach coordinate system**. *NeuroImage*, **17**:922–927, 2002. 67

[158] D. Seghers, E. D́Agostino, D. Maes, F.and Vandermeulen, and P. Suetens. **Construction of a Brain Template From MR Images Using State-of-the-Art Registration and Segmentation techniques**. *Lecture Notes in Computer Science. Springer-Verlag, Berlin, Germany*, **3216**:696–703, 2004. 67

[159] S.C. Joshi, B. Davis, M. Jomier, and G. Gerig. **Unbiased diffeomorphic atlas construction for computational anatomy**. *NeuroImage*, **23**:151C160, 2004. 67

[160] S. Allassonniere, Y. Amit, and A. Trouvé. **Towards a coherent statistical framework for dense deformable template estimation.** *Journal Of The Royal Statistical Society Series B*, **69**:3–29, 2007. 67

[161] J. Ma, M.I. Miller, A. Trouvé, and L. Younes. **Bayesian template estimation in computational anatomy**. *NeuroImage*, **42**:252–261, 2008. 67

[162] Miller M.I., Priebe C.E., Qiu A., Fischl B., Kolasny A., Brown T., Park Y., Ratnanather J.T., Busa E., Jovicich J., Yu P., Dickerson B.C., Buckner R.L., and BIRN t.M. **Collaborative Computational Anatomy: An MRI Morphometry Study of the Human Brain Via Diffeomorphic Metric Mapping**. *Human Brain Mapping*, **30**:2132–2141, 2009. 67

[163] Qiu A., Brown T., Fischl B., Kolasny A., Ma J., Buckner R.L., and Miller M.I. **Subcortical Structure Template Generation with its Applications in Shape Analysis**. Human Brain Mapping, Australia, 2008. 67

[164] Anqi Qiu and Michael I. Miller. **Multi-Structure Network Shape Analysis via Normal Surface Momentum Maps**. *NeuroImage*, 2008. 68

[165] B. Avants and J. C. Gee. **Geodesic Estimation for Large Deformation Anatomical Shape and Intensity Averaging**. *NeuroImage*, **23**:139–150, 2004. 70

[166] S. C. Joshi, B. Davis, M. Jomier, and G. Gerig. **Unbiased diffeomorphic atlas construction for computational anatomy**. *NeuroImage*, **23**:151–160, 2004. 70

[167] Howard Eichenbaum. **A Cortical-Hippocampal System for Declarative Memory**. *NATURE REVIEWS, NEUROSCIENCE*, **1**:41–50, 2000. 73

[168] Robyn L. Bluhm, C. Richard Clark, Alexander C. McFarlane, Kathryn A. Moores, Marnie E. Shaw, and Ruth A. Lanius. **Default network connectivity during a working memory task**. *Human Brain Mapping*, **32**(7):1029–1035, 2011. 73

[169] P.R. Huttenlocher. *Neural Plasticity: The Effects of Environment on the Development of the Cerebral Cortex*. Cambridge,MA: Harvard University Press, 2002. 73

[170] M. Sur and J.L. Rubenstein. **Patterning and plasticity of the cerebral cortex**. *Science*, **310**:805C810, 2005. 73

[171] Galvan A. Casey BJ, Getz S. **The adolescent brain**. *Dev Rev.*, **28**:62–77, 2008. 73

[172] Blakemore SJ. **The social brain in adolescence**. *Nat Rev Neurosci*, **9**:267–277, 2008. 73

[173] OHearn K Luna B, Padmanabhan A. **What has fMRI told us about the development of cognitive control through adolescence?** *Brain Cogn.*, **72**:101–113, 2010. 73

[174] A.M. Clare Kelly, Adriana Di Martino, Lucina Q. Uddin, Zarrar Shehzad, Dylan G. Gee, Philip T. Reiss, Daniel S. Margulies, F. Xavier Castellanos, and Michael P. Milham. **Development of Anterior Cingulate Functional Connectivity from Late Childhood to Early Adulthood**. *Cerebral Cortex*, **19**(3):640–657, 2009. 74, 86, 100, 101

[175] M.J. Webster, L.G Ungerleider, and J. Bachevalier. **Development and plasticity of the neural circuitry underlying visual recognition memory**. *Can. J. Physiol. Pharmacol.*, **73**:1364–1371, 1995. 74

[176] Torkel Klingberg, Hans Forssberg, and Helena Westerberg. **Increased Brain Activity in Frontal and Parietal Cortex Underlies the Development of Visuospatial Working Memory Capacity during Childhood**. *Journal of Cognitive Neuroscience*, **14**(1):1–10, 2002. 74, 85, 100, 101

[177] Torkel Klingberg. **Development of a superior frontal-intraparietal network for visuo-spatial working memory**. *Neuropsychologia*, **44**:2171–2177, 2006. 74, 85

[178] Bharat B. Biswal, Joel Van Kylen, and James S. Hyde. **Simultaneous assessment of flow and BOLD signals in resting-state functional connectivity maps**. *NMR in Biomedicine*, **10**(4-5):165–170, 1997. 74

[179] J.L Vincent, A.Z Snyder, M.D Fox, B.J Shannon, J.R Andrews, M.E Raichle, and R.L Buckner. **Coherent spontaneous activity identifies a hippocampalparietal memory network**. *J Neurophysiol*, **96**:3517–3531, 2006. 74, 75, 86

[180] Henrica M. A. de Bie, Maria Boersma, Sofie Adriaanse, Dick J. Veltman, Alle Meije Wink, Stefan D. Roosendaal, Frederik Barkhof, Cornelis J. Stam, Kim J. Oostrom, Henriette A. Delemarre-van de Waal, and Ernesto J. Sanz-Arigita. **Resting-state networks in awake five- to eight-year old children**. *Human Brain Mapping*, pages n/a–n/a, 2011. 74, 92

[181] Rosenberg-Lee M., Barth M., and Menon V. **What difference does a year of schooling make?: Maturation of brain response and connectivity between 2nd and 3rd grades during arithmetic problem solving.** *Neuroimage*, **57**:796–808, 2011. 74

[182] Mark J. Lowe, Mario Dzemidzic, Joseph T. Lurito, Vincent P. Mathews, and Micheal D. Phillips. **Correlations in Low-Frequency BOLD Fluctuations Reflect Cortico-Cortical Connections**. *NeuroImage*, **12**(5):582 – 587, 2000. 74

[183] Dietmar Cordes, Victor M. Haughton, Konstantinos Arfanakis, John D. Carew, Patrick A. Turski, Chad H. Moritz, Michelle A. Quigley, and M. Elizabeth Meyerand. **Frequencies Contributing to Functional Connectivity in the Cerebral Cortex in ”Resting-state” Data**. *AJNR Am J Neuroradiol*, **22**(7):1326–1333, 2001. 75, 81

[184] Marilena De Luca, Stephen Smith, Nicola De Stefano, Antonio Federico, and Paul Matthews. **Blood oxygenation level dependent contrast resting state networks are relevant to functional activity in the neocortical sensorimotor system**. *Experimental Brain Research*, **167**:587–594, 2005. 10.1007/s00221-005-0059-1. 75

[185] Martijn van den Heuvel, Rene Mandl, and Hilleke Hulshoff Pol. **Normalized Cut Group Clustering of Resting-State fMRI Data**. *PLoS ONE*, **3**(4):e2001, 04 2008. 75

[186] Damien A. Fair, Nico U. F. Dosenbach, Jessica A. Church, Alexander L. Cohen, Shefali Brahmbhatt, Francis M. Miezin, Deanna M. Barch, Marcus E. Raichle, Steven E. Petersen, and Bradley L. Schlaggar. **Development of distinct control networks through segregation and integration**. *Proceedings of the National Academy of Sciences*, **104**(33):13507–13512, 2007. 75, 82, 86, 101

[187] Damoiseaux JS, Beckmann CF, Arigita EJS, Barkhof F, Scheltens P, Stam CJ, Smith SM, and Rombouts SARB. **Reduced resting-state brain activity in the 'default network' in normal aging.** *Cerebral Cortex*, **18**:1856–1864, 2008. 75, 86

[188] Wei Gao, Hongtu Zhu, Kelly S. Giovanello, J. Keith Smith, Dinggang Shen, John H. Gilmore, and Weili Lin. **Evidence on the emergence of the brain's default network from 2-week-old to 2-year-old healthy pediatric subjects**. *Proceedings of the National Academy of Sciences*, **106**(16):6790–6795, 2009. 75, 82

[189] Sarah Durston and B.J. Casey. **What have we learned about cognitive development from neuroimaging?** *Neuropsychologia*, **44**(11):2149 – 2157, 2006. Advances in Developmental Cognitive Neuroscience. 75

[190] V.D. Calhoun, T. Adali, G.D. Pearlson, and J.J. Pekar. **A method for making group inferences from functional MRI data using independent component analysis**. *Human Brain Mapping*, **14**(3):140–151, 2001. 75

[191] M. De Luca, C.F. Beckmann, N. De Stefano, P.M. Matthews, and S.M. Smith. **fMRI resting state networks define distinct modes of long-distance interactions in the human brain**. *NeuroImage*, **29**(4):1359 – 1367, 2006. 75

[192] Vincent G. van de Ven, Elia Formisano, David Prvulovic, Christian H. Roeder, and David E.J. Linden. **Functional connectivity as revealed by spatial independent component analysis of fMRI measurements during rest**. *Human Brain Mapping*, **22**(3):165–178, 2004. 75

[193] Martina Piefke, Peter H. Weiss, Hans J. Markowitsch, and Gereon R. Fink. **Gender Differences in the Functional Neuroanatomy of Emotional Episodic Autobiographical Memory**. *Human Brain Mapping*, **24**:313–324, 2005. 75

[194] Alecia D. Schweinsburg, Bonnie J. Nagel, and Susan F. Tapert. **fMRI reveals alteration of spatial working memory networks across adolescence**. *Journal of the International Neuropsychological Society*, **11**:631–644, 2005. 75, 92, 100, 101

[195] M. Jenkinson and S. Smith. **A global optimisation method for robust affine registration of brain images**. *Med Image Anal*, **5**:143–156, 2001. 76, 87

[196] J Zhong, D.Y Phua, and A. Qiu. **Quantitative evaluation of LDDMM, FreeSurfer, and CARET for cortical surface mapping**. *Neuroimage*, **52**(1):131–141, 2010. 77, 88

[197] T. Lund, K. Madsen, K. Sidaros, W. Luo, and T. Nichols. **Non-white noise in fMRI: Does modelling have an impact?** *Neuroimage*, **29**:54–66, 2006. 77

[198] J.C. De Munck, S.I. Goncalves, T.J. Faes, J.P. Kuijer, P.J. Pouwels, R.M. Heethaar, and F.H. Lopes da Silva. **A study of the brains resting state based on alpha band power, heart rate and fMRI.** *Neuroimage*, **42**:112–121, 2008. 77

[199] A Qiu, B.J Rosenau, A.S Greenberg, M.K Hurdal, P Barta, S Yantis, and M.I Miller. **Estimating linear cortical magnification in human primary visual cortex via dynamic programming**. *Neuroimage*, **31**:125 – 138, 2006. 77

[200] Kang HC, Burgund ED, Lugar HM, Petersen SE, and Schlaggar BL. **Comparison of functional activation foci in children and adults using a common stereotactic space**. *NeuroImage*, **19**:16C28, 2003. 77

[201] Michael D. Fox, Maurizio Corbetta, Abraham Z. Snyder, Justin L. Vincent, and Marcus E. Raichle. **Spontaneous neuronal activity distinguishes human dorsal and ventral attention systems**. *Proceedings of the National Academy of Sciences*, **103**(26):10046–10051, 2006. 77, 82, 86

[202] Christoph Lehmann, Marcus Herdener, Peter Schneider, Andrea Federspiel, Dominik R. Bach, Fabrizio Esposito, Francesco di Salle, Klaus Scheffler, Robert Kretz, Thomas Dierks, and Erich Seifritz. **Dissociated lateralization of transient and sustained blood oxygen level-dependent signal components in human primary auditory cortex**. *NeuroImage*, **34**(4):1637 – 1642, 2007. 77

[203] Nico U.F. Dosenbach, Kristina M. Visscher, Erica D. Palmer, Francis M. Miezin, Kristin K. Wenger, Hyunseon C. Kang, E. Darcy Burgund, Ansley L. Grimes, Bradley L. Schlaggar, and Steven E. Petersen. **A Core System for the Implementation of Task Sets**. *Neuron*, **50**(5):799–812, 2006. 78, 82

[204] Marcus E. Raichle, Ann Mary MacLeod, Abraham Z. Snyder, William J. Powers, Debra A. Gusnard, and Gordon L. Shulman. **A default mode of brain function**. *Proceedings of the National Academy of Sciences*, **98**(2):676–682, 2001. 78

[205] J.H. Zar, editor. *Biostatistical analysis*. Prentice Hall Inc., Upper Saddle River., 3rd edition, 1996. 78, 89

[206] Linda J. Larson-Prior, John M. Zempel, Tracy S. Nolan, Fred W. Prior, Abraham Z. Snyder, and Marcus E. Raichle. **Cortical network functional connectivity in the descent to sleep**. *Proceedings of the National Academy of Sciences*, **106**(11):4489–4494, 2009. 81, 82, 83

[207] Mark H Johnson. **Development of human brain functions**. *Biological Psychiatry*, **54**(12):1312 – 1316, 2003. 81

[208] B. J. Casey, Jay N. Giedd, and Kathleen M. Thomas. **Structural and functional brain development and its relation to cognitive development**. *Biological Psychology*, **54**(1-3):241 – 257, 2000. 81

[209] Gayane Meschyan and Arturo E. Hernandez. **Impact of language proficiency and orthographic transparency on bilingual word reading: An fMRI investigation**. *NeuroImage*, **29**(4):1135 – 1140, 2006. 82

[210] Mohamed L. Seghier, François Lazeyras, Alan J. Pegna, Jean-Marie Annoni, Ivan Zimine, Eugne Mayer, Christoph M. Michel, and Asaid Khateb. **Variability of fMRI activation during a phonological and semantic language task in healthy subjects**. *Human Brain Mapping*, **23**(3):140–155, 2004. 82

[211] S. Y. Bookheimer, T. A. Zeffiro, T. A. Blaxton, W. D. Gaillard, B. Malow, and W. H. Theodore. **Regional cerebral blood flow during auditory responsive naming: evidence for cross-modality neural activation**. *NeuroReport*, **9**(10):2409–2413, July 1998. 82

[212] Maurizio Corbetta and Gordon L. Shulman. **Control of Goal-directed and Stimulus-driven Attention in The Brain**. *Nature Reviews, Neuroscience*, **3**:201–215, 2002. 82

[213] Kevin S. LaBar, Darren R. Gitelman, Todd B. Parrish, and M.-Marsel Mesulam. **Neuroanatomic Overlap of Working Memory and Spatial Attention Networks: A Functional MRI Comparison within Subjects**. *Neuroimage*, **10**:695C704, 1999. 82

[214] Ridderinkhof KR, van den Wildenberg WP, Segalowitz SJ, and Carter CS. **Neurocognitive mechanisms of cognitive control: the role of prefrontal cortex in action selection, response inhibition, performance monitoring, and reward-based learning**. *Brain Cogn*, **56**:129 C140, 2004. 82

[215] Menon V, Adleman NE, White CD, Glover GH, and Reiss AL. **Error-related brain activation during a Go/NoGo response inhibition task**. *Hum Brain Mapp*, **12**:131C143, 2001. 82

[216] Kerns JG, Cohen JD, MacDonald III AW, Cho RY, Stenger VA, and Carter CS. **Anterior cingulate conflict monitoring and adjustments in control**. *Science*, **303**:1023C1026, 2004. 82

[217] Ridderinkhof KR, Ullsperger M, Crone EA, and Nieuwenhuis S. **The role of the medial frontal cortex in cognitive control**. *Science*, **306**:443C447, 2004. 82

[218] Peyron R, Laurent B, and Garcia-Larrea L. **Functional imaging of brain responses to pain. A review and meta-analysis**. *Neurophysiol Clin*, **30**:263C288, 2000. 82

[219] Craig AD. **How do you feel? Interoception: the sense of the physiological condition of the body**. *Nat Rev Neurosci*, **3**:655C 666, 2002. 82

[220] Eisenberger NI, Lieberman MD, and Williams KD. **Does rejection hurt? An FMRI study of social exclusion**. *Science*, **302**:290 C292, 2003. 82

[221] Christophe Habas, Nirav Kamdar, Daniel Nguyen, Katherine Prater, Christian F. Beckmann, Vinod Menon, and Michael D. Greicius. **Distinct Cerebellar Contributions to Intrinsic Connectivity Networks**. *The Journal of Neuroscience*, **29**(26):8586–8594, July 2009. 82

[222] Kaustubh Supekar, Lucina Q. Uddin, Katherine Prater, Hitha Amin, Michael D. Greicius, and Vinod Menon. **Development of functional and structural connectivity within the default mode network in young children**. *NeuroImage*, **52**(1):290 – 301, 2010. 82

[223] Jay N. Giedd, Jonathan Blumenthal, Neal O. Jeffries, F. X. Castellanos, Hong Liu, Alex Zijdenbos, Tomas Paus, Alan C. Evans, and Judith L. Rapoport. **Brain development during childhood and adolescence: A longitudinal MRI study**. *Nat Neurosci*, **2**(10):861C863, 1999. 82

[224] Johnson MH. **Functional brain development in infants: Elements of an interactive specialization framework**. *Child Dev*, **71**:75C81, 2000. 82

[225] Rhoshel K. Lenroot and Jay N. Giedd. **Brain development in children and adolescents: Insights from anatomical magnetic resonance imaging**. *Neuroscience Biobehavioral Reviews*, **30**(6):718–729, 2006. 85

[226] Jay N. Giedd and Judith L. Rapoport. **Structural MRI of Pediatric Brain Development: What Have We Learned and Where Are We Going?** *Neuron*, **67**(5):728–734, 2010. 85

[227] Alecia Vogel, Jonathan Power, Steven Petersen, and Bradley Schlaggar. **Development of the Brains Functional Network Architecture**. *Neuropsychology Review*, **20**(4):362–375, 2010. 85, 86

[228] Kerstin Konrad, Susanne Neufang, Christiane M. Thiel, Karsten Specht, Charlotte Hanisch, Jin Fan, Beate Herpertz-Dahlmann, and Gereon R. Fink. **Development of attentional networks: An fMRI study with children and adults**. *Neuroimage*, **28**(2):429–439, 2005. 85

[229] Sarah Durston and B. J. Casey. **What have we learned about cognitive development from neuroimaging?** *Neuropsychologia*, **44**(11):2149–2157, 2006. 85

[230] Sarah Durston, Matthew C. Davidson, Nim Tottenham, Adriana Galvan, Julie Spicer, John A. Fossella, and B.J. Casey. **A shift from diffuse to focal cortical activity with development**. *Developmental Science*, **9**(1):1–20, 2006. 85, 92

[231] Katerina Velanova, Mark E. Wheeler, and Beatriz Luna. **Maturational Changes in Anterior Cingulate and Frontoparietal Recruitment Support the Development of Error Processing and Inhibitory Control**. *Cerebral Cortex*, **18**(11):2505–2522, 2008. 85

[232] Elizabeth R. Sowell, Paul M. Thompson, Christiana M. Leonard, Suzanne E. Welcome, Eric Kan, and Arthur W. Toga. **Longitudinal Mapping of Cortical Thickness and Brain Growth in Normal Children**. *The Journal of Neuroscience*, **24**(38):8223–8231, 2004. 85, 100

[233] L. Tugan Muftuler, Elysia Poggi Davis, Claudia Buss, Kevin Head, Anton N. Hasso, and Curt A. Sandman. **Cortical and subcortical changes in typically developing preadolescent children**. *Brain Research*, **1399**:15–24, 2011. 85, 100

[234] Jin Fan, Bruce D. McCandliss, John Fossella, Jonathan I. Flombaum, and Michael I. Posner. **The activation of attentional networks**. *Neuroimage*, **26**(2):471–479, 2005. 85

[235] N. U. Dosenbach, K. M. Visscher, E. D. Palmer, F. M. Miezin, K. K. Wenger, and H.C. Kang. **A core system for the implementation of task sets**. *Neuron*, **50**:799–812., 2006. 85

[236] Amir Raz and Jason Buhle. **Typologies of attentional networks**. *Nat Rev Neurosci*, **7**(5):367–379, 2006. 85

[237] A. R. Aron. **The neural basis of inhibition in cognitive control**. *Neuroscientist*, **13**:214–228., 2007. 85

[238] Noa Ofen, Yun-Ching Kao, Peter Sokol-Hessner, Heesoo Kim, Susan Whitfield-Gabrieli, and John D E Gabrieli. **Development of the declarative memory system in the human brain**. *NATURE NEUROSCIENCE*, **10**(9):1198–1205, 2007. 85

[239] Beatriz Luna, Aarthi Padmanabhan, and Kirsten OHearn. **What has fMRI told us about the Development of Cognitive Control through Adolescence?** *Brain and Cognition*, **72**(1):101–113, 2010. 85

[240] Golijeh Golarai, Dara G Ghahremani, S Whitfield-Gabrieli, Allan Reiss, Jennifer L Eberhardt, John D E Gabrieli, and Kalanit Grill-Spector. **Differential development of high-level visual cortex correlates with category-specific recognition memory**. *NATURE NEUROSCIENCE*, **10**(4):512–522, 2007. 85

[241] Katya Rubia, Anna B. Smith, Eric Taylor, and Michael Brammer. **Linear age-correlated functional development of right inferior fronto-striato-cerebellar networks during response inhibition and anterior cingulate during error-related processes**. *Human Brain Mapping*, **28**(11):1163–1177, 2007. 85, 100

[242] Axel Mecklinger, Nicole Brunnemann, and Kerstin Kipp. **Two Processes for Recognition Memory in Children of Early School Age: An Event-related Potential Study**. *Journal of Cognitive Neuroscience*, **23**(2):435–446, 2010. 85

[243] Miriam Rosenberg-Lee, Maria Barth, and Vinod Menon. **What difference does a year of schooling make?: Maturation of brain response and connectivity between 2nd and 3rd grades during arithmetic problem solving**. *Neuroimage*, **57**(3):796–808, 2011. 85

[244] Beatriz Luna, Krista E. Garver, Trinity A. Urban, Nicole A. Lazar, and John A. Sweeney. **Maturation of Cognitive Processes from Late Childhood to Adulthood**. *Child Development*, **75**(5):1357–1372, 2004. 85

[245] William W. Seeley, Vinod Menon, Alan F. Schatzberg, Jennifer Keller, Gary H. Glover, Heather Kenna, Allan L. Reiss, and Michael D. Greicius. **Dissociable Intrinsic Connectivity Networks for Salience Processing and Executive Control**. *J. Neurosci.*, **27**(9):2349–2356, 2007. 86, 92, 100

[246] D. Fair and B. L. Schlaggar. **Brain Development**. In M. Haith Marshall and B. Benson Janette, editors, *Encyclopedia of Infant and Early Childhood Development*, pages 211–225. Academic Press, San Diego, 2008. 86

[247] JP Lerch and AC Evans. **Cortical thickness analysis examined through power analysis and a population simulation**. *Neuroimage*, **24**:163173, 2005. 88

[248] Carin M. Tillman, Lisa B. Thorell, Karin C. Brocki, and Gunilla Bohlin. **Motor Response Inhibition and Execution in the Stop-Signal Task: Development and Relation to ADHD Behaviors**. *Child Neuropsychology*, **14**(1):42 – 59, 2008. 88

[249] Ad-Dabbagh Y, Singh V, Robbins S, Lerch J, Lyttelton O, and Fombonne E. **Nativespace cortical thickness measurement and the absence of correlation to cerebral volume**, 2005. 89

[250] Elizabeth R. Sowell, Bradley S. Peterson, Eric Kan, Roger P. Woods, June Yoshii, Ravi Bansal, Dongrong Xu, Hongtu Zhu, Paul M. Thompson, and Arthur W. Toga. **Sex Differences in Cortical Thickness Mapped in 176 Healthy Individuals between 7 and 87 Years of Age**. *Cerebral Cortex*, **17**(7):1550–1560, 2007. 89

[251] M.D. Humphries and K. Gurney. **Network 'small-world-ness': a quantitative method for determining canonical network equivalence**. *PLoS ONE*, **3**(4):e0002051, 2008. 90

[252] Yong He, Zhang J. Chen, and Alan C. Evans. **Small-World Anatomical Networks in the Human Brain Revealed by Cortical Thickness from MRI**. *Cerebral Cortex*, **17**(10):2407–2419, 2007. 90

[253] Vincent JL, Kahn I, Snyder AZ, Raichle ME, and Buckner R.L. **Evidence for a Frontoparietal Control System Revealed by Intrinsic Functional Connectivity**. *J Neurophysiol*, **100**:3328–3342, 2008. 92, 100

[254] K. Suzanne Scherf, John A. Sweeney, and Beatriz Luna. **Brain Basis of Developmental Change in Visuospatial Working Memory**. *Journal of Cognitive Neuroscience*, **18**(7):1045–1058, 2006. 92, 100, 101

[255] B. J. Casey, Adriana Galvan, and Todd A. Hare. **Changes in cerebral functional organization during cognitive development**. *Current Opinion in Neurobiology*, **15**(2):239–244, 2005. 100, 102

[256] Elizabeth R. Sowell, Dean Delis, Joan Stiles, and Terry L. Jernigan. **Improved memory functioning and frontal lobe maturation between childhood and adolescence: A structural MRI study**. *Journal of the International Neuropsychological Society*, **7**(03):312–322, 2001. 100

[257] B. J. Casey, Nim Tottenham, Conor Liston, and Sarah Durston. **Imaging the developing brain: what have we learned about cognitive development?** *TRENDS in Cognitive Sciences*, **9**(3):104–110, 2005. 100

[258] Nitin Gogtay, Jay N. Giedd, Leslie Lusk, Kiralee M. Hayashi, Deanna Greenstein, A. Catherine Vaituzis, Tom F. Nugent, David H. Herman, Liv S. Clasen, Arthur W. Toga, Judith L. Rapoport, and Paul M. Thompson. **Dynamic mapping of human cortical development during childhood through early adulthood**. *Proceedings of the National Academy of Sciences of the United States of America*, **101**(21):8174–8179, 2004. 100

[259] Michelle Hampson, Naomi R. Driesen, Pawel Skudlarski, John C. Gore, and R. Todd Constable. **Brain Connectivity Related to Working Memory Performance**. *The Journal of Neuroscience*, **26**(51):13338–13343, 2006. 100, 102

[260] Bunge SA, Dudukovic NM, Thomason ME, Vaidya CJ, and Gabrieli JDE. **Immature frontal lobe contributions to cognitive control in children: evidence from fMRI**. *Neuron*, **33**:301–311, 2002. 101

[261] Booth JR, Burman DD, Meyer JR, Lei Z, Trommer BL, Davenport ND, Li W, Parrish TB, Gitelman DR, and Mesulam MM. **Neural development of selective attention and response inhibition**. *Neuroimage*, **20**:737–751, 2003. 101

[262] Maurizio Corbetta and Gordon L. Shulman. **Control of Goal-directed and Stimulus-driven Attention in The Brain**. *Nature Reviews, Neuroscience*, **3**:201–215, 2002. 101

[263] AW Toga and PM Thompson. **Mapping brain asymmetry**. *Nat Rev Neurosci*, **4**:37–48, 2003. 101

[264] Frith CD Amodio DM. **Meeting of minds: the medial frontal cortex and social cognition**. *NATURE REVIEWS, NEUROSCIENCE*, **7**:268–277, 2006. 102

[265] J.-F. Mangin, D. Rivière, A. Cachia, E. Duchesnay, Y. Cointepas, D. Papadopoulos-Orfanos, P. Scifo, T. Ochiai, F. Brunelle, and J. Régis. **A framework to study the cortical folding patterns**. *NeuroImage*, **23**(Supplement 1):S129 – S138, 2004. Mathematics in Brain Imaging. 106

[266] Gang Li, Lei Guo, Jingxin Nie, and Tianming Liu. **An automated pipeline for cortical sulcal fundi extraction**. *Medical Image Analysis*, **14**(3):343 – 359, 2010. 106

[267] Matthieu Perrot, Denis Rivière, and JF Mangin. **Cortical sulci recognition and spatial normalization**. *Medical Image Analysis*, **In Press, Corrected Proof**:–, 2011. 106

[268] Alan Anticevic, Grega Repovs, Donna L. Dierker, John W. Harwell, Timothy S. Coalson, Deanna M. Barch, and David C. Van Essen. **Automated landmark identification for human cortical surface-based registration**. *NeuroImage*, (0):–, 2011. 106

Appendix A

A.1 Anatomical Definition of Sulcal Curves

Fourteen sulcal curves were semi-automatically tracked on each cortical surface via dynamic programming (125) once the starting and ending points of each curve were selected. The criteria for selecting these sulci were determined based on reproducibility and patterns of the sulci (115, 124). We classified these fourteen sulci into two categories based on the definition given in (124): uninterrupted and interrupted. The uninterrupted sulci are long and continuous; the interrupted sulci often have branches and are more variable across subjects than the uninterrupted sulci. We closely followed the sulcal definitions given in (115) and briefly described how to determine the starting point and ending point of each sulcal curve.

Uninterrupted Curves:

1. Central Sulcus
   - starting point: superior end close to the midline;
   - ending point: inferior end superior to the Sylvian fissure.
2. Sylvian Fissure
   - starting point: posterior end inside the supramarginal gyrus;
   - ending point: anterior point where the temporal lobe separates from the frontal lobe.
3. Collateral Sulcus
   - starting point: posterior end on the midline;
   - ending point: anterior end at the level with the pons.

4. Superior Callosal Sulcus
    - starting point: posterior end at the splenium of the corpus callosum;
    - ending point: anterior end at the rostrum of the corpus callosum.
5. Posterior Calcarine Sulcus
    - starting point: posterior end near the dorsolateral surface in the occipital pole;
    - ending point: anterior end near the parieto-occipital fissure.
6. Parieto-Occipital Fissure
    - starting point: superior end close to the boundary of the dorsolateral surface;
    - ending point: inferior end superior to the calcarine sulcus.

Interrupted Curves:

1. Superior Frontal Sulcus
    - starting point: posterior end near to the precentral sulcus;
    - ending point: anterior end near to the orbiral margin of the hemisphere.
2. Inferior Frontal Sulcus
    - starting point: posterior end near to the precentral sulcus;
    - ending point: anterior end near to the fronto-orbital sulcus or frontomarginal sulcus if the branches happen. It stops at the bifurcation between the ascending and descending parts.
3. Postcentral Sulcus
    - starting point: superior end near to the medial surface and behind the central sulcus. If the superior extent of the sulcus is not continuous up to the midline, always choose the posterior extent;
    - ending point: inferior end superior to the Sylvian fissure. If the branches happen, the end point is defined at the end of the posterior branch.
4. Intraparietal Sulcus

- starting point: posterior end at the temporal-occipital notch where the bifurcation between the ascending and descending segments is close to the intersection with the transverse occipital sulcus. When the branches happen, the end point is defined at the end of the inferior branch;
- ending point: There are cases that the intraparietal sulcus connects to the superior or inferior, or both segments of the postcentral sulcus. If the connection is only at the superior or inferior segment, the end point is defined at the intersection. If the intraparietal sulcus intersects with both superior and inferior segments of the postcentral sulcus, then the end point is defined at the intersection of the inferior segment of the postcentral sulcus.

5. Anterior Segment of the Superior Temporal Sulcus
    - starting point: posterior end close to the intersection with the transverse occipital sulcus. When the branches happen, the end point is defined at the end of the inferior branch;
    - ending point: anterior end before the bifurcation of the ascending and descending segments.
6. Precentral Sulcus
    - starting point: superior end at the midline of the anterior route;
    - ending point: inferior end near the Sylvian fissure.
7. Inferior Temporal Sulcus
    - starting point: posterior end at the temporal-occipital notch or the intersection of the anterior occipital sulcus;
    - ending point: anterior end before any branch.
8. Olfactory Sulcus
    - starting point: most posterior extent of the olfactory sulcus away from the midline;
    - ending point: anterior end near the frontal lobe.